Understanding Organic Reaction Mechanisms Through Applications of Density-Functional Theory

A THESIS
SUBMITTED TO THE FACULTY OF THE GRADUATE SCHOOL
OF THE UNIVERSITY OF MINNESOTA
BY

Daniel Joshua Marell

IN PARTIAL FULFILLMENT OF THE REQUIREMENTS
FOR THE DEGREE OF
Doctor of Philosophy

Christopher J. Cramer

August, 2016

Acknowledgments

There are so many people that have been involved in both my professional and personal life leading up to the completion of this thesis. I would like to highlight a few specific people who have participated in major ways.

My adviser, Chris Cramer has been an incredible support in a many avenues. From discussions about thesis research, navigating a job search process and conversations about teaching philosophy to name just a few. His dedication to mentorship and understanding my goals as a student, colleague and as a future professional have been immensely appreciated.

Within the Cramer group, I would like to thank Michelle Johnson for the incredible friendship that has grown from our time working together. She provided great support and was a terrifically motivated student I had the pleasure of mentoring. I would like to thank Xiangyun Lei for his immensely dedicated work on the HDDA project. Additionally, I would like to acknowledge other groups members, specifically Aaron League, Will Isley, Stuart Winikoff, Büşra Dereli, and Andreas Mavrantonakis for their insightful conversations and contributions to my own growth as a chemist.

The experimental collaborators I've worked with on these projects have been instrumental in bringing these projects to completion. They've also served a pivotal role in helping expand my understanding of chemistries beyond theoretical chemistry. I'd like to thank Maria Miranda, Eloide Marlier, Johanna Macaranas, Brent Rivard and Melanie Rogers for all their efforts on our projects together.

I'd like to thank my boyfriend Nick who has encouraged so much personal growth of myself. His kindness, understanding and constant encouragement as I have worked to finish my program and thesis have been critical to my success. Always there with a smile no matter how late I've had to work, I cannot thank him enough for being with me each step of the way.

My family has also been an invaluable supportive network during my time working on my PhD. My parents have always encouraged my pursuit of passions and interests. I'd like to thank my Dad, Michael, for having a fascination in the sciences and technology which I'm sure sparked my own passions. Also, a thank you to my mom, Ellyn, for her patience and understanding as I wrecked more than one item of her cookware while carrying out science experiments in the kitchen without her permission. My brother Noah has also been an unwavering support of my studies and interests. By example of his own hard work ethic, he has pushed me to dedicate myself even more so to my goals. I also appreciate the many helpful conversations we've shared about productivity and work efficiency. My extended family, whom I share a very close connection with has always shown interest in my studies and I'm thankful to have their support and love.

Abstract

The application of computational chemistry has a wide scope of utility. From large systems such as proteins or metal-organic frameworks down to the understanding of individual bonding patterns between atoms, there are endless opportunities to explore. Further utility is gained when the insights and resources of computational chemists can be applied to systems under investigation by experimental chemists The combined information of computational details with experimental findings can lead to new understanding of the systems being investigated.

The ring-opening transesterification polymerization of caprolactone with an aluminum-salen catalyst is a useful reaction for the conversion of caprolactone to polyester. Mechanistic understanding of this reaction was gained through the interrogation of this process with density functional theory. Further, the origins for rate-enhancement through modification of electron-withdrawing groups was explained through the analysis of partial atomic charges. A rate enhancement observed by altering the backbone of the catalyst was also explained through the development of a distortion framework analysis.

Rieske oxygenase are a class of protein that executes a variety of chemical reactions such as oxygenations, O- and N-demethylations, oxidations, and C–C bond formations *en route* to the formation of medically relevant natural products. The continued elucidation of the mechanism, including the characterization of reactive species was persued. Computational work to understand the impact partial atomic charge on the aromatic system (by inclusion of fluorine substituents) had on the rate constant demonstrated a clear correlation between the partial atomic charge on the C(2) position and the rate constant for a variety of substrates.

A new reaction, the hexadehydro-Diels–Alder (HDDA) reaction takes a diyne and a diynophile to create a reactive benzyne intermediate. A series of six intramolecular HDDA substrates were found to undergo this transformation at relatively similar rates. Analysis of transition state geometries, investigation of both closed-shell and diradical mechanistic pathways, as well as insight from high-level calculations provide information about the nature of this intramolecular reaction. Extension of the mechanism led to predictive capability in good agreement with a new set of substrates as well.

Table of Contents

List of Tables

List of Figures

Acronyms

ACV	δ-(L-α-aminoadipoyl)-L-cysteinyl-D-valine
AO	atomic orbital
BL	γ-butyrolactone
CarDO	carbazole 1,9a-dioxygenase
CASSCF	complete-active space self-consistent field
CL	ε-caprolactone
DFT	density functional theory
EWGs	electron-withdrawing groups
GGA	generalized-gradient approximation
HDDA	hexadehydro-Diels–Alder
HF	Hartree-Fock
IDO	indolamine 2,3-dioxygenase
KIE	kinetic isotope effect
LA	lactide
LDA	local density approximation
LSDA	local spin-density approximation
MMO	methyl monooxygenase
NBDO	nitrobenzene 1,2-dioxygenase
NDO	naphthalene 1,2-dioxygenase
NMR	nuclear magnetic resonance
PES	potential energy surface
PLA	poly(lactide)
RDD	Rieske dearomatizing dioxygenase
ROP	ring-opening polymerization
ROTEP	ring opening transesterification polymerization
RPKA	reaction progress kinetic analysis
RRT	reciprocal relaxation time
SCF	self-consistent field
TDO	tryptophan 2,3-dioxygenase
TS	transition-state
UDFT	Unrestricted Density Functional Theory

Preface

Citations from previously published work in this thesis are as follows:

Understanding ROTEP of Caprolactone with Al-Salen Catalysts

2.1 Understanding the Mechanism of Polymerization of ε-Caprolactone Catalyzed by Aluminum Salen Complexes
Adapted with permission from:

Miranda, Maria O.; DePorre, Yvonne; Vazquez-Lima, Hugo; Johnson, Michelle A.; Marell, Daniel J.; Cramer, Christopher J.; Tolamn, William B.

Inorg. Chem., **2013**, *52* (23), pp 13692–13701

Link: http://dx.doi.org/10.1021/ic402255m

2.2 Mechanistic Studies of ε-Caprolactone Polymerization by (salen)AlOR Complexes and a Predictive Model for Cyclic Ester Polymerizations
Adapted with permission from:

Marlier, Elodie E.; Macaranas, Joahanna A.; Marell, Daniel J.; Dunbar, Christine R.; Johnson, Michelle A.; DePorre, Yvonne; Miranda, Maria O.; Neisen, Benjamin D.; Cramer, Christopher J.; Hillmyer, Marc A.; Tolman, William B.

ACS Catal., **2016**, *6* (2), pp 1215–1224

Link: http://dx.doi.org/10.1021/acscatal.5b02607

Probing Electronic Properties of Small-Molecule Systems

3.1 Rate-Determining Attack on Substrate Precedes Rieske Cluster Oxidation during Cis-Dihydroxylation by Benzoate Dioxygenase
Adapted with permission from:

Rivard, Brent S.; Rogers, Melanie S.; Marell, Daniel J.; Neibergall, Matthew B.; Chakrabarty, Sarmistha; Cramer, Cristopher J.; Lipscomb, John D.

Biochemistry, **2015**, *54* 30, pp 4652–4664

Link: http://dx.doi.org/10.1021/acs.biochem.5b00573

Interrogating Reaction Mechanisms for Complex Organic Reactions

4.1 Mechanism of the Intramolecular Hexadehydro-Diels–Alder Reaction
Adapted with permission from:

Marell, Daniel J.; Furan, Lawrence R.; Woods, Brain P.; Lei, Xiangyun; Bendelsmith, Andrew J.; Cramer, Cristopher J.; Hoye, Thomas R.; Kuwata, Keith T.

J. Org. Chem., **2015**, *80* (23), pp 11744–11754

Link: http://dx.doi.org/10.1021/acs.joc.5b01356

1. Introduction

1.1 Background of Computational Chemistry

Computational chemistry is a science that is based on the critical work of Schrödinger[1] and Heisenberg.[2] With the invention of the modern computer, the computation of properties relating to small molecules (and as computing capabilities have increased, larger and larger molecules) became possible for a variety of chemical systems. The various properties of a molecule can be exactly described by analytically solving the the time-independent Schrödinger equation, Eq. 1.1. The complexity of the Schrödinger equation, however limits an exact analytic solution to only when there is one electron present.

$$E\Psi = \hat{H}\Psi \tag{1.1}$$

While solving the Schrödinger equation exactly is not possible, Hartree developed a method for taking a serious of successive estimates to arrive at an answer as close as possible to the exact solution. This series of iterative estimates is known as self-consistent field (SCF) theory.[3] In order to circumvent the issue of solving the Schrödinger equation for a many-electron system, Hartree's SCF approach places each electron into it's own one-electron potential or wave functions. The product of these individual wave functions (Ψ_{HP}), is then used to describe the eigenfunction of the Schrödinger equation (Ψ, Equation 1.2a & 1.2b).

$$\Psi_{HP} = \prod_{i=1}^{n} \psi_i(r_i) \tag{1.2a}$$

$$\Psi(x_1, x_2, \ldots, x_n) = \chi_1(x_1), \chi_2(x_2), \ldots, \chi_n(x_n) \tag{1.2b}$$

As this is an estimated approach to calculating the exact Schrödinger solution, each one-electron wave function, ψ_i, is populated with an *initial guess* for every populated atomic

orbital (AO). Able to solve the one-electron Shrödinger equation, Eq. 1.3, leads to the generation of a new set of wave functions, which are then solved again giving yet another set of wave functions. This iterative process is repeated until some criteria is reached. One such criteria may be the change in energy from one wave function to the next is below a certain threshold.

$$h_i\psi_i = \varepsilon\psi_i \tag{1.3}$$

The initial work by Hartree was crucial to bringing the unsolvable many-electron Schrödinger equation into the reach of computation. However, Hartree's representation of the wave function was not antisymmetric (Eq. 1.2b), which is a violation of the Pauli-exclusion principle. Fock expanded on Hartree's work to account for this requirement by utilizing Slater determinants,[4] leading to the development of Hartree-Fock (HF) theory.[5]

As computing technology became available in the 1950s, application of HF theory became possible. However, because HF requires the description of every electron in the system and their interaction, the computational cost for most systems of interest remained too large. In the early 1960s, work by Hohenberg and Kohn[6] as well as Kohn and Sham,[7] sought to describe the electrons in a manner that did not require evaluation of each pair-wise interaction in the many-body wavefunction. Rather, they represented the electrons as a assembly of non-interacting electrons in an effective potential which could be described by the ground-state electron density, a theory called density functional theory (DFT). The popularity of utilizing DFT theory caught on in the early 1990s with the number of papers using the phrase DFT in their title or abstract rose quickly (Figure 1.1). The ability to expand the scope of chemical systems that could be interrogated without excessive computing power makes the use of DFT a popular choice.

Fig. 1.1 Number of Publications Listing DFT as a Topic

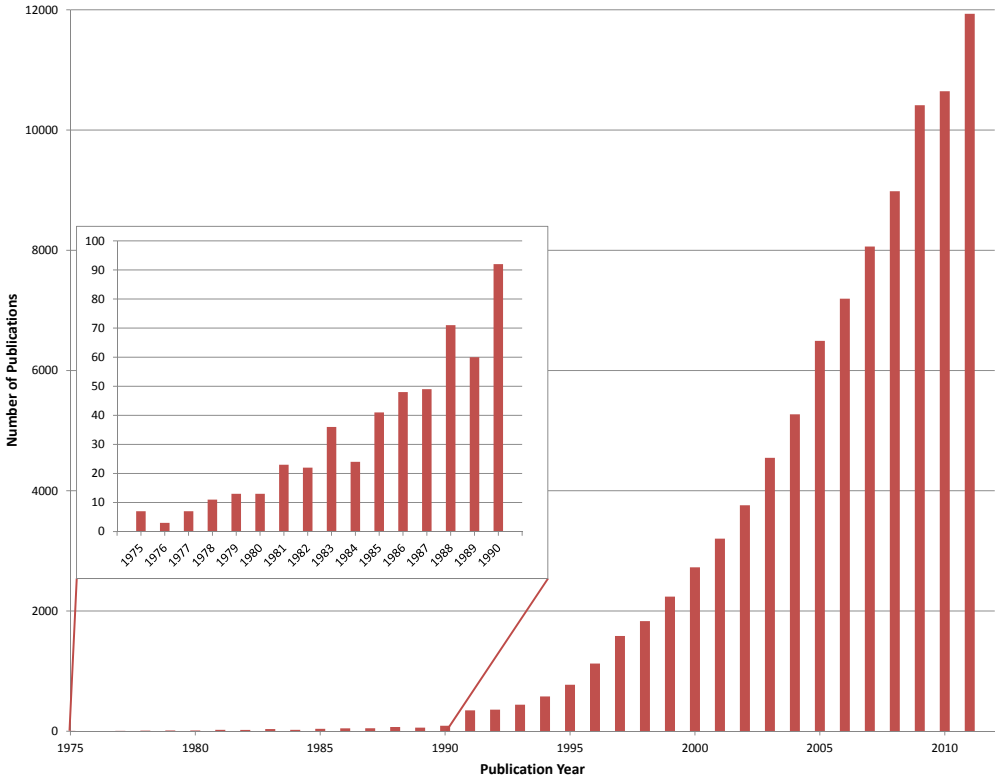

Graph compiled from data provided from a search of "dft" as a topic keyword on the Web of Knowledge database

1.2 Evaluation and Use of Density Functional Theory Methods

While DFT is a popular choice for computation of molecular systems, it has a specific limitation in that the functional form has an inexact description of a crucial term. The exchange-correlation (E_{xc}) energy describes the kinetic energy difference between an interacting and non-interacting system as well as Coulomb interactions of the electrons (since

DFT assumes them to be non-interacting). Each functional in DFT is left to decide what form and solution to use to approximate this energy. There are however, a few high-level groups that describe the most common ways in which this energy is evaluated.

Local density approximation (LDA) is the most simple form for DFT, in which the functional depends only on the electron density at the location in the system being calculated. This means there is an assumption that the density remains consistent throughout the system. A further expansion of the LDA is the local spin-density approximation (LSDA) which works to include some correction for electron spin. To continue a more accurate description of the density, Generalized-gradient approximation (GGA) functionals were developed. These functionals no longer assume the density to remain consistent throughout the system, and instead use the gradient of the density to approximate its change away from the coordinate being calculated. Finally, a further refinement of the GGA functionals is in the form of the meta-GGA functionals. These take into account the density at the coordinate (LDA), the gradient of the density (GGA) as well as the 2^{nd} derivative of the denisty. Within all these functionals, the approximation of the exact E_{xc} comes by way of some derivation from the electron density of the system. One alternative solution to improve the accuracy in computation of this E_{xc} term is by including a small portion of HF energy which has an exact solution for this E_{xc} term. Functionals that incorporate a percentage of energy from a HF calculation are referred to as hybrid functionals.

With so many possible DFT functional groups and the myriad of functionals within each group, the task of determining which is the best representation of a chemical system (where best could be any metric of importance; e.g., activation energies, nuclear magnetic resonance (NMR) chemical shifts, redox potentials, etc.) is a crucial piece in any project. In the most ideal case, expensive high-level calculations are used as a benchmark for a representative set of systems, by which a selection of DFT results are compared against. The best performing functionals are then used for the remainder of the project on the complete set of systems

being explored. In other cases, the size of the molecule may be so large as to make very high-level calculations impractical. There are two main options that might be considered in this case. If there is existing experimental data available, comparison of the results from the suite of functionals available may be referenced to the experimental value (considered as a true value). If experimental data is not available, extra thorough consideration for many different DFT functionals must be used to see what common trends or patterns may emerge depending on the form of the functionals chosen. From those, a small selection or one choice may be used to average or as a best-approximation for the true system. Regardless of the data available, guidance from references where calculations on related structures can also aid in the determination of the most proper choice of functional. In this work, nearly all options discussed above are used in one form or another to provide a high level of confidence in the results obtained.

1.3 General Organization

This thesis highlights the various ways DFT can be applied to a variety of interesting systems. Each chapter of this work is devoted to a separate molecular system with specific aims for the projects guided by questions from experimental collaborators.

Chapter 2 is devoted to the work on understanding the mechanism and details of ring opening transesterification polymerization (ROTEP) aluminum-salen catalysts. These catalysts undergo the ROTEP reaction with caprolactone to afford a polyester chain. In this work, modification of the catalyst backbone and electron-withdrawing groups (EWGs) on the catalyst impact the observed rate of the reaction. In addition, experimental measurements were able to determine activation energies, and a clear trend with respect to modification of the EWGs was observed. Computational work focused on elucidating the mechanism of

this ROTEP as a basis for interrogating the impacts modification of the catalyst structure and electronic environment had on the activation energies. With further understanding into this catalytic system, the scope of catalyst structures was expanded to investigate the predicative capability of a distortion framework model for rapidly determining possible catalyst structures that would be reaction towards the ROTEP reaction.

Chapter 3 is focused on a project involving the investigation of a protein system involved in oxygenation, demethylations, oxidations and C–C bond formations of various substrates in the synthesis of medically relevant natural products. This protein, named Rieske oxygenase, has some uncertainty as to the mechanism of its oxygenation pathway on its aromatic substrates. One avenue of exploration included the use of a set of electronically modified aromatic system (by fluorinating at various positions on the aromatic ring) and observing changes in the rate of single-turnover. The hypothesis was that if fluorination impacted the rate, and thus possibly the electrophilic nature of the aromatic system, this might be correlated well with a computed partial atomic charge. The small size of the aromatic rings, and the relatively simple calculation of partial charges yielded valuable data for the experimentalists to observe a clear trend in rate constants and partial charge on the ring, thus furthering their mechanistic understanding of this system.

Chapter 4 explores the complexities involved when investigating a system that has the potential to include radical character. A new reactivity in triynes, termed the hexadehydro-Diels–Alder (HDDA) reaction, leads to the formation of *o*-benzynes. This system was explored to understand the remarkably similar rates of reactivity amongst substrates that the experimental collaborators had initially thought should show markedly different results. Examining this molecular group highlighted the limitations of DFT to tackle reaction pathways with similar energetics and orbital arrangements that can sometimes have a level of multi-reference character. It also highlighted the importance of benchmarking and analysis of various DFT functionals to ensure the use of an appropriate functional is chosen.

References

[1] Schrödinger, E. *Ann. Phys.* **1926**, *79*, 361.

[2] Heisenberg, W. *Z. Phys.* **1925**, *33*, 879.

[3] Hartree, D. R. *Proc. Cambridge Phil. Soc.* **1928**, *24*, 89–110.

[4] Slater, J. C. *Phys. Rev.* **1929**, *34*, 1293–1322.

[5] Fock, V. *Z. Phys.* **1930**, *61*, 126–148.

[6] Hohenberg, P.; Kohn, W. *Phys. Rev.* **1964**, *136*, B864–B871.

[7] Kohn, W.; Sham, L. J. *Phys. Rev.* **1965**, *140*, A1133–A1138.

2. Understanding ROTEP of Caprolactone with Al-Salen Catalysts

2.1 Understanding the Mechanism of Polymerization of ε-Caprolactone Catalyzed by Aluminum Salen Complexes

2.1.1 Introduction

Ring opening transesterification polymerization (ROTEP), a specific type of ring-opening polymerization, of cyclic esters is an important method for converting renewable resources to aliphatic polyesters, sustainable materials useful for myriad applications and as potential alternatives to petrochemical polymers.[1,2] Polymerization of monomers like lactide (LA) and ε-caprolactone (CL) have been particularly well studied using a variety of polymerization methods.[3–7] Metal-alkoxide catalysts are often employed as ring opening transesterification polymerization (ROTEP) catalysts in both academic and industrial settings, and are especially attractive because of their ability to generate high molecular weight polymers in controlled fashion, with low polydispersities, and with maintenance of end-group fidelity.[3–6]

The mechanistic paradigm for ROTEP by single-site metal alkoxide catalysts is the so-called "coordination–insertion" pathway (Figure 2.1).

Fig. 2.1 Coordination–Insertion Mechanism for the Polymerization of Cyclic Esters.

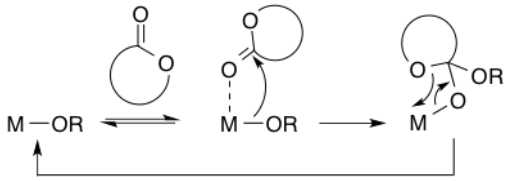

According to this mechanism, monomer coordinates through the carbonyl oxygen to a vacant site on the Lewis acidic metal, followed by alkoxide insertion into the activated carbonyl carbon and ring-opening to generate a new propagating alkoxide. While widely accepted, significant gaps in our understanding of this mechanism remain. For example, variable electronic and steric effects of supporting ligands on rates of ROTEP catalyzed by metal alkoxide complexes raise questions about the relative importance of monomer binding, alkoxide nucelophilicity, or both in controlling polymerization reactivity. Thus, for various salen aluminum catalysts, the groups of Gibson and Nomura both observed increased rates for the polymerization of LA when the ligands were substituted with electron-withdrawing groups (EWGs).[8,9] They postulated the enhancement is due to increased Lewis acidity of the aluminum, which boosts monomer binding and activation. Another study using a dinuclear salen aluminum complex found contradictory rate trends between monomers; in the case of LA polymerization, EWGs increased the rate, whereas in the case of CL polymerization, the opposite effect was observed.[10] Rate attenuation by EWGs has also been observed for titanium salen complexes,[11] magnesium complexes bearing benzenesulfonate phenol ligands,[12] and some aluminum alkoxide complexes supported by bis(phenolate)diamine ligands (**1** in Figure 2.2).[13]

Fig. 2.2 Representative Al-Salen Catalysts

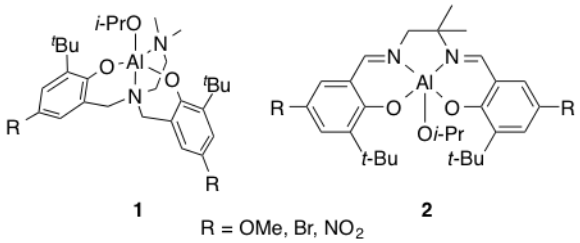

We recently examined the kinetics of CL polymerization catalyzed by the latter aluminum alkoxide complexes (**1**) in detail.[14] We found that by studying the reactions using high concentrations of monomer, saturation kinetics were observed enabling determination of a monomer binding equilibrium constant, K_{eq}, and a catalytic rate constant, k_2, that we attributed to the coordination and insertion steps, respectively. The data showed that the origin of the rate differences across the series of catalyts is entirely due to differences in k_2, and on the basis of both experiment and theory we argued that the nucelophilicity of the alkoxide is the determining factor (increasing nucelophilicity with increasing electron-donation). However, analysis of the catalytic activity of **1** was complicated by the potential for decoordination of the dimethylalkylamino arm of the polydentate ligand.

With the aim of further understanding the diverse electronic and steric effect of ligand substituents on the ROTEP efficiencies of metal alkoxide complexes, we turned our attention to aluminum complexes supported by salen-type ligands (**2**), where decoordination of the ligand rom the metal ion is unlikely. Such Schiff base complexes have been used extensively in catalysis,[15,16] and (with variable substituents and linkers between the imino nitrogen atoms) are notably effective for ROTEP of a variety of lactones.[8,9,17–30] Published kinetic/mechanistic studies of ROTEP catalyzed by Schiff base Al compounds have provided important information, such as ligand structure effects on ROTEP rates for a variety of lactones[29] (cf. the forementioned rate enhancement of LA polymerization

by electron withdrawing ligand substituents),[8,9] ^{1}H nuclear magnetic resonance (NMR) spectroscopic evidence for reversible LA coordination to the catalyst,[27] and the basis for observed poly(lactide) (PLA) tacticity in stereospecific polymerizations.[18–22,26,27]

Herein we report the results of detailed kinetic studies of CL polymerization by well-characterized, monomeric aluminum salen complexes with identical steric profiles but variable remote substituents with differing electron donating characteristics (**2**). Using our previously described methodology involving ^{1}H NMR spectroscopic analysis of ROTEP kinetics performed with high initial monomer concentrations,[14] we again observed saturation behavior that enabled determination of K_{eq} and k_2 values for the catalyst series of **2**, but with trends opposite to that seen for **1**. Density functional theory (DFT) calculations were performed to rationalize the kinetic data, and provide key mechanistic insights, including a new rationale for the experimental rate law that has significant, broader implications for evaluating metal-alkoxide catalyzed ROTEP kinetics.

2.1.2 Results and Discussion

Synthesis and Characterization of Ligands and Catalysts The ligands required to synthesis complexes **2** (R = OMe, Br, NO_2) were prepared using a traditional imine condensation between the three differently substituted salicylaldehydes and 2-methylpropane-1,2-diamine in yields ranging from 35 % (R = Br) to 98 % (R = OMe). Complexes **2** were synthesized in high yields (84–97 %) via thermolysis of equimolar amounts of ligand and aluminum tris(*iso*-propoxide) in toluene. Complexes **2** (R = Br, NO_2) were isolated as analytically pure yellow and light brown solids, respectively, directly from the reaction mixture, whereas **2** (R = OMe) required recrystallization from toluene and pentane to isolate pure, bright yellow, material. The compounds are air- and moisture-sensitive and soluble in chlorinated (dichloromethane) and aromatic hydrocarbon (toluene) solvents. As

in the ^{1}H NMR spectra, with the most significant differences being in the aryl region; the aryl residues shift downfield as the electron-withdrawing nature of the catalyst increases. In solution the complexes appear monomeric, as expected because of the presence of the *t*-butyl substituents[31] and as indicated by a single set of resonances in their ^{1}H NMR spectra and a single resonance in their ^{27}Al NMR spectra at 35, 34 and 33 ppm (R = OMe, Br, or NO_2, respectively). This ^{27}Al NMR chemical shift region is indicative of a five-coordinate aluminum center, and matches that reported previously for a pentacoordinate salen-type aluminum alkoxide (35 ppm).[22,24,32]

In addition, a crystal of **2** (R = OMe) suitable for X-ray diffraction was obtained from a toluene/hexane mixture at −40 °C. The structure (Figure 2.3) features a monomeric complex with a 5-coordinate aluminum ion in a geometry between square pyramidal and trigonal bipyramidal ($\tau = 0.52$).[33]

Fig. 2.3 Representation of the X-ray Crystal Structure of **2** (R = OMe).

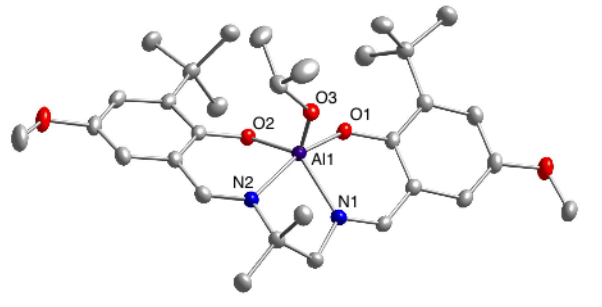

Nonhydrogen atoms are shown as 50 % thermal ellipsoids. Selected interatomic distances (Å) and angles (deg): Al1–O1,1.8107(13); Al1–O2, 1.7899(12); Al1–O3, 1.7292(13); Al1–N1, 2.0042(14); Al1–N2, 2.0445(15); O3–Al1–O2, 115.98(6); O3–Al1–O1, 100.22(6); O2–Al1–O1, 97.57(6); O3–Al1–N1, 113.60(6); O2–Al1–N1, 129.72(6); O1–Al1–N1, 87,59(6); O3–Al1–N2, 96.96(6); 2–Al1–N2, 88.00(6); O1–Al1–N2, 161.05(6); N–Al1–N2, 78.22(6).

Other structures of complexes with the 2-methylpropane-1,2-diamine backbone display similarly intermediate τ parameters ($0.48 < \tau < 0.56$).[31,34] Bond distances and angles are

consistent with other aluminum salen-type structures.

Polymerization Kinetics Polymerization of CL using catalysts **2** were performed in triplicate with fixed initial concentration of CL (2 M < $[CL]_0$ < 2.6 M) and catalyst (5.5 mM < $[\mathbf{2}]_0$ < 7 mM) in toluene-d_8 at temperatures ranging from 20 to 90 °C. As in a previous study,[14] features due to the growth of polymer and decay of monomer were monitored by ^{1}H NMR spectroscopy to polymerization completion (conversions >99 %) and their concentrations as a function of time were fit to the Michaelis-Menten expression (Eq. 2.1) using the global kinetics fitting program COPASI (version 4.8).[35] Good agreement between the fit and the data was obtained (representative plot in Figure 2.4; all data shown in Supporting Information, Figure S1).

Fig. 2.4 Illustrative Conversion vs. Time Profile for Decay of CL (■) and Growth of PCL (◆)

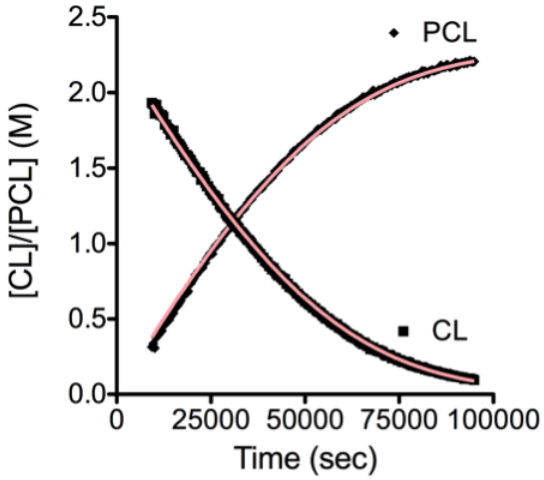

Growth and decay of resonances during ROTEP catalyzed by R = OMe at 333 K, determined from ^{1}H NMR spectra, along with fits (red lines) determined by COPASI.

$$-\frac{\mathrm{d[CL]}}{\mathrm{d}t} = \frac{\mathrm{d[PCL]}}{\mathrm{d}t} = \frac{k_2[\mathbf{2}][\mathrm{CL}]}{1/K_{\mathrm{eq}} + [\mathrm{CL}]} \tag{2.1}$$

These fits, and curved rate vs. [CL] plots derived from both the COPASI analysis (Supporting Information, Figure S2) and a reaction progress kinetic analysis[36] (using derivatives of polynomial fits; Supporting Information, Figure S7) support saturation behavior; significantly poorer fits were obtained using simpler first- or second-order rate equations (Supporting Information, Figures S3–S7). Average values from replicate runs for K_{eq} and k_2 are listed in Table 2.1, with all values provided in the Supporting Information, Table S1.

Table 2.1 Average Values of Kinetic Parameters Determined from COPASI Fits and NMR Peak Analysis

Entry	Temps (K)	R	K_{eq} COPASI (M^{-1})	K_{eq} NMR (M^{-1})	k_2 (s^{-1}) ($x10^2$)
1	333	OMe	0.9(1)	0.70(5)	1.00(3)
2	343	OMe	0.92(9)	0.54(7)	2.1(1)
3	353	OMe	0.86(3)	0.56(5)	3.8(1)
4	363	OMe	0.7(1)	0.50(7)	5.9(1)
5	313	Br	1.38(8)	0.83(6)	1.39(8)
6	323	Br	1.19(5)	0.8(1)	2.7(1)
7	333	Br	1.37(6)	0.76(4)	4.3(2)
8	343	Br	1.16(2)	0.64(5)	7.9(6)
9	293	NO_2	1.64(5)	2.2(3)	2.34(6)
10	303	NO_2	1.5(1)	1.7(2)	5.2(5)
11	313	NO_2	1.66(7)	1.7(3)	8.0(4)
12	323	NO_2	1.45(4)	1.5(1)	15.4(8)

In addition, independent measurements of K_{eq} were obtained by analyzing observed changes in the chemical shift of the aryl and imine catalyst residues (Figure 2.5) as a function of time and [CL], using Eq. 2.2[14] (fits shown in Supporting Information, Figures S8–S10). Comparison of these K_{eq} values with those obtained from the averaged COPASI fits

shows reasonable agreement between the independently calculated parameters (Table 2.1), providing further evidence for the validity of Eq. 2.1 involving pre-equilibrium monomer binding followed by insertion, but other kinetic models described by Eq. 2.1 are also possible (vida infra).

$$\Delta\delta = \Delta\delta_{\text{uncoord}} + \frac{(\Delta\delta_{\text{uncoord}} - \Delta\delta_{\text{coord}})[\text{CL}]}{K_{\text{M}} + [\text{CL}]} \tag{2.2}$$

An induction period was seen in the kinetic runs, as had been noted previously for ROTEP by related aluminum systems, and close inspection of ^{1}H NMR spectra revealed transformations of the catalyst during these early reaction times (cf. $t = 0$ to 1.3 h in Figure 2.5). The initial ^{1}H NMR spectrum obtained soon after mixing of the catalyst with CL contained imine peaks different from those of the catalyst in the absence of CL, suggesting some rapid change of the catalyst structure in the presence of substrate. In addition, these peaks smoothly converted to a second set of peaks as polymerization began. This conversion follows first order kinetics, with a rate that is similar to the rate of polymerization (Supporting Information, S11). The NMR data suggest structural changes to the catalyst and/or precatalyst, possibly including binding of monomer, initiation via isopropoxide insertion, or some other geometric change, but definitive conclusions cannot be drawn with the information currently available

Fig. 2.5 Combined ^{1}H NMR Spectra of Polymerization Over Time

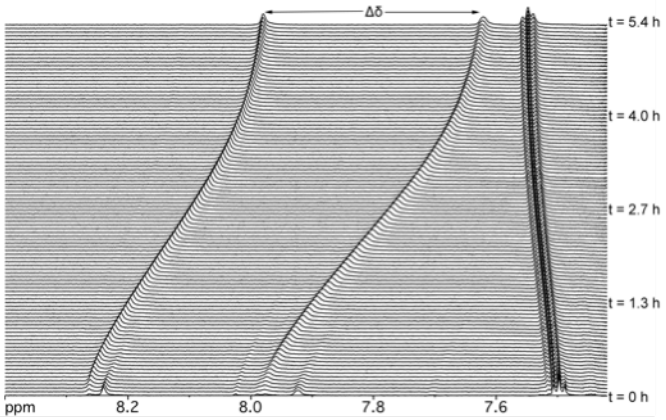

Portion of the ^{1}H NMR spectra acquired during polymerization of CL by **2** (R = Br) at 333 K illustrating how the aryl resonances for the complex in solution changes as a function of reaction time. The indicated peak separation $\Delta\delta$ was used to independently evaluate K_{eq} (see Eq. 2.2). Note the conversion of the catalyst during early reaction times (t = 0–1 h) that is modeled in Supporting Information, Figure S11.

Interpretation of Kinetic Parameters We evaluated the dependencies of K_{eq} and k_2 on the catalyst R group and temperature through Hammett, Eyring, and van't Hoff plots, with the aim of discerning electronic effects and obtaining thermodynamic parameters (Figure 2.6). Turning first to K_{eq}, we find only very weak dependencies on substituent and temperature from plots of log K_{eq} vs. σ_p (Figure 2.6a, red)[34,i] and ln K_{eq} vs $1/T$ (Figure 2.6b), respectively. A linear relationship between $\log(K_{eq})$ and σ_p with a small positive slope ρ (average = 0.16(8)) indicates that the equilibrium constant for monomer binding is slightly enhanced by EWGs, in line with previous explanations for the reactivity of aluminum salen complexes.[8] However, this effect is small, which is highlighted by the small differences in the ΔG° values (Table 2.2) calculated from Figure 2.6b (e.g., the $\Delta\Delta G^\circ$ between **2** with R = OMe and R = Br at 333 K is less than 0.4 kcal/mol).

[i]Values for the rate constants k_2 and K_{eq} at temperatures that were not experimentally measured but presented in Figure 2.6 were obtained by extrapolating the thermodynamic parameters from the Eyring (k_2) and vant Hoff (K_M) plots (see Table 2.2 and 2.3 for thermodynamic parameters).

Table 2.2 Thermodynamic Parameters Associated with K_{eq} for Catalysts **2** Determined by COPASI and NMR Peak Analysis

R	Method	ΔH° (kcal/mol)	ΔS° (cal/(mol·K))	ΔG° (kcal/mol, 323 K)
OMe	COPASI	−2.1 ± 0.9	−7 ± 3	−0.03 ± 1
OMe	NMR	−2.3 ± 0.5	−8 ± 2	0.2 ± 0.7
Br	COPASI	−0.8 ± 0.5	−2 ± 1	−0.2 ± 0.6
Br	NMR	−1.8 ± 0.3	−6 ± 1	0.2 ± 0.5
NO_2	COPASI	−0.5 ± 0.3	−0.8 ± 1	−0.2 ± 0.5
NO_2	NMR	−2.2 ± 0.4	−6 ± 1	−0.2 ± 0.6

For all catalysts studied, ΔG° values are zero within experimental error. Importantly, the small differences in K_{eq} and ΔG° as a function of substituents cannot fully explain the differences in the observed overall rates for this set of catalysts.

Fig. 2.6 Temperature Dependence on K_{eq} and k_2

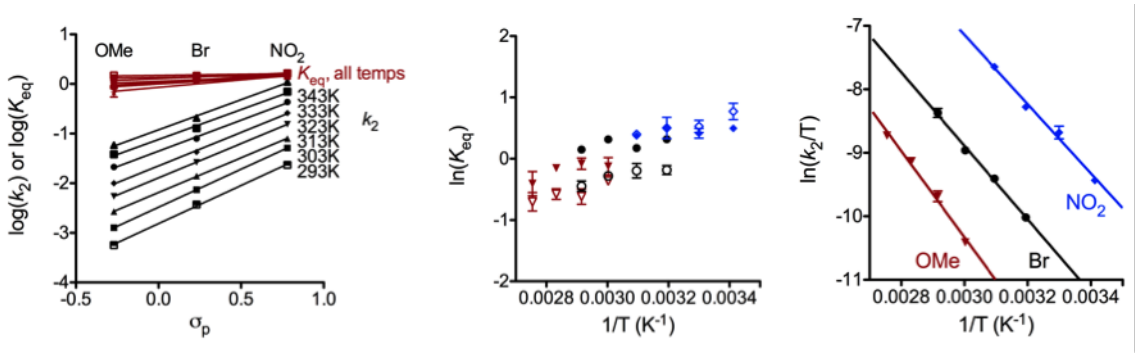

a b c

(a) Hammett plot for k_2 (black) and K_{eq} (red). (b) van't Hoff plot for K_{eq} (R = OMe, red triangles; R = Br, black circles; R = NO_2, blue diamonds). Closed points denote equilibrium constant values determined by COPASI; open points denote values determined by NMR peak analysis method. (c) Eyring plot for k_2 values.

The dependencies of k_2 on substituent R and temperature are more striking (Figures 2.6a, 2.6c), and show that the overall rate differences between the ROTEP polymerizations by catalysts **2** arise from this kinetic parameter. Linear relationships between $log(k_2)$ and

the σ_p values at all temperatures have similar positive slopes (ρ) with an average value of +1.4(1). The linear correlations support a similar mechanism(s) across the series of catalysts, and the positive ρ values reflect enhancement of k_2 with increasing substituent electron withdrawing power. This trend is notably opposite from that reported previously for catalysts **1** ($\rho = -1.1(1)$).[14] Further insight is provided by the activation parameters calculated using the Eyring equation from Figure 2.6c (Table 2.3). A clear trend in both the activation enthalpy and Gibb's free energy of activation that mimics the overall rate order is observed, albeit with no discernible trend in the activation entropies (within error).

Table 2.3 Activation Parameters for k_2

R	$\Delta H^{\ddagger}$ (kcal/mol)	$\Delta S^{\ddagger}$ (cal/(mol·K))	$\Delta G^{\ddagger}$ (kcal/mol, 323 K)
OMe	13.5 ± 0.5	-27 ± 2	22.3 ± 0.8
Br	11.5 ± 0.3	-30 ± 2	21.3 ± 0.7
NO_2	10.8 ± 0.4	-29 ± 2	20.2 ± 0.8

The modest positive activation enthalpies accompanied by negative activation entropies imply a degree of bond breaking and ordering in the transition state consistent with the insertion process, with further understanding made available from DFT calculations (see below).

Density Functional Modeling

Pathway Analysis on Models Lacking para Substituents. To characterize in microscopic detail the various elementary steps associated with the ROTEP mechanism, we began by applying a DFT model that has been extensively validated for organic and main-group inorganic systems (M06-2X/6-311+G(d,p)//M06-L/6-31+G(d,p) including toluene solvation effects using a quantum chemical continuum model; see Computational Methods section for

full details) to a truncated model catalyst from which bulky alkyl substituents were removed (and isopropoxide truncated to methoxide) to facilitate initial identification of important stationary-point structures (denoted **r**, Figure 2.7).[37]

Fig. 2.7 Truncated Model **r** for Catalysts **2**

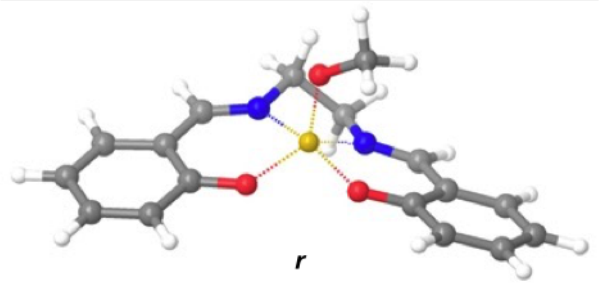

Many complexes of **r** with CL can be found and identified as minima on the potential energy surface (PES). These include van der Waals complexes, with CL "stacking" above or below an aromatic ring, and various structures coordinating either of the two ester oxygen atoms of CL to the aluminum atom. However, while all of these structures are minima on the potential energy surface, they are all predicted to have positive free energies relative to separated reactants, such that product distributions would be expected to follow the Curtin–Hammett principle. As a result, we will therefore begin with a focus primarily on transition-state (TS) structures and their energies. Later, however, we will return to the myriad of catalyst·CL complexes to rationalize what we believe to be substrate-inhibition effects in the observed kinetic.

As noted above, the calculations indicate that monomer coordination to aluminum does *not* generate a significantly stable intermediate that precedes a separate insertion step, (as is often assumed, cf. Figure 2.1, page 9). Nonetheless, the alkoxide and CL must indeed be brought into proximity to accomplish the alkoxide insertion step. Consideration of this step leads to eight stereochemically distinct and mechanistically productive insertion orientations

of the alkoxide and CL relative to the catalyst structure. These eight orientations (Figure 2.8) differ in the orientation of the CL monomer and the orientation of the noncoordinated oxygen (carbonyl or ester) relative to the nitrogen ligands (*trans*/*trans*, *trans*/*cis*, *cis*/*trans*, and *cis*/*cis*) as well as whether coordination occurs through the monomer carbonyl or ester oxygen atom ($O_{carbonyl}$ and O_{ester}, respectively).

Fig. 2.8 Eight Distinct Caprolactone **r** Complexes

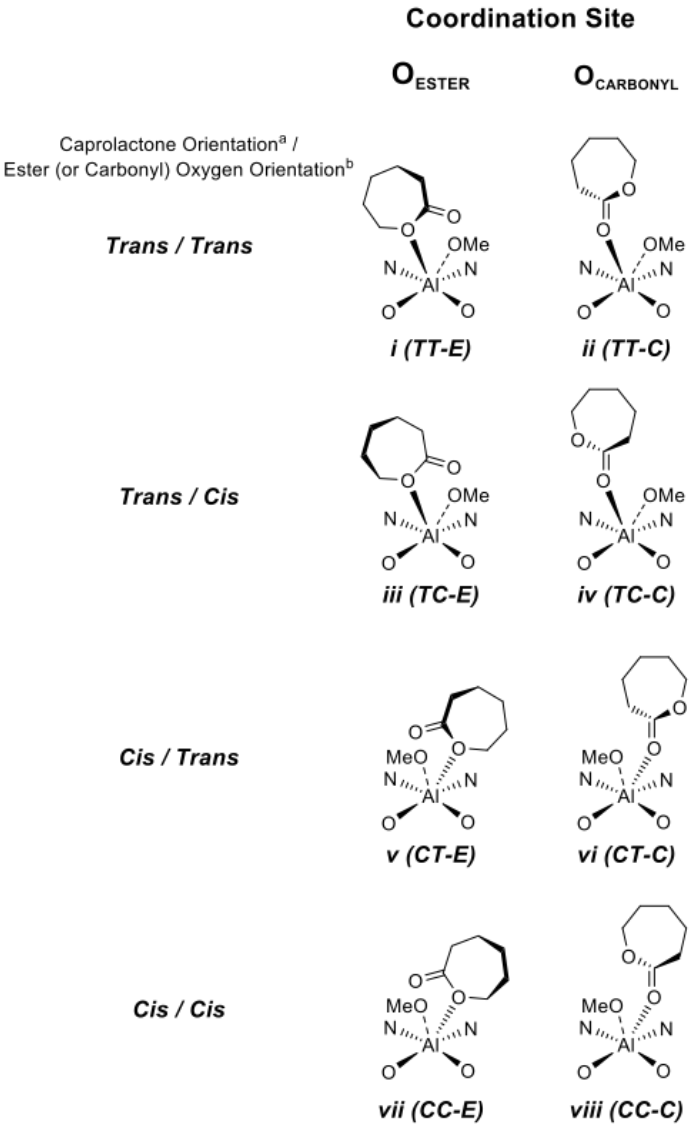

Eight distinct CL **r** complex structures from which alkoxide insertion may proceed; complete geometries are provided in the Supporting Information. [a]Orientation of the CL is given relative to the nitrogen ligands. [b]Orientation of the ester or carbonyl oxygen is given relative to the nitrogen donors.

The ring-opening polymerization proceeds via two distinct mechanistic routes depending on how CL coordinates to the Al center along the insertion pathway. Initial approach involving the ester oxygen (***i***, ***iii***, ***v***, ***vii***) provides access to an alkoxide-insertion TS

structure from which ring-opened product is directly obtained (Supporting Information, Figure S15). By contrast, initial approach involving the carbonyl oxygen (***ii***, ***iv***, ***vi***, ***viii***) leads to an alkoxide-insertion TS structure that generates a reactive orthoalkoxide intermediate (Figure 2.9, first TS). Subsequent exchange of the newly generated alkoxide oxygen and the original ester oxygen, with concomitant ring-opening, then proceeds via a second TS structure that leads to ring-opened product.

Fig. 2.9 Reaction Path for **r-*vi***

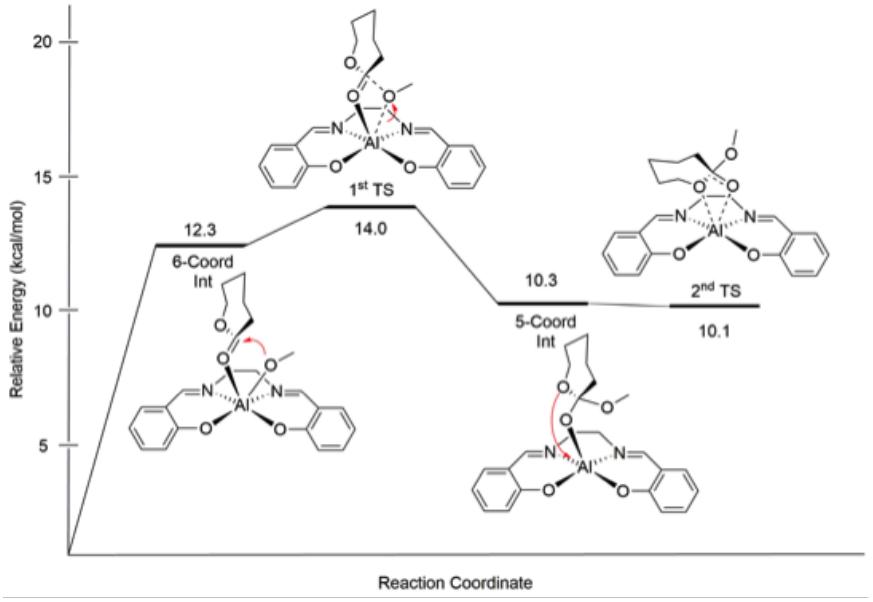

This path is computed to have the lowest activation free energy of eight distinct stereochemical possibilities shown in Figure 2.8

The relative free energies for the key stationary points on all pathways for the truncated model **r** are listed in Tables 2.4 and 2.5 for O_{ester} and $O_{carbonyl}$ coordination, respectively (all structures are provided in Supporting Information; these tables also include data for a more elaborate model s including all experimental alkyl substituents described below). The ring-opening pathway associated with ***vi*** (***CT-C***) was found to have the lowest activation free energy of all eight possible pathways, 14.0 kcal/mol, with the rate limiting step being

the initial alkoxide insertion. Note that the initial 6-coordinate intermediate is 12.3 kcal/mol above separated reactants in free energy, even though it is predicted to be a minimum on the potential energy surface.

Table 2.4 Free Energies (kcal/mol) Relative to Separated Reactants for Reaction Paths Involving O_{ester}–Al Coordination in the Truncated **r** and More Elaborate **s** Models[a]

Orientation	6-coordinate Intermediate	TS Structure
r-*i*	12.9	16.8
s-*i*	16.7	17.7
r-*iii*	11.8	19.5
s-*iii*	17.6	22.2
r-*v*	16.0	16.7
s-*v*	17.9	17.6
r-*vii*	*b*	19.6
s-*vii*	*b*	20.2

[a]See computational methods section for theoretical details. [b]No stationary point preceding the TS structure could be located.

Table 2.5 Free Energies (kcal/mol) Relative to Separated Reactants for Reaction Paths Involving $O_{carbonyl}$–Al Coordination in the Truncated **r** and More Elaborate **s** Models (See Also Figure 2.9)[a]

Orientation	6-coordinate Intermediate	1st Transition State	5-coordinate Intermediate	2nd Transition State
r-*ii*	11.4	17.2	9.2	14.8
s-*ii*	*b*	16.5	7.0	15.3
r-*iv*	11.3	19.3	6.9	7.4
s-*iv*	*b*	18.0	6.2	11.3
r-*vi*^{c}	**12.3**	**14.0**	**10.3**	**10.1**
s-*vi*^{c}	***b***	**14.9**	**10.6**	**12.2**
r-*viii*	8.1	17.3	10.4	15.6
s-*viii*	*b*	17.6	8.7	13.9

[a]See computational methods section for theoretical details. [b]Stationary points were not computed for these structures. [c]This pathway has the lowest rate-limiting activation free energy of the eight stereochemically distinct possibilities.

Also, the orthoalkoxide intermediate is predicted to be a very shallow minimum on the potential energy surface, such that adding thermal contributions to arrive at a free energy leads to the intermediate being effectively degenerate with the second TS structure for ring-opening that generates product alkoxide. As such, the orthoalkoxide is kinetically irrelevant. Cases **r-*i***, **r-*ii***, **r-*v***, and **r-*viii*** have rate-limiting free energies of activation of 15 to 17 kcal/mol, that is, only slightly above that for **r-*vi***. In the remaining cases, **r-*iii***, **r-*iv***, and **r-*vii***, steric clashes between the phenyl rings of the Al-salen complex and the CL ring destabilize the rate-determining TS structures leading to activation free energies above 19 kcal/mol.

With results in hand for the eight pathways associated with model **r**, we next examined the influence of the two *t*-butyl and two methyl groups that are present in the experimental salen ligand by introducing them into the computational model, hereafter referred to as model **s**. The mean unsigned difference between the relative free energies for corresponding stationary points of model **r** vs model **s** (Tables 2.4 and 2.5) is only 1.8 kcal/mol, indicating that most of the relative energies are not especially perturbed by the additional steric bulk in model **s**. However, all of the structures involving coordination to the *ester* oxygen are *destabilized*, because these structures bring the CL ring into closer proximity to the steric bulk of the full catalyst model. Indeed, the 6-coordinate intermediate **s-*iii*** is destabilized by 5.8 kcal/mol relative to the truncated **r** model owing to unfavorable interactions with the methyl groups on the salen bridge. The looser complexes associated with carbonyl oxygen coordination are by contrast in some cases *stabilized* by favorable dispersion interactions (i.e., attractive London forces at van der Waals contact), for example, the 5-coordinate intermediate **s-*ii*** whose relative energy is 2.2 kcal/mol more stable than that of **r-*ii***. As might be expected given the small mean unsigned difference between models **r** and **s**, we find that again the lowest energy pathway upon inclusion of the alkyl substitution is pathway ***vi*** (Figure 2.10), with a rate-limiting free energy of activation of 14.9 kcal/mol, which is slightly

increased from the 14.0 kcal/mol value obtained with model **r**.

Fig. 2.10 Lowest-Energy Pathway Corresponding to **s**-***vi*** Pathway

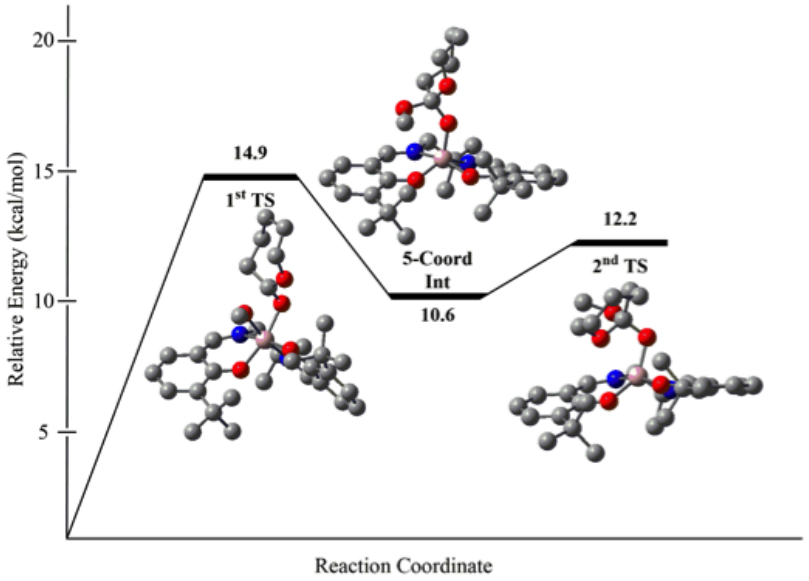

Influence of para Substituents on the Reaction Pathways. Having assessed the effect of additional steric bulk in the salen ligand, we examine next the electronic effects observed with *para* substitution. The same eight pathways (***i***–***viii***) were investigated for the **s** model substituted with *p*-MeO, *p*-Br, and *p*-NO_2, corresponding to the experimental systems **2**. In addition, we chose to use ethoxide in place of methoxide to mimic more accurately a growing polymer chain.

There are some general trends to be observed for the ester coordination pathway (Table 2.6).

Table 2.6 Free Energies (kcal/mol) Relative to Separated Reactants for Reaction Paths Involving O_{ester}–Al Coordination in Full *para*-Substituted Models[a]

Orientation	6-coordinate Intermediate	TS Structure
i-OMe	14.3	17.4
i-Br	12.4	16.7
i-NO$_2$	11.6	16.0
iii-OMe	17.7	23.8
iii-Br	15.6	22.0
iii-NO$_2$	15.8	21.7
v-OMe	16.6	18.3
v-Br	15.6	15.6
v-NO$_2$	13.6	16.3
vii-OMe	*b*	22.1
vii-Br	*b*	20.3
vii-NO$_2$	*b*	20.6

[a]See computational methods section for theoretical details. [b]No stationary points preceding the TS structure could be located

The lactone-coordinated intermediate is stabilized by substitution at the *para* position for all pathways and substitutions. With increasing electron-withdrawing power of the substituent (OMe < Br < NO_2), the intermediate is further stabilized (mean unsigned difference between the model **s** and each substituent is 1.3, 2.9 and 3.7 kcal/mol respectively), consistent with the increased Lewis acidity of the Al atom that is expected with aryl rings substituted by more EWGs. That increased Lewis acidity may be assessed through the evaluation of the CM5 partial atomic charge[38] of the Al atom, which increases smoothly from 0.535 to 0.538 and 0.544 with the substituent going from MeO to Br to NO_2.

For the subsequent TS structures, the *para*-methoxy substituted compounds show mixed results with some pathways being stabilized and some destabilized, over a range of −0.3 to

1.9 kcal/mol relative to unsubstituted **s** results above (cf. Table 2.5, page 23). In the case of *p*-Br, the range is −2.0 to 0.1, and in the case of *p*-NO_2, it is −1.7 to 0.4. The variability in the *para* substitution effect in these systems may be associated with varying degrees of dissociative character in the separation of the nucleophile alkoxide *from* the aluminum atom (which would be expected to be *disfavored* by EWGs) and associative character of the newly formed alkoxide *to* the aluminum atom (which would be favored by the same EWGs). The varying geometries associated with each path permit such differentiation. However, as the free energies of activation in Table 2.6 considerably exceed those associated with carbonyl coordination (vide infra) we will not explore these trends further.

Consistent with the results for the **r** and **s** models above, pathway ***vi*** in the carbonyl coordination pathway case was found to have the lowest rate-limiting free energy of activation (Table 2.7), and to show a trend in relative activation free energies relative to *p*-MeO of −1.2 for *p*-Br, and −2.8 for *p*-NO_2. These free energy differences are in agreement with those measured (-1.0 ± 1.1 and -2.1 ± 1.1, respectively; derived from Table 2.3) to within experimental uncertainty.

Table 2.7 Free Energies (kcal/mol) Relative to Separated Reactants for Reaction Paths Involving $O_{carbonyl}$–Al Coordination in Full *para*-Substituted Models[a]

Orientation	1st Transition State	5-coordinate Intermediate	2nd Transition State
ii-OMe	21.7	8.9	17.1
ii-Br	21.9	8.3	13.5
ii-NO$_2$	18.4	9.0	15.1
iv-OMe	19.2	6.3	11.1
iv-Br	20.2	6.2	14.5
iv-NO$_2$	19.0	5.3	9.2
vi-OMe[b]	**14.3**	**11.5**	**12.3**
vi-Br[b]	**13.1**	**10.8**	**10.4**
vi-NO$_2$[b]	**11.5**	**11.5**	**10.6**
viii-OMe	20.0	9.0	15.2
viii-Br	18.4	7.8	15.2
viii-NO$_2$	17.9	8.2	10.9

[a]See computational methods section for theoretical details. [b]These pathways have the lowest rate-limiting activation free energies of the eight stereochemically distinct possibilities.

Analysis of the geometries along pathway ***vi*** indicates that substitution with increasingly EWGs in the salen ligand leads to an increasingly more compact coordination of the reactants in the rate-determining TS structure. Thus, the Al–O bond distances to the carbonyl group of the incoming cyclic ester are 1.929, 1.912 and 1.892 Å, respectively, for the complexes with *p*-MeO, -Br, and -NO_2 substituents, respectively. Concomitantly, the C–O distances for the forming bond between the carbonyl carbon and the ethoxide nucleophile are 1.784, 1.769 and 1.744 Å, respectively (the Al–O bond distance to the methoxide varies by less than 0.005 Å over the different substitutions). Thus, it appears that the more electrophilic Al center best stabilizes the incipient tetrahedral intermediate character in the TS structure, thereby effecting the observed rate acceleration.

While the predicted free energies of activation show a trend with respect to substitution that agrees well with experiment, they are considerably smaller in absolute magnitude than those measured experimentally. Comparison of the enthalpic and entropic contributions to the theoretical free energies relative to the experimental values indicates that theory predicts much smaller *enthalpies* of activation, but much larger *entropies* of activation. Such behavior might be associated with either or both of two phenomena. First, in the actual polymerization process, the growing polymer chain may associate with the catalyst, either through noncovalent interactions or through coordination of oxygen functionality to aluminum, and the requirement that the chain be displaced by CL would be expected to increase the enthalpy of activation and decrease the entropy of activation. Similarly, solvent toluene could enjoy particularly favorable π-stacking interactions with the aromatic rings of the salen ligand, for example, again introducing a larger enthalpy of activation and a less unfavorable entropy of activation (owing to solvent release) associated with reaction CL. In the absence of detailed (and impractical) simulations including solvent and an actual polymer chain, however, it is difficult to do more than speculate about these possibilities.

Also, as noted above, a key finding from the DFT calculations is *unfavorable* free energies for prereactive complexes that are implicated by the usual interpretation of the Michaelis-Menten equation (Eq. 2.1), wherein a pre-equilibrium substrate binding step (K_{eq}) is followed by a catalytic turnover step (k_2; Figure 2.11).

Fig. 2.11 Proposed ROTEP Mechanisms

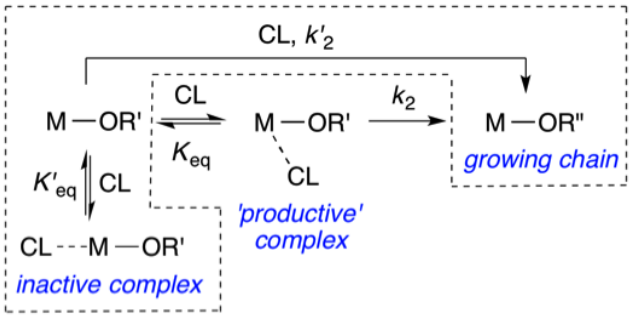

Proposed ROTEP mechanisms that yield the rate law described by Eq. 2.1 M = [(salen)Al] moiety.

To reconcile the experimentally observed rate law (Eq. 2.1) with the absence of such a binding step from the calculated reaction trajectories, we propose a different mechanism involving *substrate inhibition* (steps enclosed by dashed line in Figure 2.11, characterized by K'_{eq} and k'_2) that yields an experimental rate law indistinguishable from Eq. 2.1 (see Supporting Information for derivation). According to this mechanism, reversible substrate binding can be *non*productive, owing to formation of an *inactive* species. This species would be expected to be favored at high CL concentrations, resulting in rate retardation under these conditions (saturation kinetics). One such complex that can be imagined involves coordination of CL to Al trans to the alkoxide ligand, generating a complex that could not lead to intramolecular nucleophilic attack. Many such 6-coordinate Al(salen) complexes are known.[ii] To specifically explore this possibility in our system, we computed the structure of the relevant complex for the *p*-NO_2 substituted salen case (Figure 2.12). It has a free energy that is 8.4 kcal/mol lower than any of the productively coordinated species presented in Tables 2.4 and 2.5.

[ii] A search of the Cambridge Crystallographic Database (v. 5.34) revealed >20 such structures. See references for some illustrative examples[39–41]

Fig. 2.12 Unproductive Complex of Caprolactone with p-NO_2 Catalyst

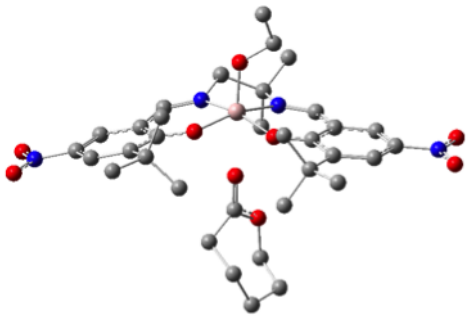

In addition, while not shown, we also located various van der Waals complexes of CL with the aromatic portions of the salen ligand that were also predicted to have lower free energies than productively coordinated complexes (adjacent to the alkoxide ligand). A quantitative measure of the inhibitory effect would require a statistical average over all nonproductive complexes, which is not practical in the absence of detailed molecular simulations. Nevertheless, the substrate inhibition mechanism (steps $K_{eq}^{'}$ and $k_2^{'}$) is consistent with the experimental kinetics, and provides an alternative to the assumption in the pre-equilibrium mechanism that K_{eq} refers to productive coordination of substrate as a separate step prior to alkoxide insertion. Indeed, the substrate inhibition model represents a potentially important general phenomenon in ROTEP with catalysts for which both productive and unproductive coordination geometries of substrate and catalyst are available.

As a final, technical point related to the modeling, we note that use of the M06-L functional, with its well established ability to account for attractive medium-range electron correlation effects (sometimes informally referred to as "dispersion", although that term really should only be used for longer-range attractive effects varying as r^{-6} with distance), is critical for the determination of accurate catalyst-CL complex geometries. When the 6-coordinate precursor structure corresponding to **r-*vi*** is reoptimized with the B3LYP functional, for example, which does not account for medium-range correlation effects, the

bond distance between the carbonyl oxygen and the aluminum atom changes from the M06-L value of 2.18 Å to a value of 4.89 Å, i.e., the CL fully decoordinates.

2.1.3 Summary and Conclusions

Detailed kinetic studies of the polymerization of CL by salen-aluminum catalysts **2** (R = OMe, Br, or NO_2) supported by ligands with similar steric profiles but different electron donating characteristics revealed saturation behavior that fits to the rate Eq. 2.1. While K_{eq} varied only slightly with the electron donating properties of R (Hammett $\rho = +0.16(8)$), k_2 showed a more significant dependence reflected by $\rho = +1.4(1)$. These conclusions were buttressed by the dependencies of K_{eq} and k_2 with temperature that led to essentially invariant ΔG° values of 0 kcal/mol for all catalysts (Table 2.2, page 17) and a discernible trend in $\Delta H^\ddagger$ of R = OMe > Br > NO_2 (Table 2.3, page 18). The observation of faster rates with EWGs on the supporting ligand agrees with the results of previous studies of ROTEP reactions catalyzed by related salen-aluminum complexes.[8,9]

The lowest energy reaction trajectories calculated by DFT (**r** and **s-*vi***) have similarities to those proposed for ROTEP of LA stereoisomers by (β-diketiminate)-Zn and -Sn catalysts,[42,43] in particular with respect to the first transition state structure that features incipient attack of the nucleophile to the lactone carbonyl that is bound to the metal ion. With respect to the effects of the remote ligand substituents, both the trend and the free energy of activation differences observed experimentally are reproduced in pathway ***vi***. The greater Lewis acidity of the electron-deficient metal ion accelerates the reaction via transition state stabilization that involves increased bonding between the Al ion and the lactone carbonyl and between the nucleophilic alkoxide and the lactone carbonyl carbon.

Interestingly, DFT calculations indicated that a distinct CL adduct is not a free energy

minimum on the reaction pathway, arguing against K_{eq} being associated with productive coordination of monomer according to the typical coordination-insertion mechanism (Figures 2.1 and 2.11). Instead, we propose that K_{eq} corresponds to "nonproductive" coordination of substrate that inhibits the reaction at high substrate concentrations, with k_2 thus encompassing both "productive" coordination and insertion steps that occur smoothly along the reaction trajectory. This attribution of saturation behavior to monomer inhibition has potentially significant implications for the interpretation of mechanistic studies of ROTEP catalysis and for the design of new catalysts. For example, we predict that catalysts for which nonproductive monomer coordination is prevented may be particularly efficient, particularly when high monomer concentrations are used (e.g., neat or in the melt).

2.1.4 Experimental Section

General Considerations All reactions were carried out under an inert atmosphere using standard Schlenk and drybox techniques, unless otherwise indicated. Reagents were obtained from commercial suppliers and used as received unless otherwise indicated. CL was purified by distillation from CaH_2 and stored under N_2. Deuterated solvents were dried over CaH_2 or sodium, distilled under vacuum and stored under N_2. Protiated solvents were degassed and passed through a solvent purification system (Glass Contour, Laguna, CA) prior to use. ^{1}H and ^{13}C NMR spectra were recorded on a Varian VI-300 NMR spectrometer or a Bruker Avance III 500 MHz spectrometer equipped with a BBFO SmartProbe, and their chemical shifts (δ) for ^{1}H and ^{13}C spectra are referenced to residual protium in the deuterated solvent (for ^{1}H) and deuterated solvent itself (for ^{13}C). Chemical shifts for ^{27}Al NMR were externally referenced to aluminum tris(acetylacetonate)[44] in toluene-d_8. 2-hydroxy-3-(*tert*-butyl)-5-bromobenzaldehyde,[45] and 2-hydroxy-3-(*tert*-butyl)-5-nitrobenzaldehyde[46] were synthesized according to literature procedures. Elemental analyses were performed by Complete Analysis

Laboratories, Inc., Parsippany, NJ.

Ligand Synthesis The benzaldehyde (H_2L^{OMe}: 7.7 g, 83% pure, 31 mmol; H_2L^{Br}: 1.40 g, 5.44 mmol; $H_2L^{NO_2}$: 1.61 g, 88% pure, 6.35 mmol) was added to a round-bottom flask with the appropriate amount of absolute ethanol to give 0.63 M benzaldehyde. 2-methylpropane-1,2-diamine (0.5 equiv) was added in one portion to the flask with stirring. A reflux condenser was added and the mixture was refluxed at 100 °C for 2 h, then allowed to cool to room temperature. The crude solution was placed in a −30 °C freezer overnight to induce precipitation of the protonated form of the ligand. After recovery by filtration washing with 40 mL of hexanes and in the case of H_2L^{Br}, recrystallization from dichloromethane and hexanes at −30 °C overnight, the solid product was placed in a vacuum oven overnight before bringing into the glovebox for metalation. Yield: H_2L^{OMe}: 5.62 g, 98%; H_2L^{Br}: 1.08 g, 35%; $H_2L^{NO_2}$: 1.38 g, 87%). H_2L^{OMe}: ^{1}H NMR (500 MHz, $CDCl_3$) δ 13.95 (s, 1H, O*H*), 13.42 (s, 1H, O*H*), 8.35 (s, 1H, C*H*═N), 8.31 (s, 1H, C*H*═N), 6.96 (app t, J = 3.37 Hz, 2H, Ar*H*), 6.60 (d, J = 3 Hz, 1H, Ar*H*), 6.58 (d, J = 3 Hz, 1H, Ar*H*), 3.76 (s, 3H, ArOMe), 3.75 (s, 3H, ArOMe), 3.72 (s, 2H, NCH_2C$(CH_3)_2$N), 1.44 (s, 6H, NCH_2C(CH_3)$_2$N), 1.42 (s, 9H, Ar*t-Bu*), 1.41 (s, 9H, Ar*t-Bu*); ^{13}C NMR (125 MHz, $CDCl_3$) δ 167.26, 162.37, 155.32, 155.13, 151.31, 151.24, 139.15, 139.14, 118.61, 118.42, 118.09, 117.99, 111.72, 111.62, 70.57, 60.28, 55.91, 35.14, 35.12, 29.41, 29.39, 25.69. Anal. Calcd for $C_{28}H_{40}N_2O_2$: C, 71.76; H, 8.60; N, 5.98. Found: C, 71.73; H, 8.57; N, 5.98.

H_2L^{Br}: ^{1}H NMR (500 MHz, CDCl3) δ 14.39 (s, 1H, O*H*), 13.83 (s, 1H, O*H*), 8.29 (s, 1H, C*H*═N), 8.25 (s, 1H, C*H*═N), 7.37 (d, J = 2.5 Hz, 1H, Ar*H*), 7.36 (d, J = 2 Hz, 1H, Ar*H*), 7.23 (d, J = 2.5 Hz, 1H, Ar*H*), 7.20 (d, J = 2.5 Hz, 1H, Ar*H*), 3.72 (s, 2H, NCH_2C$(CH_3)_2$N), 1.43 (s, 6H, NCH_2C(CH_3)$_2$N), 1.40 (s, 18H, Ar*t-Bu*); ^{13}C NMR (125 MHz, $CDCl_3$) δ 166.37, 161.45, 159.97, 159.69, 140.32, 140.29, 132.63, 132.39, 131.98, 131.84, 119.98, 119.91, 109.90, 109.70, 70.35, 60.45, 35.25, 35.23, 29.25, 25.55. Anal. Calcd for

$C_{26}H_{34}Br_2N_2O_2$: C, 55.14; H, 6.05; N, 4.95. Found: C, 55.08; H, 6.09; N, 4.90.

$H_2L^{NO_2}$: ^{1}H NMR (500 MHz, $CDCl_3$) δ 15.68 (s, 1H, O*H*), 14.94 (s, 1H, O*H*), 8.43 (app s, 2H, C*H*═N), 8.23 (d, J = 2.5 Hz, 1H, Ar*H*), 8.20 (d, J = 2.5 Hz, 1H, Ar*H*), 8.13 (d, J = 2.5 Hz, 1H, Ar*H*), 8.12 (d, J = 3 Hz, 1H, Ar*H*), 3.82 (s, 2H, NCH_2C$(CH_3)_2$N), 1.54 (s, 2H, NCH_2C$(CH_3)_2$N), 1.52 (s, 6H, NCH_2C$(CH_3)_2$N), 1.43 (s, 9H, Ar*t-Bu*), 1.42 (s, 9H, Ar*t-Bu*); ^{13}C NMR (125 MHz, $CDCl_3$) δ 168.59, 167.12, 166.73, 161.83, 140.26, 139.93, 139.02, 126.90, 126.44, 125.39, 117.19, 116.78, 69.47, 60.47, 70.35, 60.45, 35.45, 35.41, 29.07, 25.45. Anal. Calcd for $C_{26}H_{34}N_4O_6$: C, 62.63; H, 6.87; N, 11.24. Found: C, 62.54; H, 6.67; N, 11.15.

Aluminum Complexes (2) In a nitrogen-filled glovebox, equimolar amounts of the pro-ligand (H_2L^{OMe}: 0.596 g, 1.27 mmol; H_2L^{Br}: 0.719 g, 1.27 mmol; $H_2L^{NO_2}$: 0.778 g, 1.56 mmol) and aluminum tris(*iso*-propoxide) were added to an oven-dried 15 mL screw cap glass vessel. Toluene (3 mL) was added, and the vessel was equipped with a stir bar, sealed, and removed from the glovebox. The sealed vessel was heated to 90 °C for 3 days, after which time it was cooled to room temperature and returned to the glovebox. Toluene was removed in vacuo from the homogeneous solutions to yield the products as a colored powder (R = OMe: bright yellow; R = Br: yellow; R = NO_2: light brown). The powder was triturated with pentane and collected by filtration through a glass frit. In the cases of R = Br and NO_2, the solid was dried on a vacuum line overnight and used without further purification. The resulting solid in the case of R = OMe was recrystallized from toluene/pentane at −40 °C, and the crystals were dried overnight on a vacuum line before use. Yields: R = OMe: 0.591 g (84%); R = Br: 0.712 g (86%); R = NO_2: 0.879 g (97%).

R = OMe: ^{1}H NMR (500 MHz, toluene-d_8) δ 7.93 (s, 1H, C*H*═N), 7.45 (s, 1H, C*H*═N), 7.38 (d, J = 3 Hz, 1H, Ar*H*), 7.36 (d, J = 3 Hz, 1H, Ar*H*), 6.38 (d, J = 3 Hz, 1H, Ar*H*),

6.27 (d, J = 2.6 Hz, 1H, ArH), 4.15 (q, J = 6 Hz, 1H, OCHH(CH$_3$)$_2$), 3.75 (d, J = 12 Hz, 1H, NCH_2C(CH$_3$)$_2$N), 3.52 (s, 3H, ArOMe), 3.49 (s, 3H, ArOMe), 2.47 (d, J = 12 Hz, 1H, NCH_2C(CH$_3$)$_2$N), 1.76 (s, 9H, Art-Bu), 1.74 (s, 9H, Art-Bu), 1.17 (d, J = 6.0 Hz, 3H, OCH(CH_3)$_2$), 1.11 (s, 3H, NCH$_2$C(CH_3)$_2$N), 1.10 (d, J = 6.3 Hz, 3H, OCH(CH_3)$_2$), 0.62 (s, 3H, NCH$_2$C(CH_3)$_2$N); ^{27}Al NMR (130 MHz, toluene-d_8) δ 35.23. Anal. Calcd for $C_{31}H_{45}AlN_2O_5$: C, 67.37; H, 8.21; N, 5.07. Found: C, 67.43; H, 8.23; N, 4.98.

R = Br: ^{1}H NMR (500 MHz, toluene-d_8) δ 7.70 (d, J = 2.7 Hz, 1H, ArH), 7.69 (d, J = 2.8 Hz, 1H, ArH), 7.64 (s, 1H, CH═N), 7.18 (s, 1H, CH═N), 6.97 (d, J = 2.6 Hz, 1H, ArH), 6.91 (d, J = 2.6 Hz, 1H, ArH), 4.05 (q, J = 5.9 Hz, 1H, OCH(CH$_3$)$_2$), 3.65 (d, J = 12.3 Hz, 1H, NCH_2C(CH$_3$)$_2$N), 2.39 (d, J = 12.2 Hz, 1H, NCH$_2$C(CH_3)$_2$N), 1.65 (s, 9H, Art-Bu), 1.63 (s, 9H, Art-Bu), 1.15 (d, J = 6.0 Hz, 3H, OCH(CH_3)$_2$), 1.06 (d, J = 6.3 Hz, 3H, OCH(CH_3)$_2$), 1.06 (s, 3H, NCH$_2$C(CH_3)$_2$N), 0.57 (s, 3H, NCH$_2$C(CH_3)$_2$N); ^{27}Al NMR (130 MHz, toluene-d_8) δ 34.11. Anal. Calcd for $C_{29}H_{39}AlBr_2N_2O_3$: C, 53.55; H, 6.04; N, 4.31. Found: C, 53.60; H, 6.08; N, 4.31.

R = NO$_2$: ^{1}H NMR (500 MHz, toluene-d_8) δ 8.49 (d, J = 2.1 Hz, 1H, ArH), 8.48 (d, J = 2.3 Hz, 1H, ArH), 7.92 (d, J = 2.4 Hz, 1H, ArH), 7.76 (d, J = 2.3 Hz, 1H, ArH), 7.66 (s, 1H, CH═N), 7.10 (s, 1H, CH═N), 3.96 (q, J = 5.7 Hz, 1H, OCH(CH$_3$)$_2$), 3.59 (d, J = 12.4 Hz, 1H, NCH_2C(CH$_3$)$_2$N), 2.43 (d, J = 12.3 Hz, 1H, NCH_2C(CH$_3$)$_2$N), 1.62 (s, 9H, Art-Bu), 1.60 (s, 9H, Art-Bu), 1.10 (d, J = 5.8 Hz, 3H, OCH(CH_3)$_2$), 1.04 (s, 3H, NCH$_2$C(CH_3)$_2$N), 1.03 (d, J = 6.3 Hz, 3H, OCH(CH_3)$_2$), 0.58 (s, 3H, NCH$_2$C(CH_3)$_2$N); ^{27}Al NMR (130 MHz, toluene-d_8) δ 33.07. Anal. Calcd for $C_{29}H_{39}AlN_4O_7$: C, 59.78; H, 6.75; N, 9.62. Found: C, 59.78; H, 6.78; N, 9.62.

^{1}H NMR Kinetics A representative procedure for the kinetic studies is described. To an oven-dried NMR tube in a nitrogen-filled glovebox, 500 µL of a stock solution of catalyst in

toluene-d_8 (0.0092 M) and 10 µL of the internal standard bis(*para*-trimethylsilyl)benzene in toluene-d_8 (0.28 M) were added. The NMR tube was capped with a septum and wrapped with parafilm. A gastight syringe was loaded with 190 µL of ε-caprolactone (CL) stock solution (7.4 M), also in toluene-d_8. The target final concentrations of catalyst, internal standard, and CL were 0.0062 M, 0.004 M, and 2 M, respectively. The gastight syringe containing CL was inserted into a rubber septum to prevent air contamination during the experiment setup. The NMR tube and syringe were removed from the glovebox and brought to the spectrometer. The temperature on the NMR spectrometer (300 MHz Varian Inova) was calibrated using an ethylene glycol standard. A ^{1}H NMR spectrum was taken of the initial catalyst and internal standard solution before addition of CL with a relaxation time of 10 s and a 30° pulse width to ensure complete relaxation for quantitative integrations to determine catalyst concentration. Next, the tube was ejected from the spectrometer and CL was injected through the septum into the NMR tube, and the time between CL injection and start of the ^{1}H NMR data acquisition was recorded in minutes. The contents of the tube were well mixed before reinserting the NMR tube into the spectrometer. Again, a relaxation time of 10 s and a 30° pulse width were used for quantitative purposes, and an arrayed set of spectra were taken every 96, 192, or 384 s with 8, 16, or 32 scans, respectively, spin rate of 16 Hz, acquisition time 2 s, and maximum gain. The arrayed experiment was allowed to proceed until polymerization had completed, as indicated by the disappearance of the CL peaks. For each catalyst, four temperatures were carefully chosen, and three reactions were repeated at each temperature. The obtained arrayed NMR data were phased and baseline corrected in Mestrenova (http://mestrelab.com/) before being integrated by the same program. The integrations were recorded and entered into an Excel spreadsheet. Absolute concentrations of all species as a function of time were computed relative to the concentration of internal standard. Reaction time was calculated in seconds from the known length of time per spectrum and the time between CL injection and the start of the ^{1}H NMR data acquisition. The concentration vs time data obtained from the ^{1}H NMR data were

input into the COPASI program and fit to Eq. 2.2 to obtain K_M and k_2 values. COPASI fitting plots (concentration vs time) are shown in Supporting Information, Figure S1. The reaction rates were calculated by Eq. 2.2 and plotted as a function of concentration, as shown in Supporting Information, Figure S2. Kinetic parameters determined by COPASI are listed in Supporting Information, Table S1. All linear and nonlinear curve fits were performed using Graphpad Prism software. In a test of the significance of possible viscosity effects on the kinetics performed in the NMR tubes, a stirred polymerization using **2** (R = NO_2) at 298 K (average temperature inside nitrogen-filled glovebox over the course of the reaction) with [**2** (R = NO_2)]$_{tot}$ = 5.8 mM and [CL]$_0$ = 2 M (total volume 5 mL). Aliquots were removed at selected time points for NMR analysis, which revealed rate parameters similar to those seen in the NMR tube experiments (see Supporting Information for details).

Density Functional Calculations All stationary molecular geometries were fully optimized in the gas phase at the M06-L level of DFT[47] employing the 6-31+G(d,p) basis set[48] in the Gaussian09 electronic structure program suite.[49] The nature of individual stationary points, that is, their characterization as either minima or TS structures, was verified by the computation of analytical vibrational frequencies. These same calculations, within the conventional ideal-gas, rigid-rotator, quantum-mechanical harmonic-oscillator (QMHO) approximation,[50] permitted the computation of thermal contributions to 323.15 K free energies. To compensate for errors in the QMHO approximation when applied to very low-frequency normal modes, vibrational frequencies below 50 cm^{-1} were replaced by values of 50 cm^{-1} (the quasi-harmonic approximation[51]). The effects of toluene as solvent were included through calculations at the same level of theory using the SMD quantum-mechanical continuum solvation model for the gas-phase optimized structures. In select instances, we explored the influence of reoptimization of the geometries including solvation and determined that the effects were small, and insofar as geometric convergence was considerably slower

with the solvation model included, we restricted our consideration to gas-phase structures. Final, best-estimate composite free energies in solution were computed by replacing the M06-L/6-31+G(d,p) gas-phase electronic energies with single-point electronic energies computed using the M06-2X density functional[52] and the 6-311+G(d,p) basis set.[48] Minima connected through individual TS structures were determined by displacing the geometries of TS structures by small amounts in both directions along their corresponding reaction coordinates and permitting the resulting structures to optimize to their associated minima.

2.1.5 Associated Content

Experimental data, analysis (comparison to alternative rate law fits, error evaluation), and theory details (PDF). This material is available free of charge via the Internet at http://pubs.acs.org.

2.1.6 Notes

The authors declare no competing financial interest.

2.1.7 Acknowledgments

This work was supported by the Center for Sustainable Polymers at the University of Minnesota, a National Science Foundation (NSF) supported Center for Chemical Innovation (CHE-1136607), and by NSF grants to D.J.M. and C.J.C. (CHE-0952054), an NSF graduate research fellowship to M.O.M. (Grant 00006595), a CONACYT postdoctoral grant to H. V.-L. (Grant 186695), and UM Lando and Heisig grants in support of undergraduate student research (Y.D. and M.A.J.).

References

[1] Gandini, A. *Macromolecules* **2008**, *41*, 9491–9504.

[2] *Renewable Polymers: Synthesis, Processing, and Technology*; John Wiley & Sons and Scrivener Publishing: Hoboken, NJ and Salem, MA, 2012.

[3] Drumright, R. E.; Gruber, P. R.; Henton, D. E. *Adv. Mater.* **2000**, *12*, 1841–1846.

[4] Wu, J.; Yu, T.-L.; Chen, C.-T.; Chu, C.-C. *Coord. Chem. Rev.* **2006**, *250*, 602–626.

[5] Dechy-Cabaret, O.; Martin-Vaca, B.; Bourissou, D. *Chem. Rev.* **2004**, *104*, 6147–6176.

[6] O'Keefe, B. J.; Hillmyer, M. A.; Tolman, W. B. *J. Chem. Soc., Dalton Trans.* **2001**, 2215–2224.

[7] Kamber, N. E.; Jeong, W.; Pratt, R. C.; Lohmeijer, B. G. G.; Waymouth, R. M.; Hedrick, J. L. *Chem. Rev.* **2007**, *107*, 5813–5840.

[8] Hormnirun, P.; Marshall, E. L.; Gibson, V. C.; Pugh, R. I.; White, A. J. P. *Proc. Natl. Acad. Sci. U.S.A.* **2006**, *103*, 15343–15348.

[9] Nomura, N.; Ishii, R.; Yamamoto, Y.; Kondo, T. *Chem. Eur. J.* **2007**, *13*, 4433–4451.

[10] Wang, Y.; Ma, H. *Chem. Commun.* **2012**, *48*, 6729–6731.

[11] Gregson, C. K. A.; Blackmore, I. J.; Gibson, V. C.; Long, N. J.; Marshall, E. L.; White, A. J. P. *Dalton Trans.* **2006**, 3134–3140.

[12] Wu, J.; Chen, Y.-Z.; Hung, W.-C.; Lin, C.-C. *Organometallics* **2008**, *27*, 4970–4978.

[13] Alcazar-Roman, L. M.; O'Keefe, B. J.; Hillmyer, M. A.; Tolman, W. B. *Dalton Trans.* **2003**, 3082–3087.

[14] Ding, K.; Miranda, M. O.; Moscato-Goodpaster, B.; Ajellal, N.; Breyfogle, L. E.; Hermes, E. D.; Schaller, C. P.; Roe, S. E.; Cramer, C. J.; Hillmyer, M. A.; Tolman, W. B. *Macromolecules* **2012**, *45*, 5387–5396.

[15] Cozzi, P. G. *Chem. Soc. Rev.* **2004**, *33*, 410–421.

[16] Che, C. *Coord. Chem. Rev.* **2003**, *242*, 97–113.

[17] Spassky, N.; Wisniewski, M.; Pluta, C.; Borgne, A. L. *Macromol. Chem. Phys.* **1996**, *197*, 2627–2637.

[18] Ovitt, T. M.; Coates, G. W. *J. Am. Chem. Soc.* **1999**, *121*, 4072–4073.

[19] Ovitt, T. M.; Coates, G. W. *J. Polym. Sci., Part A: Polym. Chem.* **2000**, 4686–4692.

[20] Ovitt, T. M.; Coates, G. W. *J. Am. Chem. Soc.* **2002**, *124*, 1316–1326.

[21] Radano, C. P.; Baker, G. L.; Smith, M. R. *J. Am. Chem. Soc.* **2000**, *122*, 1552–1553.

[22] Majerska, K.; Duda, A. *J. Am. Chem . Soc.* **2004**, *126*, 1026–1027.

[23] Breteler, M. R. T.; Zhong, Z.; Dijkstra, P. J.; Palmans, A. R. A.; Peeters, J.; Feijen, J. *J. Polym. Sci. A Polym. Chem.* **2006**, *45*, 429–436.

[24] Zhong, Z.; Dijkstra, P. J.; Feijen, J. *J. Am. Chem . Soc.* **2003**, *125*, 11291–11298.

[25] Yang, J.; Yu, Y.; Li, Q.; Li, Y.; Cao, A. *J. Polym. Sci. A: Polym. Chem.* **2004**, *43*, 373–384.

[26] Chisholm, M. H.; Patmore, N. J.; Zhou, Z. *Chem. Commun.* **2005**, 127–129.

[27] Chisholm, M. H.; Gallucci, J. C.; Quisenberry, K. T.; Zhou, Z. *Inorg. Chem.* **2008**, *47*, 2613–2624.

[28] van der Meulen, I.; Gubbels, E.; Huijser, S.; Sablong, R. l.; Koning, C. E.; Heise, A.; Duchateau, R. *Macromolecules* **2011**, *44*, 4301–4305.

[29] Pepels, M. P. F.; Bouyahyi, M.; Heise, A.; Duchateau, R. *Macromolecules* **2013**, *46*, 4324–4334.

[30] Cross, E. D.; Allan, L. E. N.; Decken, A.; Shaver, M. P. *J. Polym. Sci. Part A: Polym. Chem.* **2012**, *51*, 1137–1146.

[31] Du, H.; Pang, X.; Yu, H.; Zhuang, X.; Chen, X.; Cui, D.; Wang, X.; Jing, X. *Macromolecules* **2007**, *40*, 1904–1913.

[32] Atwood, D. A.; Harvey, M. J. *Chem. Rev.* **2001**, *101*, 37–52.

[33] Addison, A. W.; Rao, T. N.; Reedijk, J.; Rijn, J. V.; Verschoor, G. C. *J. Chem. Soc., Dalton Trans.* **1984**, 1349–1356.

[34] Hansch, C.; Leo, A.; Taft, R. W. *Chem. Rev.* **1991**, *91*, 165–195.

[35] Hoops, S.; Sahle, S.; Gauges, R.; Lee, C.; Pahle, J.; Simus, N.; Singhal, M.; Xu, L.; Mendes, P.; Kummer, U. *Bioinformatics* **2006**, *22*, 3067–3074.

[36] Blackmond, D. *Angew. Chem., Int. Ed.* **2005**, *44*, 4302–4320.

[37] Talarico, G.; Barone, V.; Joubert, L.; Adamo, C. *Int. J. Quantum Chem.* **2003**, *91*, 474–482.

[38] Marenich, A. V.; Jerome, S. V.; Cramer, C. J.; Truhlar, D. G. *J. Chem. Theor. Comput.* **2012**, *8*, 527–541.

[39] Jegier, J. A.; Muñoz Hernàndez, M.-A.; Atwood, D. A. *J. Chem. Soc., Dalton Trans.* **1999**, 2583–2588.

[40] Muñoz Hernàndez, M.-A.; McKee, M. L.; Keizer, T. S.; Yearwood, B. C.; Atwood, D. A. *J. Chem. Soc., Dalton Trans.* **2002**, 410–414.

[41] Getzler, Y. D.; Mahadevan, E. B., V. andLobkovsky; Coates, G. W. *Pure Appl. Chem.* **2004**, *76*, 557–564.

[42] Marshall, E. L.; Gibson, V. C.; Rzepa, H. S. *J. Am. Chem. Soc.* **2005**, *126*, 6048–6051.

[43] Dove, A. P.; Gibson, V. C.; Marshall, E. L.; Rzepa, H. S.; White, A. J. P.; Williams, D. J. *J. Am. Chem. Soc.* **2006**, *128*, 9834–9843.

[44] Kurahashi, T.; Fujii, H. *J. Am. Chem. Soc.* **2011**, *133*, 8307–8316.

[45] Cavazzini, M.; Manfredi, A.; Montanari, F.; Quici, S.; Pozzi, G. *Eur. J. Org. Chem.* **2001**, 4639–4649.

[46] Braun, M.; Fleischer, R.; Mai, B.; Schneider, M.-A.; Lachenicht, S. *Adv. Synth. Catal.* **2004**, *346*, 474–482.

[47] Zhao, Y.; Truhlar, D. G. *J. Chem. Phys.* **2006**, *125*, 194101/1–194101/18.

[48] Hehre, W. J.; Radom, L.; Schleyer, P. v. R.; Pople, J. A. *Ab Initio Molecular Orbital Theory*; Wiley: New York, 1986.

[49] Frisch, M. J. Gaussian 09, Revision C.01. 2010; See Supporting Information for full reference.

[50] Cramer, C. J. *Essentials of Computational Chemistry: Theories and MOdels*, 2nd ed.; John Wiley & Sons: Chichester, U.K., 2004.

[51] Ribeiro, R. F.; Marenich, A. V.; Cramer, C. J.; Truhlar, D. G. *J. Phys. Chem. B* **2011**, *115*, 14556–14562.

[52] Zhao, Y.; Truhlar, D. G. *Theor. Chem. Acc.* **2008**, *120*, 215–241.

2.2 Mechanistic Studies of ε-Caprolactone Polymerization by (salen)AlOR Complexes and a Predictive Model for Cyclic Ester Polymerizations

2.2.1 Introduction

Through the controlled ring-opening polymerization (ROP) of cyclic esters, a variety of useful and often renewable polymers may be synthesized.[1–9] Among the catalysts found to be effective in such polymerization reactions, metal alkoxides are ubiquitous and in many cases operate at high rates with excellent control of polymer molecular weight and stereochemistry.[3–9] Further improvements in catalytic behavior by metal alkoxide catalysts are likely if the mechanism(s) of ROP is (are) understood and the roles of supporting ligand structural variation on ROP rates and selectivities are unraveled. Toward that end, numerous mechanistic studies have been reported, leading to the hypothesis of the often used and generic "coordination-insertion" pathway (Figure 2.13), wherein binding of the ester to the metal (coordination) is followed by nucleophilic attack and ring opening (insertion).[2–15] However, the involvement of these two sequential independent steps has been difficult to confirm and evaluation of the influences of ligand variation on them has been impeded because comparisons are typically made on the basis of measured pseudo-first-order rate constants (k_{app}) that are composites of equilibrium and/or rate constants for the attendant elementary reaction steps.

Fig. 2.13 Generalized Coordination–Insertion Mechanism

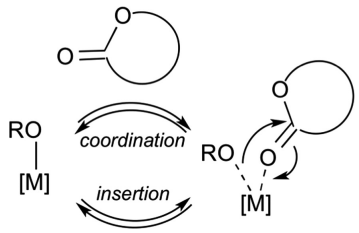

Nonetheless, intriguing effects of changes in ligand structure on ROP k_{app} values have been seen. A notable example is a study of *rac*-lactide (LA) polymerization using aluminum alkoxide catalysts derived from treatment of (salen)AlMe complexes with benzyl alcohol (Figure 2.14, top);[16] such aluminum alkoxide catalysts are known to be mononuclear, single-site species that operate at rates convenient for measurement by routine nuclear magnetic resonance (NMR) methods. Rates of LA ROP increased when $R_1 = R_2 =$ Cl versus H or *t*-Bu (with identical linkers X), consistent with the enhanced electrophilicity of the metal center underlying higher k_{app} values. The rates also increased as the linker was changed from two to three carbons (X = -$CH_2C(Me)_2$- vs -$CH_2C(Me)_2CH_2$-), but on the basis of the data available the only conclusion drawn was that "the enhanced performance of the C_3 linker is more a function of the flexibility of the linking unit, which may allow the complex to better access the key transition states involved in the ROP process".[16]

Fig. 2.14 General Structures of (salen)AlMe complexes

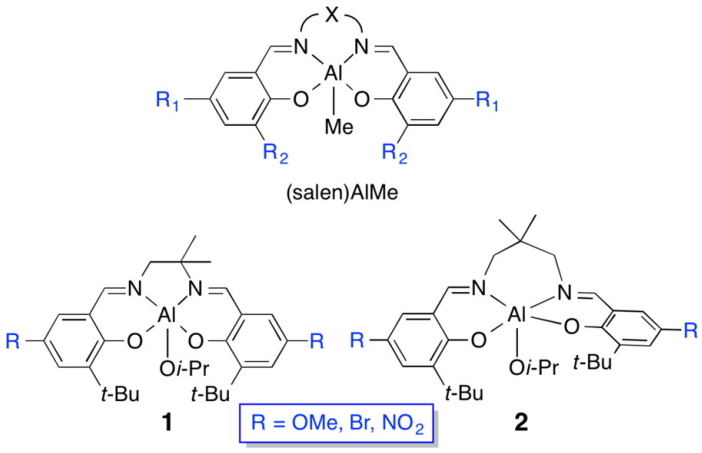

Structures of (salen)AlMe complexes studies as LA polymerization precursors (top)[16] and catalysts **1** and **2** used in mechanistic studies of CL polymerization (bottom)

We have sought more detailed mechanistic information for such cyclic ester polymerizations by mononuclear aluminum alkoxide complexes through dissection of composite k_{app} values into kinetic/thermodynamic constants associated with elementary reaction steps.[17,18] Through such studies, we aim to better understand the fundamental basis for ROP rate differences caused by catalyst structure variation in compounds that are single-site catalysts, with the ultimate goal of applying this knowledge to the design of more effective catalysts. In previous work,[18] we examined the kinetics of CL polymerization by mononuclear aluminum alkoxide complexes **1** (Figure 2.14) using high monomer concentrations ($[CL]_0 \geq 2.0\,M$). Under these conditions, saturation behavior was observed, and the data could be fit to the rate law Eq. 2.1 (PCL = polycaprolactone) to provide values of the equilibrium constant for monomer binding, K_{eq}, and the rate constant for monomer enchainment, k_2, as a function of temperature and remote substituent R. While K_{eq} varied little as a function of the electron-withdrawing properties of R (Hammett $\rho = +0.16(8)$), the k_2 dependence was significantly larger ($\rho = +1.4(1)$), supporting the hypothesis that differences in k_2 underly

observed overall rate differences and that k_2 is enhanced by increased electrophilicity of the metal center. Density functional theory (DFT) revealed transition-state (TS) structures featuring bond formation between the alkoxide and the incoming carbonyl of CL, showing that greater electron withdrawal by the substituent on the salen ligand results in greater bonding between the nucleophilic alkoxide and the lactone carbonyl carbon in the TS to give enhanced polymerization rates, and indicated that K_{eq} was not appropriately assigned to formation of a CL adduct along the reaction pathway; instead, K_{eq} is associated with "non-productive" binding that inhibits the ROP rate at high substrate concentrations.

$$-\frac{\mathrm{d[CL]}}{\mathrm{d}t} = \frac{\mathrm{d[PCL]}}{\mathrm{d}t} = \frac{k_2[\mathbf{2}][\mathrm{CL}]}{1/K_{\mathrm{eq}} + [\mathrm{CL}]} \qquad \text{(2.1 revisited)}$$

To dissect the intriguing effect of linker length described in the previous studies,[16] we have now applied our saturation kinetics approach to ROP by **2**, comprising the same substituents as **1** but with a longer ligand linker. As described below, we observed saturation kinetics for CL polymerization by **2** that were fit to Eq. 2.1 to yield K_{eq} and k_2 values as a function of temperature. Comparison of these values to those reported previously for **1**[1] in concert with evaluation of reactant and transition-state structures via DFT, provided additional detailed insight into how linker length affects ROP, with intriguing implications for future ROP catalyst design.

2.2.2 Results

Synthesis and Characterization of Ligands and Complexes The proligands H_2L^R (R = OMe, Br, NO_2) and their complexes **2** were prepared according to the same procedures described previously for **1**,[18] except using 2,2-dimethyl-1,3-propanediamine in the condensations with the respective salicylaldehydes. The proligands were isolated as bright yellow

crystalline solids in good yields (70-91%) and then heated with Al(O-*i*-Pr)$_3$ in toluene to afford the compounds **2**, which were isolated as analytically pure bright yellow, yellow, and light brown solids (R_1 = OMe, Br, NO_2, respectively), also in good yields (72-90%). The proligands and complexes were characterized by ^{1}H, ^{1}H^{13}C, and ^{27}Al NMR spectroscopy, CHN analysis, and, for **2** (R = Br), X-ray crystallography. The X-ray structure (Figure 2.15) confirms the

Fig. 2.15 Representation of the X-ray Crystal Structure of **2** (R = Br)

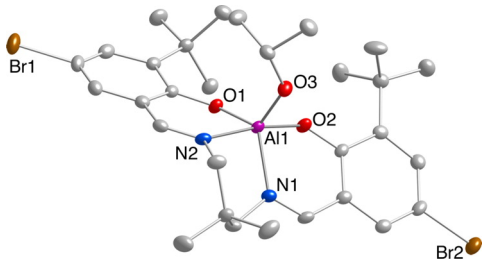

All non-hydrogen atoms as 50% thermal ellipsoids. Selected interatomic distances (Å) and angles (deg): Al1–O1, 1.7803(17); Al1–O2, 1.8225(18); Al1–O3, 1.7345(19); Al1–N1, 2.054(2); Al1–N2, 1.994(2); O3–Al1–O2, 95.76(9); O3–Al1–O1, 120.96(9); O2–Al1–O1, 91.22(8); O3–Al1–N1, 92.35(9); O2–Al1–N1, 171.10(9); O1–Al1–N1, 87.74(8); O3–Al1–N2, 118.71(9); O2–Al1–N2, 88.90(8); O1–Al1–N2, 119.98(9); N1–Al1–N2, 83.98(8).

anticipated five-coordinate formulation with a τ value of 0.84,[19] close to idealized trigonal bipyramidal (τ = 1) and similar to that of related complexes of salen ligands also featuring the 2,2-dimethylpropyl linker.[16,20–23] The τ value differs from that previously determined for **1** (R = OMe; τ = 0.52)[18] and other closely related congeners with a two-carbon linker (τ = 0.48–0.56).[16,20,21] Density functional theory optimization of **2** (R = H; see Density Functional Calculations for theoretical details) provided a τ value of 0.85, which is in excellent agreement with that determined from crystallography, suggesting that crystal packing forces do not significantly influence the intrinsic coordination geometry at the aluminum center. The ^{1}H NMR spectra for the complexes (Figures S1-S6 in the Supporting Information) are consistent with monomeric structures and contain a single resonance for

the *tert*-butyl groups, indicating that the two different chemical environments of the aryl groups in the experimentally determined X-ray structure for **2** (R = Br) and calculated gas-phase structures for **2** (R = H) are averaged in solution. Such fluxionality was reported for other complexes of related salen ligands with the 2,2-dimethylpropyl linker.[16,20–23] The NMR spectra of the complexes **2** with different R groups are generally similar, except for differences in the aryl region (imine hydrogens and two aromatic hydrogens adjacent to R). The ^{27}Al NMR spectra contain a single resonance at 35, 34 and 33 ppm for the complexes with R = OMe, Br, NO_2, respectively.

Kinetics of CL Polymerizations NMR-scale polymerization reactions for each catalyst were run in triplicate at four different temperatures ranging from 273 to 313 K. The reactions were performed in toluene-d_8 with a fixed initial concentration of monomer ([CL] = 2.0 M), catalyst ([cat] = 5.5 to 7.0 mM), and internal standard ([1,4-bis(trimethylsilyl)benzene] = 4.0 mM), with growth of polymer (PCL) and decay of monomer (CL) monitored throughout the reaction by ^{1}H NMR spectroscopy. Most polymerizations achieved 99% conversion, except for those catalyzed by **2** (R = NO_2) at 273 K, for which the loss of NMR shims only allowed for analysis up to only about 84% conversion. Similarly to previous work,[17,18] the concentrations of CL and PCL (determined by integrations vs the standard) were plotted versus time and fit to Eq. 2.1 using the global kinetics fitting program COPASI (Figures S7-S11 in the Supporting Information). A reaction progress kinetic analysis (RPKA)[24] protocol was used to analyze one polymerization run (R = Br, 273 K) and further supported the appropriateness of Eq. 2.1 (Figure S12 and Table S2 in the Supporting Information), with fits to alternative first- and second-order rate laws being notably inferior (Figure S13 in the Supporting Information). Average values from the triplicate runs for the kinetic parameters K_{eq} and k_2 calculated from the COPASI fits to Eq. 2.1 are compiled in Table 2.8; the complete list of parameters from both COPASI analysis and RPKA are provided in

Table S1 in the Supporting Information.

Table 2.8 Average Values of Kinetic Parameters K_{eq} and k_2 for Complexes **2**

Entry	Temp (K)	R	K_{eq} COPASI (M^{-1})	K_{eq} NMR (M^{-1})	k_2 ($s^{-}1$)
1	313	OMe	3.4(7)	0.65(9)	0.32(2)
2	298	OMe	3.8(7)	0.64(5)	0.147(5)
3	293	OMe	3.3(4)	0.69(4)	0.105(3)
4	283	OMe	4.0(5)	0.88(3)	0.048(3)
5	298	Br	1.4(3)	0.6(1)	0.67(6)
6	293	Br	1.3(2)	1.2(4)	0.53(4)
7	283	Br	1.5(2)	0.9(2)	0.27(2)
8	273	Br	1.7(2)	0.65(8)	0.106(6)
9	293	NO_2	0.8(4)	1.9(5)	1.9(7)
10	288	NO_2	0.5(2)	1.6(3)	1.9(6)
11	278	NO_2	0.9(3)	1.9(2)	0.6(2)
12	273	NO_2	0.7(5)	1.7(5)	0.5(2)

The presence of a substrate binding equilibrium characterized by K_{eq} was further confirmed by two independent sets of experiments. First, we analyzed the chemical shifts of peaks associated with the catalyst during the polymerization reaction. Changes in the chemical shifts of the catalyst peaks as a function of [CL] were observed, and we analyzed them as described previously,[17,18] working under the assumption that these changes arise from rapid equilibration between complexes with and without bound monomer. Typical ^{1}H NMR spectra and plots of chemical shift vs [CL] are presented in Figures S14-S17 in the Supporting Information, and calculated average K_{eq} values are given in Table 2.8 (a full list is given in Table S3 in the Supporting Information). Although the K_{eq} values independently determined from the catalyst NMR peak analysis and those obtained from the kinetic fits (COPASI) of the CL decay and PCL generation profiles to Eq. 2.1 are not identical, we consider them to be sufficiently similar to be consistent with the hypothesized substrate binding equilibration, especially if one considers the narrow span of derived ΔG° values (see

below).

In a second set of experiments, complexes **2** were mixed at 293 K with varying concentrations of γ-butyrolactone (BL), a cyclic ester that is relatively unreactive toward ring-opening polymerization.[25–28] The chemical shifts of the ligand peaks in the aromatic region were observed to change as a function of BL, consistent with a binding equilibrium. Fitting of the data accordingly yielded K_{eq} values of 0.6(1), 0.5(2) and 0.9(2) for R = OMe, Br, NO_2, respectively (Figures S18 and S19 in the Supporting Information). The relatively good agreement among the K_{eq} values determined from fitting of the kinetic profiles and analysis of the catalyst NMR peaks during CL polymerization and in the presence of BL provides strong experimental evidence for equilibrium binding of lactones to the catalysts **2** (Table S4 in the Supporting Information).

Evaluation of the variation of the experimentally determined kinetic and thermodynamic parameters as a function of substituent R and temperature provided important insights. A plot of ln K_{eq} versus 1/T including values from both COPASI (circles) and NMR analysis (squares) shows clustering of ln K_{eq} values within a relatively narrow range (-0.5 to $+1.5$) and with minimal temperature dependences indicative of relatively small ΔG° values of < 2 kcal/mol for monomer binding (Figure 2.16).

Fig. 2.16 Plot of ln K_{eq} versus 1/T for **2**

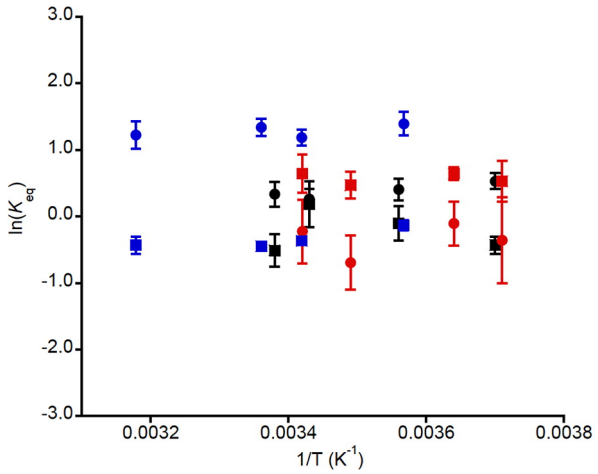

R = Br, black; R = OMe, blue; R = NO_2, red, using K_{eq} values determined via kinetic fits (COPASI, circles) and via fits of catalyst peak chemical shifts in NMR spectra (NMR, squares)

The K_{eq} values determined by COPASI as a function of R are ordered OMe > Br > NO_2, but the differences are small and this ordering is not followed using the values determined by the NMR method. Thus, as reported previously for **1**[18] we conclude that the thermodynamics for binding of CL to **2** are relatively insensitive to substituent R, consistent with differences in CL binding not being an important basis for the differences in the observed polymerization rates.

The temperature dependences of the rate constants k_2 for the polymerizations of CL by **2** (this work, circles) and **1** (squares)[18] are shown in Figure 2.17 and activation parameters determined from linear fits to the Eyring equation are given in Table 2.9 It is readily apparent from the Eyring plots in Figure 2.17 and the derived $\Delta G^{\ddagger}_{298}$ values that the polymerization rate constants are greater for **2** than for **1**.

Fig. 2.17 Eyring Plots for **1** and **2**

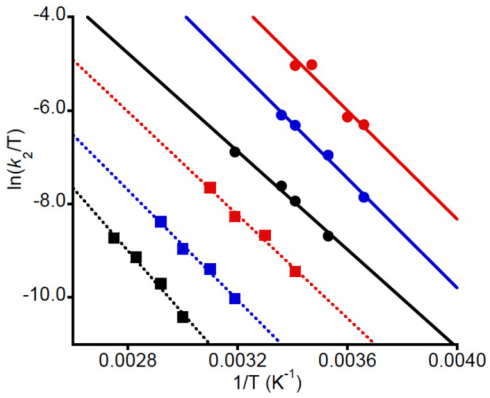

Eyring plots of ln k_2/T versus $1/T$ for **1** (squares, dashed lines) and **2** (circles, solid lines) for R= OMe (black), Br (blue), and NO_2 (red).

Table 2.9 Activation Parameters (k_2) for the Polymerization of CL

catalyst	R	$\Delta H^{\ddagger}$ (kcal/mol)	$\Delta S^{\ddagger}$ (cal/(mol·K))	$\Delta G^{\ddagger}$ (kcal/mol, 298 K)
2[a]	OMe	9.1 ± 0.3	−32 ± 1	18.6 ± 0.4
2[a]	Br	10.4 ± 0.4	−24 ± 1	17.6 ± 0.5
2[a]	NO_2	10.0 ± 0.9	−23 ± 3	17 ± 1
1[b]	OMe	13.5 ± 0.5	−27 ± 2	21.5 ± 0.8
1[b]	Br	11.5 ± 0.3	−30 ± 2	20.4 ± 0.7
1[b]	NO_2	10.8 ± 0.4	−27 ± 2	18.8 ± 0.8

[a] Determined from the linear fits in Figure 2.17. [b] Reference 18.

From the activation parameters, we calculate that the fastest catalyst **2** (R = NO_2) and the slowest catalyst **1** (R = OMe) have k_2 values that differ by factors of (1–5) 10^3 (350–273 K). Hammett plots of log k_2 versus σ_p for **2** are linear at all temperatures with similar positive slopes (Figure 2.18), yielding an average ρ value of +1.2(1) that is similar to that reported previously for **1** (+1.4(1)).[18] Thus, the sensitivities of the rate constants to the electronic influences of the ligand substituents R are similar for the two catalyst systems.

Fig. 2.18 Hammet Plots for **2**

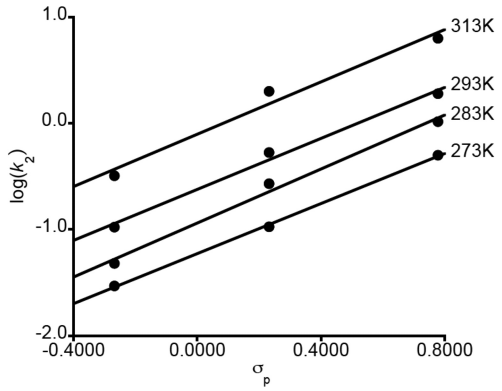

Hammet plots of log(k_2 versus σ_p for the polymerization of CL by **2** at the indicated temperatures.

Theoretical Modeling To gain additional insight into the observed catalytic activities, and in particular to better understand the rate accelerations observed relative to the first-generation catalyst **1**, we undertook density functional characterization of reaction pathways associated with catalyst **2** (see the Experimental Section for full computational details). For computational simplicity, we modeled the alkoxide in the precatalyst as MeO instead of *i*PrO, and to differentiate this we refer to the MeO-substituted precatalyst structures as **1'** and **2'** below.

Conformational Flexibility of Catalyst In comparison to **1'** with its two-carbon backbone linker, a number of alternative chair and twist-boat conformations of the three-carbon backbone are available to the ligand in **2'**. In particular, for the precatalyst carrying no para substituents on the aromatic rings, we identified four different conformations (three twist-boats and one chair), spanning a range in electronic energy of 2.2 kcal/mol. Both the lowest and highest energy conformations were found to be twist boats (the lowest is shown in Figure 2.19), with the chair conformation being intermediate in energy.

Fig. 2.19 DFT Predicted Catalyst and Transition State Structures for **1'** and **2'**

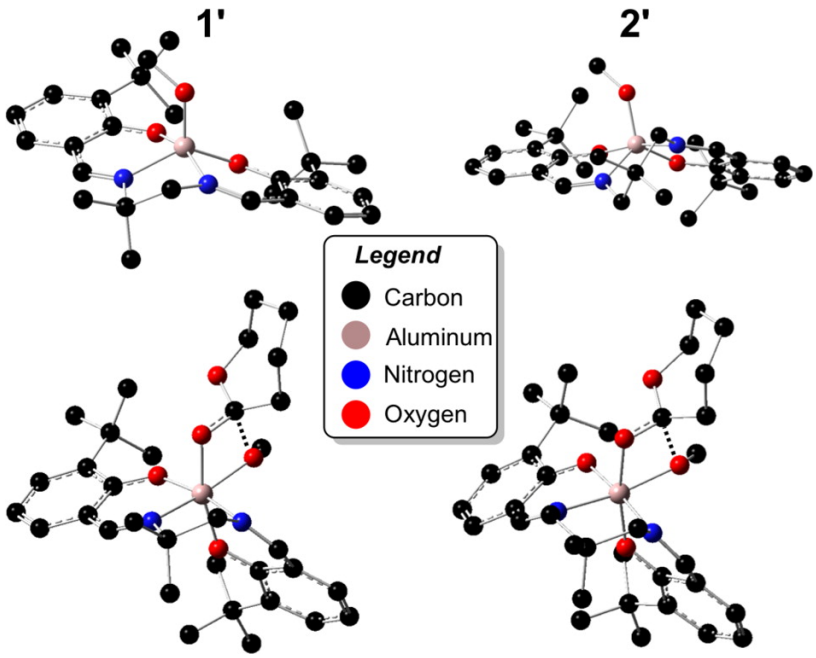

DFT Predicted lowest-energy structures for *p*-H-substituted **1'** and **2'** (above) and for their corresponding transition state structures for ring opening of CL (below) H atoms are omitted for clarity.

A Boltzmann average over all four conformers leads to a reduction in the free energy of the population of free catalyst structures of only 0.1 kcal/mol: i.e., the global minimum sits reasonably far below the other conformers in energy. We applied the same 0.1 kcal/mol correction to the energies of the global minimum twist boats in the para-substituted cases, assuming the influence of para substitution on the conformational energetics to be minimal.

Catalysis To characterize the mechanism of ROP with the catalyst **2'**, we carried out an exhaustive search over all of the pathways associated with the various possible catalyst/CL stereochemical orientations analogous to a prior study involving catalyst **1'**.[18] We observed again that one particular orientation, which was referred to as "pathway 6" in our prior

work,[18] led to CL ring opening through a TS structure having the lowest activation free energy of all those surveyed (Figure 2.19). Indeed, for the model system lacking para substituents, $\Delta G^{\ddagger}$ along pathway 6 was predicted to be at least 4 kcal/mol lower than any other pathway investigated, suggesting that Boltzmann averaging over alternative stereochemistries is not required for the modeling of the transition state. The TS structures in **1'** and **2'** are overall quite similar: in each case, there is roughly octahedral coordination about Al with an O–Al–O angle involving the alkoxide and carbonyl oxygen atoms of about 75° and with both Al–O bond lengths being 1.92 ± 0.01 Å. Full details of all bond lengths and angles are provided in Figure S20 in the Supporting Information, and additional analysis of the similarity of TS structure geometries across a wider range of Al-based catalysts is provided below in the Discussion (see page 58).

Rate Acceleration in Catalyst 2' Predicted free energies of activation for the reaction of catalyst **2'** with CL are provided in Table 2.10 for the cases of *p*-MeO, *p*-Br, and *p*-NO_2 substitution at 298 K.

Table 2.10 Predicted 298 K Activation Free Energies (kcal/mol) for Reaction of **1'** and **2'** with CL

para substituent	**1'**	**2'**
MeO	12.4	9.7
Br	11.1	8.2
NO_2	9.6	5.9

Also included in Table 2.10 are the analogous predictions previously reported for catalyst **1'**. Experimentally, a rate acceleration of about 3 orders of magnitude is observed on going from **1** to **2** with identical para substituents, which corresponds to a lowering of the activation free energy by about 4 kcal/mol at 298 K. As can be seen in Table 2.10, we predict reductions in activation free energies of 2.7, 2.9 and 3.7 kcal/mol for the *p*-MeO-, *p*-Br-,

and p-NO_2-substituted cases of **2'**, respectively. These reductions (in what is effectively $K_{eq}{}^{*}k_2$, since we compute activation free energies relative to infinitely separated reactants) are in generally good agreement with experimental observations (cf. Table 2.9, noting that variations in k_2 have a larger influence on relative rates than K_{eq}; cf. Table 2.8), although the acceleration predicted for the p-NO_2-substituted system is somewhat larger. Focusing only on para substitution effects in **2** itself, experiment shows an acceleration relative to R = MeO of −1.1 and −1.5 kcal/mol for R = Br and R = NO_2, respectively. Theory predicts values of −1.5 and −3.8 kcal/mol for **2'**, again in reasonably good agreement with experiment, albeit with some overestimation of the rate acceleration afforded for the p-NO_2 case.

Saturation Kinetics Experimental measurements indicate that there is a modest equilibrium constant for the complexation with CL of all three para-substituted derivatives of **2** examined here. This is similar to the situation previously described for **1**,[18] where DFT identified many local minimum structures corresponding to van der Waals complexes between CL and **1'**. In that case, the lowest energy such structure involved CL binding trans to the methoxide ligand, generating a structure that is necessarily incapable of ring opening; thus, the saturation kinetics observed were interpreted as substrate inhibition. In the case of **2'**, on the other hand, no such trans complexes with CL proved to be especially favorable—while van der Waals structures having CL on the side of **2** opposite MeO could be located, they were no lower in energy than alternative structures with CL on the same face as MeO, likely owing to steric constraints diminishing favorable interactions between Al and the carbonyl oxygen of CL (the shortest distance found between these two atoms for a trans complex was 2.26 Å; see Figure 2.20). However, saturation kinetics is predicted for reactions having a pre-equilibrium irrespective of whether that equilibrium leads to unreactive or reactive structures, and in this respect the kinetics of **2'** in comparison to those of **1'** are rationalized as deriving from a still-sizable population of prereactive complexes.

Fig. 2.20 Representative M06-L Same-Face and Opposite-Face van der Waals Complexes of CL with **1'** and **2'**

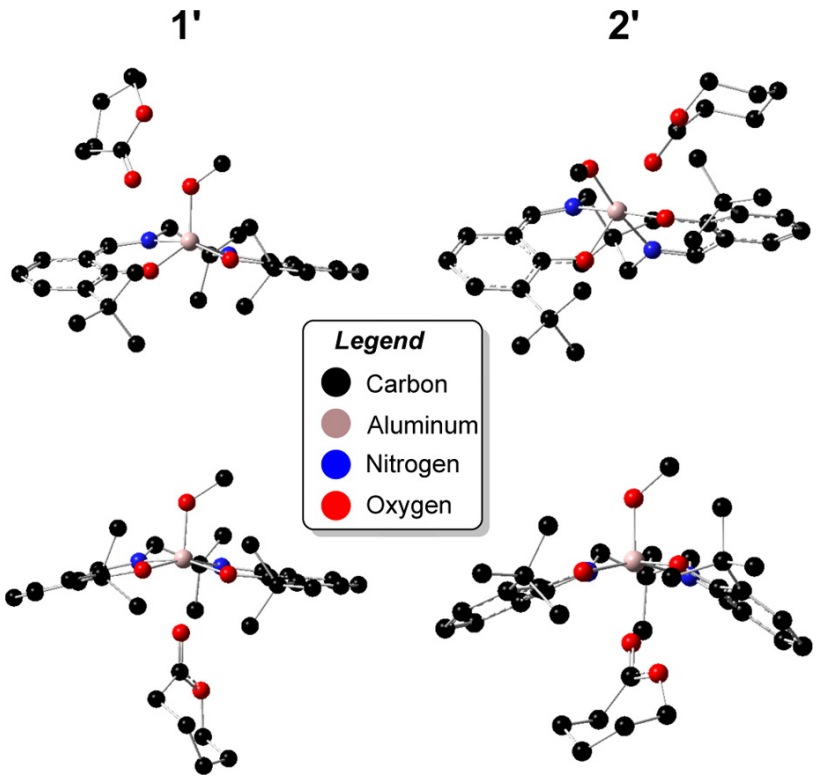

In the case of **1'**, the trans complex is lower in free energy than the same-face structure by 8.4 kcal/mol. In the case of **2'**, the trans complex is higher in free energy by 7.0 kcal/mol.

2.2.3 Discussion

In delving into the detailed effects of the change in ligand linker from two carbons to three on the rate of CL polymerization by **1** and **2**, respectively, we used a combination of experimental and theoretical approaches to compare the structures of the reactants, their saturation kinetics behavior as a function of para substituent and temperature, and the nature of relevant ring-opening transition states. X-ray crystallography and theory confirmed that the longer linker in **2** results in a coordination geometry closer to trigonal

bipyramidal ($\tau = 0.84$) in comparison to **1** ($\tau = 0.52$). This structural effect had been noted previously but discounted as a rationale for different LA polymerization rates because rate accelerations did not occur with (salen)AlMe precatalysts with similar τ values but with rigid rather than flexible linkers.[16] As seen for **1**, we observed saturation behavior in the kinetics of CL polymerization by **2**, and the combined evidence from kinetic fits and NMR data for **2** in the presence of BL, which does not polymerize under the conditions explored, supports assignment of K_{eq} to equilibrium monomer binding. For **1**, theory suggests that the lowest energy complex-binding monomer is unable to proceed to polymerization (owing to trans binding) and is thus inhibitory. For **2**, theory predicts that trans binding is not competitive with productive binding, and K_{eq} instead is a measure of alternative prereactive bound complexes. Nonetheless, the relevant kinetic behavior is the same in these two situations: i.e., saturation kinetics is predicted and observed. Importantly, we conclude that differences in CL polymerization rates between **1** and **2** and among systems with different para substituents R do not arise from differences in K_{eq} because these values do not vary significantly as a function of linker length (**1** vs **2**), R (OMe, Br, or NO_2), or temperature. Instead, the overall rate differences arise from variations in k_2. While the sensitivity of k_2 to the electron-withdrawing ability of substituent R is similar for systems **1** and **2** (Hammett ρ values of +1.4(1) and +1.2(1), respectively), and this supports similar mechanisms for CL polymerization by these two systems, at parity of R the rates of CL polymerization by **2** are significantly faster.

To rationalize the rate acceleration observed with **2** in comparison to **1**, we focused more closely on the geometric details associated with the ring-opening TS structures in each instance.[iii] As noted above and quantified in Figure S20 in the Supporting Information, for the two different TS structures the geometry about the catalytic Al center is predicted

[iii] We did examine whether the two different ligands had differing electronic influences on the natures of the precatalyst or TS structures. However, CM5 partial atomic charges (see ref 29) computed for corresponding species showed essentially no variation as a function of ligand, leading us to focus more closely on steric/geometric influences.

to be quite similar: the mean unsigned deviation over all Al–X bond lengths is 0.01 Å and the mean unsigned deviation over all (cis) X–Al–Y angles is 3.0°. This observation suggests that each catalyst is able to achieve a common geometry that is optimal for reducing the free energy of activation of ring opening. It also raises the question, then, of what is required in terms of distortion energy relative to the resting precatalyst structure to arrive at this optimal geometry. Also shown in Figure S20 are corresponding metrics for the resting precatalysts **1'** and **2'**, and it is clear that there are more substantial geometric differences between these alkoxide complexes than there are between the corresponding TS structures. The differences are primarily associated with the degree of square-pyramidal vs trigonal-bipyramidal character imposed by the different ligands and are well captured by the different τ values reported above (experimental and calculated).

To address the question of the influence of required distortion from precatalyst to TS structure in more quantitative detail, for both **1'** and **2'** we removed the reacting partners and the MeO units from the optimized TS structures, and we carried out single-point calculations on the resulting cationic conformers of the catalyst frameworks to determine their differences in energy relative to the precatalyst from which the MeO unit had been removed. This calculation thereby provides an approximation to the distortion energy of the aluminum-ligand framework that is associated with adoption of a geometry well suited to stabilize the optimal TS structure. The framework of **1** requires 18.3 kcal/mol to distort from the precatalyst structure to the TS structure, while the framework of **2** has a corresponding distortion energy of only 6.8 kcal/mol. Clearly, then, the "resting" framework of **2** is much closer to the optimal catalytic geometry than is that of **1**. This computed difference is considerably larger than the experimentally observed rate acceleration, as might be expected insofar as differential alkoxide interactions with the catalyst resting geometries would be expected to act in some way to reduce differential strain. Nevertheless, the striking difference that is computed suggests that enhanced catalytic activity can be engineered through the

design of catalysts whose precomplexed structures are already geometrically similar to the octahedral TS structures determined from DFT to have the lowest activation free energies for ring-opening polymerization.

To assess further the relative utility of this framework-strain analysis for the prediction of catalyst activity, we examined another six related ROP catalysts reported previously (structures in Figure 2.21).[16] In each instance, we computed precatalyst and TS structures analogous to those for **1'** and **2'**. In all eight TS structures, there was a remarkable uniformity in the 12 unique cis valence bond angles about Al. For example, for the O–Al–O valence angle between the alkoxide and caprolactone carbonyl oxygen atoms, the average and standard deviation were found to be $74.8 \pm 0.7°$ over all eight structures. The largest angular standard deviation, 4.7°, was associated with the N–Al–N valence angle, which is unsurprising given the variation in bridge lengths in the various catalysts; for all remaining angles, the standard deviations ranged from 0.6 to 2.3°.

Fig. 2.21 Relationship Beteen ln k_{app} and Computed Activation Free Energies and Framework Distortion Energies

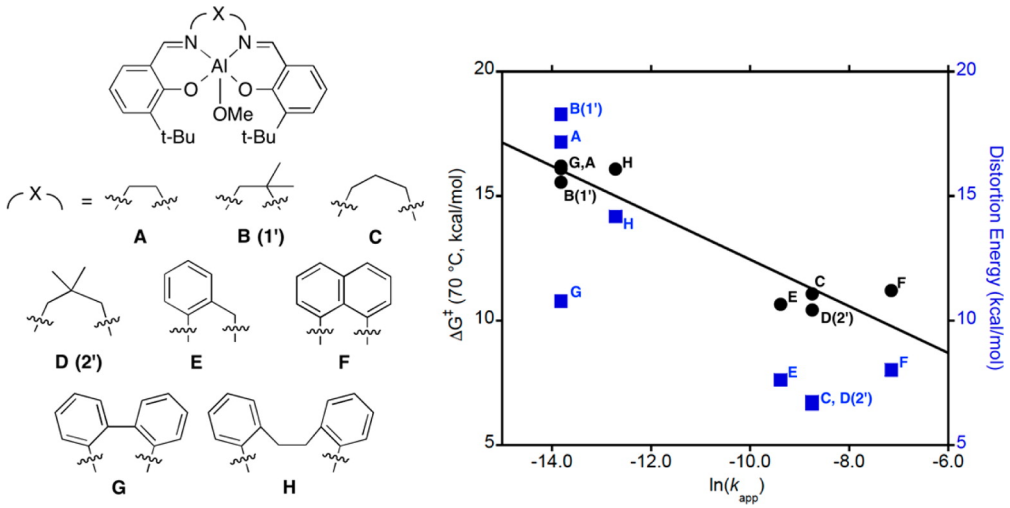

Relationship between ln k_{app} for a series of ROP catalysts described by Gibson et al.[16] (but lacking the *t*-Bu groups para to the phenolate donors) and computed activation free energies (black circles) and framework distortion energies (blue squares) for corresponding reactant and TS structures. The best-fit line to the activation free energies has the Pearson correlation coefficient R = 0.947. The best-fit line to the framework distortion energies (not shown) has R = 0.852.

This similarity in TS structures prompted us to explore further the utility of our distortion energy hypothesis. Thus, we removed the same alkoxide and CL components and computed distortion energies for the six additional compounds[16] analogous to those already described for **1'** and **2'** (Figure 2.21). These distortion energies, as well as the computed activation free energies, are plotted vs the natural logarithm of the previously reported[16] lactide ROP rate constants (for catalysts that contain *t*-Bu groups para to the phenolate donor) determined under equivalent conditions in Figure 2.21 (together with the calculated data for **1'** and **2'** already described above).

There is a good correlation between the computed activation free energies and the observed ln k_{app} values, providing further validation of the modeling protocol. Interestingly,

the correlation of the rate constant data with the framework distortion energies is also fairly good. Indeed, *if* the data point for catalyst **G** is removed, the Pearson correlation coefficient for the latter correlation is predicted to be identical with that for the activation free energies (R = 0.947). For this outlier, a significantly lower distortion energy is predicted than for catalysts **A** and **B**, even though all three are found experimentally to catalyze ROP at essentially identical rates. This suggests that there is an interaction in the actual TS structure for **G** that destabilizes the structure beyond distortion of the framework. Indeed, if one examines a space-filling model of the TS structure for polymerization of CL by **G** (Figure 2.22) it is apparent that one phenyl ring associated with the backbone bridge of the ligand is thrust into the space that the reacting alkoxide and CL moieties (not present in the framework distortion calculation) occupy and that there is a steric clash between a CL hydrogen and that ring. Failure to account for such interactions is a drawback of the simple framework distortion energy metric.

Fig. 2.22 Optimized M06-L Structure for the Transition State for ROP of Caprolactone by Catalyst **G**

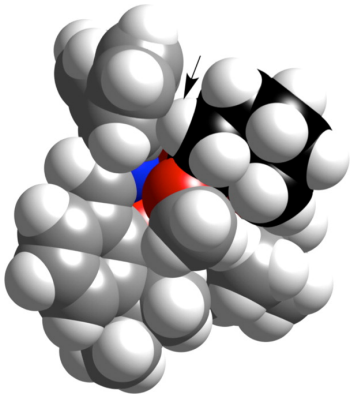

TS for ROP of CL by catalyst **G** drawn as a space-filling model (using CPK van der Waals radii). The CL ring carbons are highlighted in black, with the key destabilizing interaction of a CL hydrogen with the ligand aromatic ring indicated by an arrow.

Nevertheless, in addition to being of interest from a fundamental mechanistic standpoint,

the relationship between framework distortion energy and apparent rate constants we have discovered suggests a strategy for *in silico* catalyst design. To the extent that all of the various TS structures are geometrically similar to one another about aluminum, one could use the "average" set of TS bond angles described above for framework distortion calculations with arbitrary ligands without the added expense of actually finding a true TS structure. That is, one could compute a resting catalyst structure for a given ligand of choice, remove the alkoxide, and then compute the energy to distort the resulting structure to a pseudo-TS structure having the fixed "average" angles about Al, but all other degrees of freedom relaxed. While one might expect correlation with the proper free energies of activation to degrade with such limited relaxation, certainly ligands predicted to lead to very small framework distortion energies by this rapid computational screening technique would be higher priorities for initial experimental discovery efforts.

2.2.4 Conclusions

With the aim of understanding how linker length influences the ROP of lactones by single-site (salen)AlOR catalysts, we evaluated the kinetics for ROP of CL by **2** under conditions that enabled determination of K_{eq} and k_2 (Eq. 2.1) as a function of temperature and electron-withdrawing capabilities of remote substituents. Comparison of these and derived thermodynamic parameters for ROP by **2** to those previously reported for **1** which features a shorter linker, revealed similar dependences of K_{eq} and k_2 on the substituents (little variation of K_{eq}, similar Hammett parameters for k_2 of +1.4(1) and +1.2(1) for **1** and **2**, respectively). However, an overall significant increase in rate (k_2 values) was observed for **2** relative to **1**. Theoretical calculations accurately replicated the different reactant geometries for analogues **1'** and **2'** but showed that the ROP transition state structures were very similar, thus raising the possibility that the differing activation energies for the two catalysts

arise from differences in the energies required to distort the ligand framework to adopt the requisite TS geometries. Support for this notion was obtained by approximating the energy cost of distorting the ligand framework from its reactant geometry to that of the TS for **1'** and **2'** through single-point calculations. Extension of this method to a previously reported series of catalysts with varying ligand linkers yielded a good correlation between the distortion energy and the rate of ROP of LA. We suggest that this relatively simple method for evaluating the ligand framework distortion energy may have even broader utility for predicting the reactivity of metal alkoxide catalysts for cyclic ester ROP reactions and is therefore a potentially useful tool for future catalyst design.

2.2.5 Experimental Section

Materials and Methods. General Considerations Experiments were conducted under an inert atmosphere using a drybox or Schlenk line unless otherwise indicated. Reagents were purchased commercially and used without further purification unless otherwise stated. CL was purified by distillation from CaH_2 and stored under N_2. Deuterated solvents were dried over CaH_2 or sodium metal, distilled under vacuum, and stored under N_2. Protiated solvents were degassed and passed through a solvent purification system (Glass Contour, Laguna, CA) prior to use. ^{1}H and ^{13}C NMR spectra were recorded on a Bruker Avance III HD 500 MHz spectrometer equipped with a Prodigy TCI cryoprobe. Chemical shifts for ^{1}H and ^{13}C NMR spectra were referenced to residual protium in the deuterated solvent and deuterated solvent itself, respectively. ^{1}H NMR spectra for the kinetic runs were recorded on a Bruker Avance III 500 MHz spectrometer equipped with either a BBFO SmartProbe or a TBO triple-resonance PFG probe. ^{27}Al NMR spectra were recorded on a Bruker Avance III 500 MHz spectrometer equipped with a TBO triple-resonance PFG probe. Chemical shifts for ^{27}Al NMR spectra were externally referenced to aluminum tris(acetylacetonate) in

toluene-d_8. 2-Hydroxy-3-(*tert*-butyl)-5-methoxybenzaldehyde,[30] 2-hydroxy-3-(*tert*-butyl)-5-bromobenzaldehyde,[31] and 2-hydroxy-3-(*tert*-butyl)-5-nitro-benzaldehyde[32] were synthesized according to literature procedures. Elemental analyses were performed by Robertson Microlit Laboratory (Ledgewood, NJ).

Synthesis of Proligands H_2L^{OMe}, H_2L^{Br}, and $H_2L^{NO_2}$ In an oven-dried round-bottom flask equipped with a reflux condenser, the salicylaldehyde (H_2L^{OMe}, 1.583 g, 7.6 mmol; H_2L^{Br}, 1.311 g, 5.1 mmol; $H_2L^{NO_2}$, 1.473 g, 6.6 mmol) was dissolved in absolute ethanol to give an approximate 0.64 M concentration. To this mixture 2,2-dimethyl-1,3-propanediamine (H_2L^{OMe}, 0.388 g, 3.8 mmol; H_2L^{Br}, 0.266 g, 2.6 mmol; $H_2L^{NO_2}$, 0.337 g, 3.3 mmol) was added with stirring, and the solution was heated to reflux for 2 h. The reaction mixture was cooled to ambient temperature and left to sit overnight at −30 °C, yielding a precipitate. The crude precipitate was isolated by vacuum filtration and washed with hexanes (40 mL) before recrystallization from minimal dichloromethane (approximately 5 mL) layered with an equal volume of hexanes at −30 °C overnight. The purified product was isolated by vacuum filtration, dried overnight in a vacuum oven at ambient temperature, and stored under N_2 in a drybox as a bright yellow, crystalline solid. Yields: H_2L^{OMe}, 0.197 g, (70%); H_2L^{Br}, 1.355 g (91%); $H_2L^{NO_2}$, 1.246 g, (73%).

H_2L^{OMe}: ^{1}H NMR (500 MHz, toluene-d_8) δ 13.82 (s, 2H, O*H*), 7.78 (s, 2H, C*H*═N), 7.16 (d, J = 3.0 Hz, 2H, Ar*H*), 6.41 (d, J = 3.0 Hz, 2H, Ar*H*), 3.49 (s, 6H, ArOCH_3), 3.10 (s, 4H, NCH_2C(CH$_3$)$_2$CH_2N), 1.57 (s, 18H, Ar-*t-Bu*), 0.89 (s, 6H, NCH$_2$C(CH_3)$_2$CH$_2$N); ^{13}C NMR (125 MHz, toluene-d_8) δ 166.76, 155.52, 152.06, 139.20, 118.66, 118.56, 111.97, 68.30, 55.25, 35.98, 35.34, 29.57, 24.45. Anal. Calcd for $C_{29}H_{42}N_2O_4$: C, 72.17; H, 8.77; N, 5.80. Found: C, 72.09; H, 8.69; N, 5.73.

H_2L^{Br}: ^{1}H NMR (500 MHz, toluene-d_8) δ 14.21 (s, 2H, O*H*), 7.51 (d, J = 2.3

Hz, 2H, ArH), 7.47 (s, 2H, CH═N), 6.94 (d, J = 2.3 Hz, 2H, ArH), 2.98 (s, 4H, NCH_2C(CH_3)$_2$CH_2N), 1.43 (s, 18H, Ar-t-Bu), 0.79 (s, 6H, $NCH_2C(CH_3)_2CH_2N$); ^{13}C NMR (125 MHz, toluene-d_8) δ 165.80, 160.08, 140.47, 132.78, 132.23, 120.43, 110.44, 68.06, 35.90, 35.30, 29.25, 24.18. Anal. Calcd for $C_{27}H_{36}Br_2N_2O_2$: C, 55.87; H, 6.25; N, 4.83. Found: C, 55.90; H, 6.28; N, 4.83.

$H_2L^{NO_2}$: ^{1}H NMR (500 MHz, toluene-d_8) δ 15.27 (s, 2H, OH), 8.29 (d, J = 3.0 Hz, 2H, ArH), 7.79 (d, J = 3.0 Hz, 2H, ArH), 7.38 (s, 2H, CH═N), 2.93 (s, 4H, NCH_2C(CH_3)$_2$CH_2N), 1.42 (s, 18H, Ar-t-Bu), 0.74 (s, 6H, $NCH_2C(CH_3)_2CH_2N$); ^{13}C NMR (125 MHz, toluene-d_8) δ 167.16, 166.14, 139.61, 139.53, 126.40, 125.21, 117.34, 66.98, 35.82, 35.36, 28.98, 23.88. Anal. Calcd for $C_{27}H_{36}N_4O_6$: C, 63.26; H, 7.08; N, 10.93. Found: C, 62.64; H, 6.91; N, 10.79.

Synthesis of Complexes 2 In a glovebox, in an oven-dried 25 mL screw cap bomb flask equipped with a stirbar, equimolar amounts of proligand (H_2L^{OMe}, 0.241 g, 0.5 mmol; H_2L^{Br}, 0.290 g, 0.5 mmol; $H_2L^{NO_2}$, 0.256 g, 0.5 mmol) and aluminum tris(isopropoxide) (0.010 g, 0.5 mmol) were dissolved in toluene (3 mL). The sealed vessel was removed from the glovebox and heated to 90 °C, and the mixture was stirred at this temperature for 3 days. After being cooled to ambient temperature, the reaction mixture was returned to the glovebox and solvent was removed in vacuo. The crude solid was purified by trituration with pentane (5 mL) and then recrystallized from minimal toluene (approximately 4 mL) layered with an equal volume of pentane at −40 °C overnight. The purified product was isolated by vacuum filtration, dried overnight on a vacuum line, and stored under N in the glovebox at −40 °C as a bright yellow (R = OMe), yellow (R = Br), or light brown (R = NO_2) solid. Yields: R = OMe, 0.230 g (81%); R = Br, 0.184 g (72%); R = NO_2, 0.263 g, (90%).

2 (R = OMe): ^{1}H NMR (500 MHz, toluene-d_8) δ 7.48 (s, 2H, CH═N), 7.36 (d, J = 3.2

Hz, 2H, Ar*H*), 6.30 (d, $J = 3.2$ Hz, 2H, Ar*H*), 4.13 (septet, $J = 5.2$ Hz, 1H, OC*H*$(CH_3)_2$), 3.50 (s, 6H, ArOCH_3), 3.38 (d, $J = 12.1$ Hz, 2H, NCH*'H*$(CH_3)_2$CH*'H*N), 2.73 (d, $J = 12.1$ Hz, 2H, NC*H'*H$(CH_3)_2$C*H'*HN), 1.72 (s, 18H, Ar*t-Bu*), 1.17 (d, $J = 5.2$ Hz, 6H, OCH(C$H_3)_2$), 0.80 (s, 3H, $NCH_2(CH_3)$*'*(CH_3)CH_2N), 0.54 (s, 3H, NCH_2(CH_3)*'*$(CH_3)CH_2$N); ^{13}C NMR (125 MHz, toluene-d_8) δ 169.35, 161.44, 150.33, 143.24, 123.17, 118.37, 111.30, 68.09, 62.95, 55.25, 35.95, 35.65, 30.17, 29.98, 25.62, 25.21; ^{27}Al NMR (130 MHz, toluene-d_8) 35.33. Anal. Calcd for $C_{32}H_{47}AlN_2O_5$: C, 67.82; H, 8.36; N, 4.94. Found: C, 67.81; H, 8.32; N, 4.89.

2 (R = Br): ^{1}H NMR (500 MHz, toluene-d_8) δ 7.63 (d, $J = 2.6$ Hz, 2H, Ar*H*), 7.17 (s, 2H, C*H*═N), 6.89 (d, $J = 2.6$ Hz, 2H, Ar*H*), 3.97 (septet, $J = 5.9$ Hz, 1H, OC*H*$(CH_3)_2$), 3.25 (d, $J = 12.1$ Hz, 2H, NCH*'H*$(CH_3)_2$CH*'H*N), 2.59 (d, $J = 12.1$ Hz, 2H, NC*H'*H$(CH_3)_2$C*H'*HN), 1.56 (s, 18H, Ar-*t-Bu*), 1.08 (d, $J = 6.0$ Hz, 6H, OCH(C$H_3)_2$), 0.72 (s, 3H, $NCH_2(CH_3)$*'*(CH_3)CH_2N), 0.47 (s, 3H, NCH_2(CH_3)*'*$(CH_3)CH_2$N); ^{13}C NMR (125 MHz, toluene-d_8) δ 168.85, 164.63, 144.34, 135.59, 133.47, 120.92, 108.07, 67.89, 63.10, 35.91, 35.50, 29.66, 28.20, 25.55, 25.07; ^{27}Al NMR (130 MHz, toluene-d_8) δ 33.63. Anal. Calcd for $C_{30}H_{41}AlBr_2N_2O_3$: C, 54.23; H, 6.22; N, 4.22. Found: C, 54.29; H, 6.27; N, 4.22.

2 (R = NO_2): ^{1}H NMR (500 MHz, toluene-d_8) δ 8.43 (d, $J = 3.0$ Hz, 2H, Ar*H*), 7.81 (d, $J = 3.0$ Hz, 2H, Ar*H*), 7.14 (s, 2H, C*H*═N), 3.85 (septet, $J = 6.0$ Hz, 1H, OC*H*$(CH_3)_2$), 3.21 (d, $J = 12.1$ Hz, 2H, NCH*'H*$(CH_3)_2$CH*'H*N), 2.59 (d, $J = 12.1$ Hz, 2H, NC*H'*H$(CH_3)_2$C*H'*HN), 1.53 (s, 18H, Ar-*t-Bu*), 1.04 (d, $J = 6.0$ Hz, 6H, OCH(C$H_3)_2$), 0.71 (s, 3H, $NCH_2(CH_3)$*'*(CH_3)CH_2N), 0.50 (s, 3H, NCH_2(CH_3)*'*$(CH_3)CH_2$N); ^{13}C NMR (125 MHz, toluene-d_8) δ 169.70, 169.48, 142.80, 138.23, 129.18, 127.39, 118.22, 67.80, 63.28, 35.91, 35.42, 29.41, 27.98, 25.56, 25.01; ^{27}Al NMR (130 MHz, toluene-d_8) δ 33.40. Anal. Calcd for $C_{30}H_{41}AlN_4O_7$: C, 60.39; H, 6.93; N, 9.39. Found: C, 60.15; H, 6.55; N, 8.71.

Kinetics Measurements and Analysis A procedure for a typical kinetic run is as follows. In a nitrogen-filled glovebox, an NMR tube dried in a vacuum oven at ambient temperature was charged with 500 µL of a stock solution of catalyst in toluene-d_8 (0.0098 M) and 10 µL of the internal standard 1,4-bis(trimethylsilyl)benzene in toluene-d_8 (0.28 M). The NMR tube was capped with a septum and wrapped with black electric tape. A gastight syringe was loaded with 190 µL of a stock solution of CL in toluene-d_8 (7.4 M) and capped with a septum to prevent air contamination during the experiment setup. The target concentrations for the NMR reaction were 0.007 M catalyst, 0.004 M internal standard, and 2.0 M CL. The NMR tube and loaded syringe were taken out of the glovebox and brought to the spectrometer. A pure methanol standard was used to calibrate the temperature of the spectrometer (500 MHz Bruker Avance III). In order to accurately determine catalyst concentration, a relaxation relay of 10 s was used to ensure complete relaxation for quantification integrations. A ^{1}H NMR spectrum of the catalyst and internal standard was measured, and then the NMR tube was ejected from the spectrometer and CL was injected through the septum. The NMR tube was aggressively shaken and inverted before being reinserted into the spectrometer. The time between the CL injection and the start of ^{1}H NMR data acquisition was recorded in minutes. An array of spectra was taken every 48 s (four scans) for most kinetic runs except for the runs with R = NO_2 (288 and 293 K) and R = Br (273 K), where a spectrum was taken every 24 s (two scans) and 96 s (eight scans), respectively. The acquisition parameters were as follows: relaxation delay 10 s, 30° pulse width 3.9, gain of 10 or 16 depending on the NMR probe used, and acquisition time 2 s. Samples were spun, and autoshim was employed to allow for shimming during kinetic runs. The arrayed experiment was allowed to proceed until the disappearance of the CL peaks, indicating complete polymerization. For R = NO_2 (273 K), the kinetic runs were halted prior to the complete disappearance of CL peaks due to the loss of shims by the spectrometer. For each catalyst, triplicate reactions were performed at four different temperatures. The obtained arrayed NMR data were phased and baseline corrected before being integrated, using Mestrenova (http://mestrelab.com/).

Using the peak integrations, absolute concentrations of all species as a function of time were calculated relative to the concentration of internal standard. The reaction time was calculated in seconds from the known duration of each spectrum and the time between the CL injection and the start of the ^{1}H NMR data acquisition. The concentration vs time data were entered into the program COPASI and fit to eq S1 in the Supporting Information to obtain K_M and $V_{\max}$ values. The reaction rates were calculated using eq S1 and plotted as a function of [CL]; full details of the fits and results are provided as Supporting Information. All linear and nonlinear curve fits were performed using Origin 9.1 SR2 software (OriginLab, Northampton, MA).

Binding Study with γ-Butyrolactone In a nitrogen-filled glovebox, six NMR tubes dried in a vacuum oven at ambient temperature were each charged with 500 µL of a stock solution of catalyst **2** (R = OMe, Br, NO_2) in toluene-d_8(0.0074–0.0078 M). Different amounts (10–190 µL) of a 7.38 M stock solution of BL were added to each tube. Toluene-d_8 was added to some of the tubes to achieve an overall volume of 690 µL. The NMR tubes were capped and shaken. The final concentrations for BL were 0.11, 0.25, 0.50, 0.75, 1.0, 1.5 and 2.0 M, while the catalyst concentration ranged from 0.005 to 0.007 M. The reactions were monitored at 293 K by ^{1}H NMR spectroscopy (500 MHz Bruker Avance III) using the same parameters as the kinetic runs. This experiment was run in triplicate for each catalyst, and the spectra were processed using Mestrenova and analyzed by NMR peak analysis using Origin 9.1 SR2 software.

Density Functional Calculations Molecular structures were optimized at the M06-L level[33] of density functional theory employing the 6-31+G(d,p) basis set.[34] The nature of all stationary points was confirmed by computation of analytic vibrational frequencies, which were also employed to compute vibrational contributions to the molecular partition function,

replacing all vibrations below 50 cm^{-1} with values of 50 cm^{-1} in order to correct for the well-known deficiency of the quantum mechanical harmonic oscillator approximation when applied to very low frequency motions.[35,36] Improved free energies were computed by summing thermal contributions from this lower level of theory with single-point electronic energies computed at the M06-2X level[37] of density functional theory employing the 6-311+G(d,p) basis set.[34] Solvation effects for toluene as solvent were included during single-point energy calculations employing the SMD solvation model.[38]

There are a very large number of conformational and configurational possibilities associated with the binding of the catalyst with caprolactone. In this work, we consider a limited number of structures, primarily to compare with prior work involving a different, but analogous, catalyst. A more exhaustive survey of the various possible complexes and reaction paths undertaken for an analogue of the catalyst in this work from which alkyl groups substituting the ligand were removed suggests that the specific structures reported in this study are indeed relevant as low-energy stationary points, and results from that work on the reduced catalyst are summarized in the Supporting Information.

Calculations were carried out with the Gaussian 09 suite of electronic structure programs.[39] CM5 charges were computed using the auxiliary CM5PAC program.[40]

2.2.6 Associated Content

The Supporting Information is available free of charge on the ACS Publications website at DOI: 10.1021/acscatal.5b02607:

- X-ray data (CIF)
- Spectroscopic and kinetics data and fits and computational details (PDF)

2.2.7 Notes

The authors declares no competing financial interest.

2.2.8 Acknowledgments

Funding for this project was provided by the Center for Sustainable Polymers, a National Science Foundation sup- ported Center for Chemical Innovation (CHE-1413862). The X-ray diffraction experiments were performed using a crystal diffractometer acquired through NSF-MRI Award CHE-1229400. The NMR experiments were performed on Bruker Avance III 500 MHz spectrometers acquired through NIH Award S10OD011952. We thank Dr. Letitia Yao for her help with NMR kinetics experiments.

References

[1] Dubois, P., Coulembier, O., Raquez, J.-M., Eds. *Handbook of Ring-Opening Polymerization*; Wiley: Weinheim, Germany, 2009.

[2] Kiesewetter, M. K.; Shin, E. J.; Hedrick, J. L.; Waymouth, R. M. *Macromolecules* **2010**, *43*, 2093–2107.

[3] Thomas, C. M. *Chem. Soc. Rev.* **2010**, *39*, 165–173.

[4] Dijkstra, P. J.; Du, H.; Feijen, J. *Polym. Chem.* **2011**, *2*, 520–527.

[5] Buchard, A.; Bakewell, C.; Weiner, J.; Williams, C. In *Topics in Organometallic Chemistry: Organometallics and Renewables*; Meier, M. A. R., Weckhuysen, B. M., Bruijnincx, P. C. A., Eds.; Springer: Berlin, Heidelberg, Vol. 39; pp 175–224.

[6] Dagorne, S.; Normand, M.; Kirillov, E.; Carpentier, J.-F. 2013; Vol. 257; pp 1869–1886.

[7] Sauer, A.; Kapelski, A.; Fliedel, C.; Dagorne, S.; Kol, M.; Okuda, J. *Dalton Trans.* **2013**, *42*, 9007–9017.

[8] Hillmyer, M. A.; Tolman, W. B. *Acc. Chem. Res.* **2014**, *47*, 2390–2396.

[9] Guillaume, S. M.; Kirillov, E.; Sarazin, Y.; Carpentier, J.-F. *Chem. - Eur. J.* **2015**, *21*, 7988–8003.

[10] Borner, J.; Florke, U.; Gloge, T.; Bannenberg, T.; Tamm, M.; Jones, M. D.; Doring, A.; Kuckling, D.; Herres-Pawlis, S. *J. Mol. Catal. A: Chem.* **2010**, *316*, 139–145.

[11] Altenbuchner, P. T.; Kronast, A.; Kissling, S.; Vagin, S. I.; Herdtweck, E.; Poethig, A.; Deglmann, P.; Loos, R.; Rieger, B. *Chem. - Eur. J.* **2015**, *21*, 13609–13617.

[12] Chang, M. C.; Lu, W. Y.; Chang, H. Y.; Lai, Y. C.; Chiang, M. Y.; Chen, H. Y.; Chen, H. Y. *Inorg. Chem.* **2015**, *54*, 11292–11298.

[13] Horeglad, P.; Cybularczyk, M.; Trzaskowski, B.; Zukowska, G. Z.; Dranka, M.; Zachara, J. *Organometallics* **2015**, *34*, 3480–3496.

[14] Roymuhury, S. K.; Chakraborty, D.; Ramkumar, V. *Eur. Polym. J.* **2015**, *70*, 203–214.

[15] Tabthong, S.; Nanok, T.; Sumrit, P.; Kongsaeree, P.; Prabpai, S.; Chuawong, P.; Hormnirun, P. *Macromolecules* **2015**, *48*, 6846–6861.

[16] Hormnirun, P.; Marshall, E. L.; Gibson, V. C.; Pugh, R. I.; White, A. J. P. *Proc. Natl. Acad. Sci. U. S. A.* **2006**, *103*, 15343–15348.

[17] Ding, K.; Miranda, M. O.; Moscato-Goodpaster, B.; Ajellal, N.; Breyfogle, L. E.; Hermes, E. D.; Schaller, C. P.; Roe, S. E.; Cramer, C. J.; Hillmyer, M. A.; Tolman, W. B. *Macromolecules* **2012**, *45*, 5387–5396.

[18] Miranda, M. O.; DePorre, Y.; Vazquez-Lima, H.; Johnson, M. A.; Marell, D. J.; Cramer, C. J.; Tolman, W. B. *Inorg. Chem.* **2013**, *52*, 13692–13701.

[19] Addison, A. W.; Rao, T. N.; Reedijk, J.; Rijn, J. V.; Verschoor, G. C. *J. Chem. Soc., Dalton Trans.* **1984**, 1349–1356.

[20] Nomura, N.; Ishii, R.; Yamamoto, Y.; Kondo, T. *Chem. Eur. J.* **2007**, *13*, 4433–4451.

[21] Du, H.; Pang, X.; Yu, H.; Zhuang, X.; Chen, X.; Cui, D.; Wang, X.; Jing, X. *Macromolecules* **2007**, *40*, 1904–1913.

[22] Chen, H.-L.; Dutta, S.; Huang, P.-Y.; Lin, C.-C. *Organometallics* **2012**, *31*, 2016–2025.

[23] Agatemor, C.; Arnold, A. E.; Cross, E. D.; Decken, A.; Shaver, M. P. *J. Organomet. Chem.* **2013**, *745–746*, 335–340.

[24] Blackmond, D. *Angew. Chem., Int. Ed.* **2005**, *44*, 4302–4320.

[25] Duda, A.; Biela, T.; Libiszowski, J.; Penczek, S.; Dubois, P.; Mecerreyes, D.; Jérôme, R. *Polym. Degrad. Stab.* **1998**, *59*, 215–222.

[26] Saiyasombat, W.; Molloy, R.; Nicholson, T. M.; Johnson, A. F.; Ward, I. M.; Poshyachinda, S. *Polymer* **1998**, *39*, 5581–5585.

[27] Houk, K. N.; Jabbari, A.; Hall, H. K.; Alemán, C. *J. Org. Chem.* **2008**, *73*, 2674–2678.

[28] Alemán, C.; Betran, O.; Casanovas, J.; Houk, K. N.; Hall, H. K. *J. Org. Chem.* **2009**, *74*, 6237–6244.

[29] Marenich, A. V.; Jerome, S. V.; Cramer, C. J.; Truhlar, D. G. *J. Chem. Theory Comput.* **2012**, *8*, 527–541.

[30] Kurahashi, T.; Fujii, H. *J. Am. Chem. Soc.* **2011**, *133*, 8307–8316.

[31] Cavazzini, M.; Manfredi, A.; Montanari, F.; Quici, S.; Pozzi, G. *Eur. J. Org. Chem.* **2001**, 4639–4649.

[32] Braun, M.; Fleischer, R.; Mai, B.; Schneider, M.-A.; Lachenicht, S. *Adv. Synth. Catal.* **2004**, *346*, 474–482.

[33] Zhao, Y.; Truhlar, D. G. *J. Chem. Phys.* **2006**, *125*, 194101/1–194101/18.

[34] Hehre, W. J.; Radom, L.; Schleyer, P. v. R.; Pople, J. A. *Ab Initio Molecular Orbital Theory*; Wiley: New York, 1986.

[35] Cramer, C. J. *Essentials of Computational Chemistry: Theories and MOdels*, 2nd ed.; John Wiley & Sons: Chichester, U.K., 2004.

[36] Ribeiro, R. F.; Marenich, A. V.; Cramer, C. J.; Truhlar, D. G. *J. Phys. Chem. B* **2011**, *115*, 14556–14562.

[37] Zhao, Y.; Truhlar, D. G. *Theor. Chem. Acc.* **2008**, *120*, 215–241.

[38] Marenich, A. V.; Cramer, C. J.; Truhlar, D. G. *J. Phys. Chem. B* **2009**, *113*, 6378–6396.

[39] Frisch, M. J. Gaussian 09, Revision C.01. 2010; See Supporting Information for full reference.

[40] Marenich, A. V.; Cramer, C. J.; Truhlar, D. G. CM5PAC: University of Minnesota, Minneapolis, MN, 2011.

3. Probing Electronic Properties of Small-Molecule Systems

3.1 Rate-Determining Attack on Substrate Precedes Rieske Cluster Oxidation during Cis-Dihydroxylation by Benzoate Dioxygenase

3.1.1 Introduction

Rieske oxygenases catalyze a diverse repertoire of chemical reactions including oxygenation of hydrocarbons, O- and N-demethylations, N-oxidations, and C–C bond formation in pathways for catabolism of hydrocarbons and biosynthesis of medically significant natural products.[1] The Rieske oxygenase subclass termed Rieske dearomatizing dioxygenases (RDDs) comprises the only known enzymes that catalyze dearomatizing cis-dihydroxylation of aromatic compounds (Figure 3.1). This reaction activates otherwise stable aromatic compounds, making RDDs effective agents for bioremediation.[2,3]

Fig. 3.1 Reaction of the RDD Benzoate 1,2-Dioxygenase

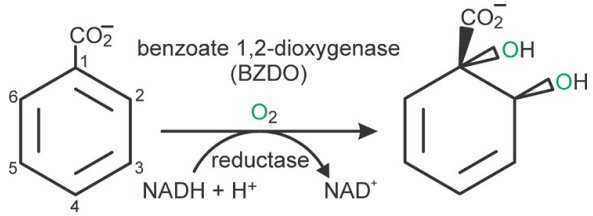

Another type of application stems from the ability of RDDs to produce large quantities of regio- and stereospecific cis-diols as important synthetic building blocks for streamlining

synthesis of drugs and antibiotics.[4] A complete understanding of the catalytic mechanism of RDDs will aid further development and utilization of these applications and provide guiding insights for mechanistic studies of the broad class of Rieske oxygenases.

The benzoate 1,2-dioxygenase system is an archetypal RDD that utilizes the electrons from NADH to catalyze the conversion of benzoate to (1S,6R)-1,6-*cis*-dihydroxycyclohexa-2,4-diene-1-carboxy acid (benzoate *cis*-diol), inserting both atoms from O_2 into the substrate, forming the product (Figure 3.1).[5–7] This system consists of reductase (BZDR) and oxygenase (BZDO) components. Each α-subunit of the $(\alpha\beta)_3$ BZDO contains a [2Fe–2S] Rieske cluster and a nonheme mononuclear Fe coordinated by two His and one Asp residues (a 2-His-1-carboxylate facial triad)[8] in addition to 1 or 2 solvent molecules.[9,10] The conserved quaternary structure of RDDs places the Rieske cluster of one α-subunit within 15 Å of the mononuclear iron of the adjacent α-subunit, suggesting that this pair of metal centers comprises the functional unit of the enzyme.[10,11] Substrates bind near (but not to) the mononuclear Fe, showing that this is the site of O_2 activation and cis-dihydroxylation.[12–15] Single-turnover experiments have shown that reduction of both the Rieske cluster and the mononuclear iron is required for normal catalysis and that one electron from each metal center is used during the cis-dihydroxylation reaction.[16] A conserved Asp residue links the two metal centers via hydrogen bonding and appears to mediate the electron transfer from the Rieske cluster to the mononuclear iron during the reaction.[11,17–20] Conformational changes involving the pathway between the metal centers also appear to play a role in the complex regulatory mechanism of the enzyme, which ensures that the Rieske cluster is reduced and the substrate is correctly bound in the active site before O_2 can be activated at the mononuclear Fe(II).[9,21–23] This mitigates formation of deleterious reactive oxygen species.[7,24]

RDDs have characteristics that make them mechanistically distinct from other Fe-dependent dioxygenases and monooxygenases. For example, many nonheme dioxygenase

classes that are reactive in the Fe(II) state utilize the 2-His-1-carboxylate facial triad iron binding ligation like the RDDs.[25] However, these dioxygenases extract all four electrons required for O_2 reduction from the substrate or cosubstrate, whereas RDDs ultimately utilize two electrons from the substrate and two from NADH. Monooxygenases, like methyl monooxygenase (MMO) or cytochrome P450, also extract two electrons from both substrate and NADH, but the products are oxidized substrate and water rather than a dihydroxylated substrate.[26–28] It is noteworthy that well-characterized Rieske monooxygenases exist that are structurally similar to RDDs but exhibit the same NADH and O_2 stoichiometry and single oxygen atom incorporation pattern as MMO or cytochrome P450.[21,29] These similarities have led to mechanistic theories for RDDs along the line of monooxygenase rather than dioxygenase enzymes.

A hypothesis for the mechanism of RDDs based on typical monooxygenase chemistry is shown in Figure 3.2 (purple arrows).[7] Substrate binds to the enzyme with the Rieske cluster, and mononuclear Fe reduced ($Rieske^{red}$/Fe(II)), resulting in solvent release from the mononuclear Fe(II). Then, O_2 binds to the Fe(II), and an electron from the reduced Rieske cluster is transferred to the mononuclear Fe–O_2 complex to yield a (hydro)peroxo intermediate similar to those previously proposed for all well-characterized monooxygenases.[30–33] The (hydro)peroxo species might be reactive with substrate, or the O–O bond could cleave to yield a reactive HO–Fe(V)═O species (red bracketed box in Figure 3.2).

Fig. 3.2 Proposed Reaction Cycle and Peroxide Shunt of RDD Enzymes

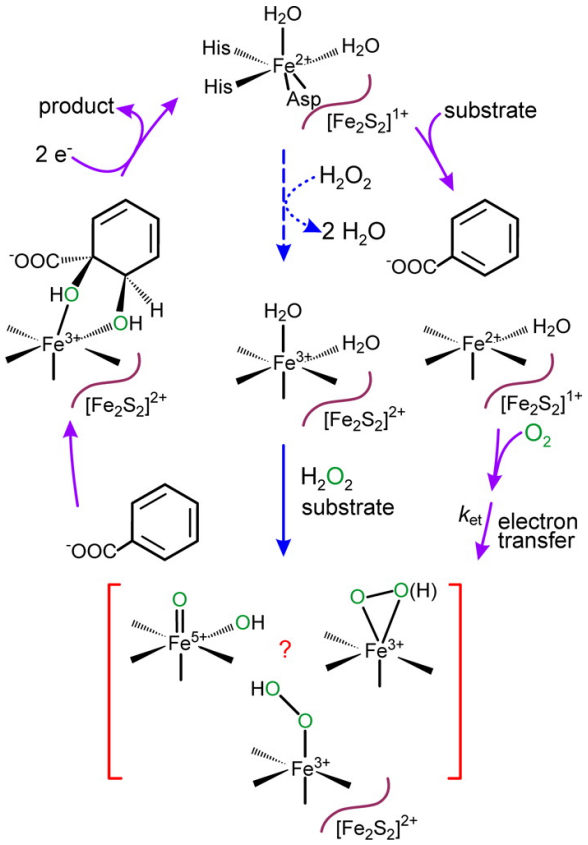

The results from experimental and computational approaches have supported the monooxygenase-like mechanism of RDD catalysis, but they have not agreed on the identity of the reactive species performing the initial substrate oxidation.[10,25] *In crystallo* characterization of tertiary ESO_2 complexes in the RDDs naphthalene 1,2-dioxygenase (NDO) and carbazole 1,9a-dioxygenase (CarDO) have shown O_2 binding in side-on or end-on configuration to the mononuclear iron, resulting in lengthening of the O–O bond, consistent with formation of a peroxo species.[13,15] Also, BZDO with both the mononuclear Fe and Rieske cluster oxidized can form significant yields of product after addition of substrate and H_2O_2 in a peroxide shunt reaction (Figure 3.2, blue arrows).[34] During these reactions, the observed rate constants of single turnover are decreased by a factor of $\sim 2 \times 10^5$.

Analysis of the peroxide shunt reaction revealed formation of a transient S = 5/8 ferric species with unusual spectroscopic properties consistent with those of a side-on bound Fe(III)–(hydro)peroxo species. These observations suggest that an Fe(III)–(hydro)peroxo is on the reaction coordinate during peroxide shunt reactions and may also be important during catalytic turnover.

Density functional theory (DFT) studies based on active site models of the structurally homologous RDDs, NDO and nitrobenzene 1,2-dioxygenase (NBDO), have reached different conclusions regarding the reaction coordinate. The calculations with NDO showed that O–O bond cleavage prior to substrate attack to yield an HO–Fe(V)═O is too energetically demanding. Instead, a lower energy pathway was proposed using a side-on Fe(III)–(hydro)peroxo proceeding to product through an epoxide intermediate.[35] However, recently, conflicting results were obtained in a study of NBDO, which showed that such a peroxo attack is more energetic than O–O bond cleavage.[36]

Several insights have been gained from studies with small-molecule Fe–chelate complexes that mimic the active site of RDDs. Investigations of olefin oxidation using various complexes showed two distinct reactive pathways to cis-dihydroxylation.[37] Both types of reaction rely on the availability of two adjacent ligand sites on the iron, as is apparently the case for RDDs. In one type of reaction catalyzed by some low-spin Fe(III)–(hydro)peroxo complexes within TPA or BPMEN ligands, one oxygen from water is incorporated into the cis-diol product in addition to one oxygen from H_2O_2.[38] This observation and subsequent experiments have demonstrated a water-assisted cleavage of the O–O bond to form an HO–Fe(V)═O reactive species.[39] In contrast, both cis-diol oxygens were found to derive from peroxide when the reactions were carried out with high-spin TPA and BPMEN Fe–chelate compounds.[37] The mononuclear iron of RDDs is high-spin in both the ferric and ferrous states,[7] but whether this correlates with the type of reactive species formed is unknown. Another study using high-spin TMC–Fe(III)–hydroperoxo complexes has shown that the S = 5/2 state increased

the oxidation potential.[40] This generates a more potent species for electrophilic catalysis, thereby providing evidence that an Fe–hydroperoxo could be active in RDDs.

The focus on two-electron O_2 activation in RDDs has limited consideration of another commonly employed mechanistic strategy in the 2-His-1-carboxylate family involving one-electron-reduced O_2. Indeed, the initial attacking species in enzymes such as extradiol ring-cleaving dioxygenases[41,42] and isopenicillin N-synthase[43] are proposed to be metal-bound superoxo moieties.[44,45]

A potential difficulty with a mechanism that invokes an Fe(III)–peroxo or HO–Fe(V)═O reactive species for RDDs derives from our past studies that showed that the rate of electron transfer from the Rieske cluster to the mononuclear iron site within BZDO is influenced by the functional groups on the aromatic ring of benzoate.[7] This observation might imply that the reaction of some type of Fe–oxygen intermediate with substrate occurs before formation of a two-electron-reduced species. Alternatively, it could reflect steric effects on the substrate position in the active site. Here, the transient kinetics of electron transfer within BZDO during a single turnover are examined for benzoate and a variety of fluorinated benzoates selected in order to limit steric effects. It is shown that the step in which activated O_2 first attacks the substrate is rate-limiting and that this step is likely to involve a metal-bound species with superoxo character. The study provides new insight into the detailed steps of oxygen activation and reaction that ensure both specificity and efficient catalysis in Rieske dioxygenases.

3.1.2 Experimental Procedures

Standard materials and procedures are described in the Supporting Information. Authentic standards of dearomatized 1,2-cis-diol products of benzoate and the fluorobenzoates used

here were prepared and characterized as described in the Supporting Information. Cloning, heterologous expression, and purification of BZDO and BZDR from the genomic DNA of *Pseudomonas putida* mt-2 were carried out using modifications of previously described methods.[7] The current methods for these procedures are described in the Supporting Information.

Stopped-Flow Analysis of Single-Turnover Reactions Stopped-flow experiments were performed at 4 °C in 50 mM MOPS buffer, pH 6.8, plus 100 mM NaCl using an Applied Photophysics SX.18MV configured for single-wavelength data collection at 464 nm. The instrument was made anaerobic by flushing with a dithionite solution and then anaerobic buffer. BZDO (60 µM) was reduced as described in the Supporting Information and mixed with a solution containing varied concentrations of substrate and O_2 (see figure legends). Fitting procedures for time courses to multiexponential equations and concentrations dependencies to hyperbolic expressions are described in the Supporting Information

Chemical Quench and Rapid Chemical Quench Product Analysis Reduced BZDO (400 µM) was mixed 1:1 with reaction buffer (50 mM MOPS buffer, pH 6.8, plus 100 mM NaCl) saturated with O_2 (1.8 mM at 4 °C) containing benzoate or a fluorobenzoate (10 mM). For time point quenches of completed reactions (>3 min), 200 µL of the reaction mixture was pipetted into 800 µL of rapidly stirring 1 M HCl. Rapid quenches were accomplished in an identical manner except that an Update 715 ram syringe controller was used to mix and dispense the reactants. Sodium formate (50 µL of 7.5 M) and NaOH (50 µL of 10 M) were added to the quenched solution to buffer the pH to ∼3.5, and 400 µL of H_2O was added to bring the final volume to 1.5 mL. Each sample was vortexed (˜20 s), and the denatured protein was removed from the solution by centrifugation at 4 °C before HPLC was used to analyze 1 mL of the quenched reaction. HPLC was performed on a Waters system with a

1525 binary pump, 2487 dual-wavelength UV/vis detector, and an Agilent Zorbax SB C18 column (4.6 mm × 150 mm, 5 µm) with an aqueous gradient of 4 to 100% acetonitrile/0.1% formic acid over 7.5 min following an isocratic flow at 4% acetonitrile/0.1% formic acid for 2.5 min. The cis-diol products were detected by their optical absorption at 262 nm. The methods used to verify the observed HPLC peaks and construct standard curves for quantification using authentic standards are described in the Supporting Information.

Computational Methods Molecular geometries for parent and various fluoro-substituted benzoic acids were optimized at the M06-2X level of density functional theory[46] employing the 6-311+(2df,p) basis set.[47] Both conjugate acid and conjugate base forms were considered in the optimizations, and the calculations were undertaken both in the gas phase and also including condensed phase effects using the SMD continuum aqueous solvation model.[48,49] Charges were computed for the optimized structures at the same level of theory employed for the optimizations, summing the charges for carbon atoms with those for attached H atoms in order to compute a net group partial charge for the C(2) C–H group. In the case of the conjugate acids, variations in this charge as a function of the position of the hydroxyl group of the carboxylic acid (distal or proximal to the carbon defined as C(2)) was, in every instance, 0.009 au for gas phase calculations but no more than 0.001 au with the SMD solvation model. Geometry optimizations were accomplished with the Gaussian09 suite of electronic structure programs,[50] and CM5 charges were computed using CM5PAC.[51]

3.1.3 Results

Product Formation Correlates with Only One Step of the Multistep Rieske Cluster Oxidation Reaction Single-turnover reactions were conducted by rapidly mixing reduced BZDO in a stopped-flow instrument with buffer containing substrate and O_2

(saturated). Only a single turnover can occur because there is no additional reductant present to reduce the metal centers for a second turnover and the ferric mononuclear iron must be reduced in order for product to dissociate.[16] Figure 3.3 shows that spectra collected during single-turnover reactions monitored in this study fit well as linear combinations of the fully oxidized and reduced Rieske cluster spectra, demonstrating that no other chromophoric intermediate(s) accumulate to detectable concentrations.

Fig. 3.3 Stopped-Flow Spectroscopy Results for Partial Reduction of BZDO

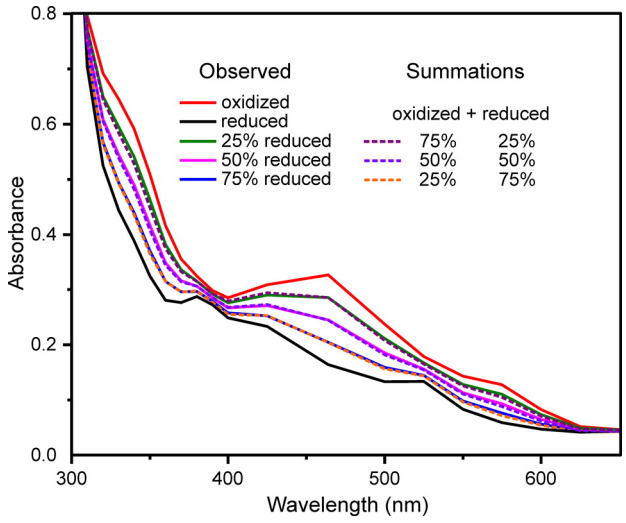

Optical changes during a single turnover with benzoate are well-accounted for by linear summations of the spectra of the reduced and oxidized Rieske cluster. Selected optical spectra observed after reduced BZDO (100 µM) was mixed with an O_2-saturated reaction buffer containing benzoate (20 mM) at 4 °C in a stopped-flow spectrophotometer. The spectra are combinations of 21 single-wavelength time courses collected from 300 to 725 nm. The simulated spectra were calculated by summing the indicated fractions of the fully reduced and fully oxidized Rieske cluster spectra.

Figure 3.4A shows the single-wavelength time courses of Rieske cluster oxidation during single-turnover reactions containing benzoate or one of several fluorinated benzoates selected to yield only one cis-diol product. Each reaction displayed two characteristics previously observed for the turnover of other substrates.[7] First, a satisfactory simulation of the time course of the Rieske cluster oxidation under pseudo-first-order conditions requires more than

one exponential phase term (Figure 3.4B). This shows that there is more than one step in the Rieske cluster oxidation process for each substrate, but it does not indicate whether the steps occur in sequence or in parallel or whether all of the steps are catalytically relevant. Second, the chemical nature of the substrate (in this case, the number and position of the fluorine aromatic substituents) changes the magnitudes of observed reciprocal relaxation times (RRTs) (Figure 3.4A and Table 3.1).

Fig. 3.4 Rieske Cluster Oxidation Rate Dependence on Substrate Type

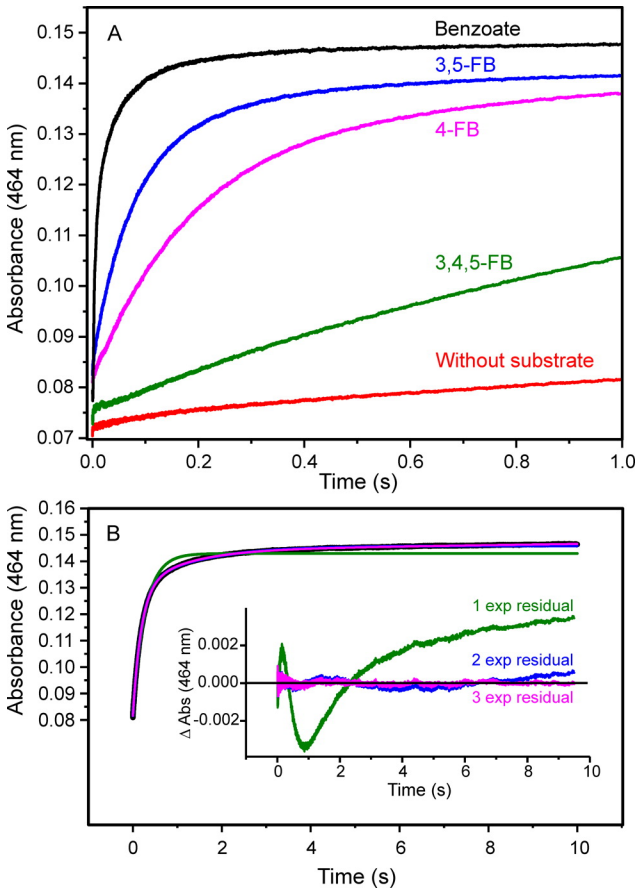

Rieske cluster oxidation rates during a single turnover depend upon the type of substrate present. (A) Optical change at 464 nm when reduced BZDO (60 µM) was mixed with an O_2-saturated reaction buffer containing the indicated substrate (5 mM) at 4 °C in a stopped-flow spectrophotometer. (B) The resulting optical change at 464 nm with 4-fluorobenzoate and residuals from single-, double-, and triple-exponential function fits.

The catalytic relevance of the steps in a multistep reaction can sometimes be evaluated from the magnitudes of the RRTs in comparison to the k_{cat} values for the reactions. This is straightforward when the steps are irreversible, in which case each RRT is the rate constant for a specific step. Many of the steps in the current case are likely to be effectively irreversible: (1) electron transfer across a substantial potential gradient,[i, 52–54] (2) O–O bond cleavage, and (3) cis-dihydroxylation. (The conclusion of irreversible steps is verified by results shown below.) With benzoate as the substrate, three substrate-dependent (see below) exponential phases are observed, whereas the reactions for the fluorobenzoates each exhibit only two substrate-dependent phases. All of the substrate-dependent phases are faster than the respective k_{cat} values for the reactions and thus all of the corresponding steps (assumed to be irreversible) must initially be considered relevant to the true catalytic process of the enzyme (Table 3.1). In contrast, each reaction displayed one or more low-amplitude substrate concentration-independent phases with RRTs much slower than k_{cat} and are therefore not catalytically relevant. Despite the observation of at least two kinetically relevant phases, it is difficult to rationalize how a single, one-electron Rieske cluster oxidation event could occur in a multistep sequential reaction. Thus, it is important to identify functionally relevant steps, which may be a subset of kinetically competent steps.

One strategy that may distinguish functionally relevant from nonproductive Rieske oxidation steps is to determine the number of steps involved in product formation and their rate constant(s). Rapid chemical quench samples taken at specific times during a single turnover were analyzed by HPLC to determine the rate constant(s) and fractional yield of

[i] In most characterized RDDs, the as-isolated state of the enzyme is composed of 100% oxidized Rieske cluster (Fe(III)Fe(III)) and 100% ferrous mononuclear Fe.[7] No equilibrium is observed between the reduced mononuclear Fe and the oxidized Rieske cluster, showing that the reduction potentials are far enough apart that the electron transfer is irreversible. BZDO is unique in that it can be isolated in either the typical state or in a fully oxidized state with a ferric mononuclear Fe.[52] When BZDO is fully oxidized, addition of stoichiometric reducing equivalents (relative to active sites) from dithionite results in the typical state of oxidized Rieske cluster and ferrous mononuclear Fe.[52] The reduction potentials of the Rieske cluster and mononuclear Fe for the Rieske monooxygenase putidamonoxin have been reported to be 5 and $\geq$200 mV, respectively.[53,54]

product formation, as shown in Figures 3.5 and S1 and summarized in Table 3.1. For each substrate, a single new HPLC peak appears at the same retention time as that for purified authentic standards of the cis-diol product (Figures 3.5 and S1, insets). In contrast to the time course for Rieske cluster oxidation, the accumulation of cis-diol products can be fit to a single-exponential function (Figures 3.5 and S1). For each substrate, the k_{obs} for product formation is within experimental error of RRT-1 (Table 3.1). Under the assumption of irreversible steps in the product formation process, this suggests that the product is formed in only one step of the Rieske oxidation reaction. If so, then the fraction of the overall amplitude of the Rieske oxidation represented in RRT-1 should correlate with the fractional yield of each cis-diol product. It is shown in Table 3.1 that this prediction is confirmed. While the error in the yield data would allow additional phases in the fit, the small amount of product formed during these phases would not correlate with the amplitudes of the slower phases in the optically monitored time course. These results strongly imply that the observed phases do not arise from a multistep, sequential process but instead are the result of independent, parallel, substrate-triggered Rieske oxidation reactions. The reason that the slower substrate-dependent steps do not yield product remains unclear. However, the ability to consider the catalytically relevant Rieske oxidation as a one-step process greatly simplifies the analysis of the mechanism of the cis-diol forming reaction. Accordingly, we will consider only RRT-1 here, and the RRT for this phase will be considered the rate constant for the rate-determining step in the product-forming process.

Table 3.1 Reaction Kinetics and Product Formation During BZDO Single Turnover[a]

Substrate		Steady State	Single Turnover								
		O_2 Uptake	Product Formation		Rieske Reoxidation (464 nm)						
					Substrate-Coupled Product-Forming Oxidation		Substrate-Coupled Non-Product Forming Oxidation				Slow Oxidation Phases[b]
	pK_a	k_{cat}(s^{-1})	k_{obs}(s^{-1})	Fractional Product Yield (%)	RRT-1 (s^{-1})	% Amp	RRT-2 (s^{-1})	% Amp	RRT-3 (s^{-1})	% Amp	% Amp
benzoate	4.2	4.4 ± 0.50	190 ± 50	47 ± 3	184 ± 23	49 ± 5	28 ± 3	32 ± 4	6.8 ± 1.0	14 ± 2	6 ± 2
4-fluoro-benzoate (4-FB)	4.14	0.48 ± 0.06	5.2 ± 1.2	62 ± 5	5.3 ± 0.2	70 ± 3	1.3 ± 0.3	19 ± 2			11 ± 2
3,5-difluoro-benzoate (3,5-FB)	3.5	1.0 ± 0.09	14.6 ± 0.6	63 ± 7	13 ± 1	66 ± 5	3.8 ± 0.6	22 ± 4			12 ± 2
3,4,5-trifluoro-benzoate (3,4,5-FB)	3.46	0.079 ± 0.01	0.70 ± 0.12	51 ± 8	0.86 ± 0.08	66 ± 4	0.28 ± 0.04	24 ± 3			10 ± 2

[a]Reduced BZDO was reacted with O_2-saturated buffer and the substrates shown. The steady-state k_{cat}, product formation rate constant k_{obs}, fractional yield of cis-diol product, and RRT and amplitudes from a multiexponential fit of the time course monitored at 464 nm were determined under the experimental conditions described in Experimental Procedures. [b]Two low-amplitude phases much slower than the k_{cat} were observed in most cases. The slowest phase has the same RRT as the substrate-free reaction ($0.1 s^{-1}$). A slightly faster phase is observed only when a substrate is present, but it exhibits no substrate concentration dependence.

It is important to note that even though it is Rieske oxidation being monitored in the single-step product-forming reaction, the electron transfer *per se* between the Rieske cluster and mononuclear iron site is unlikely to be rate-limiting. In all of the structurally characterized RDDs, the electron transfer between the Rieske cluster and mononuclear iron occurs over a distance of about 15 Å, presumably following a through-bond pathway[10,11] with a large driving force due to the difference in redox potentials of the metal sites.[53,54] A rate constant for electron transfer (k_{et} in Figure 3.2) of 2.2×10^6 s^{-1} was computed based on the NDO active site structure.[55] This rate constant is 4 orders of magnitude larger than those for single turnover with benzoate, the fastest substrate in this study; thus, a step(s) that precedes the electron transfer must be rate-limiting. Nevertheless, the Rieske cluster oxidation allows the rate-determining step in product formation to be characterized and its rate constant determined, as shown below.

Fig. 3.5 Product Analysis Over Time of Rieske Cluster Oxidation Substrates

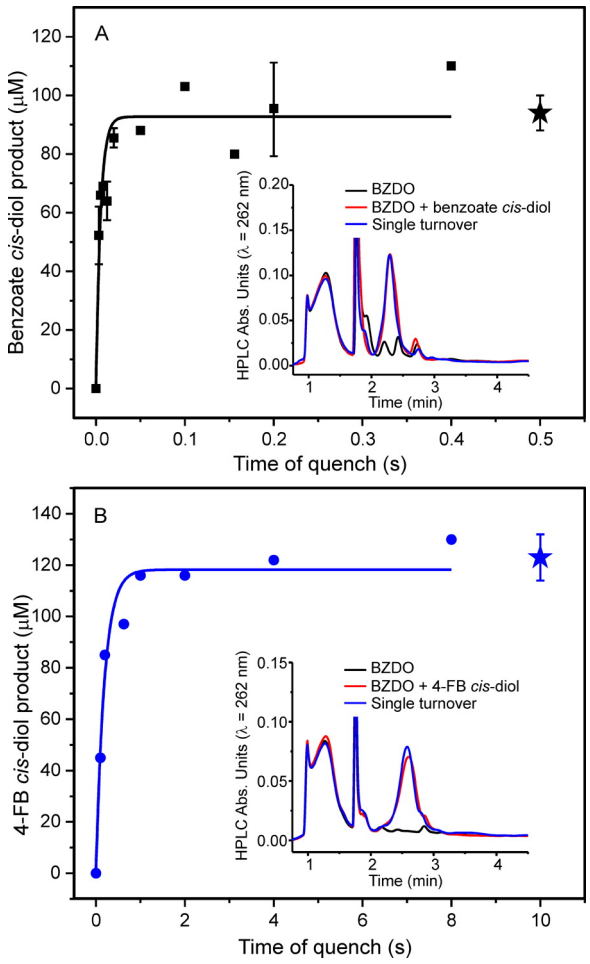

Product analysis of single-turnover reactions shows a correlation with the fast phase of Rieske cluster oxidation. Reduced BZDO (400 µM) was rapidly mixed 1:1 with O_2-saturated reaction buffer containing (A) benzoate (10 mM) or (B) 4-FB (10 mM) and chemically quenched as described in the Experimental Procedures. The yield at the end of the reaction ($\geq$ 4 min) is shown by a star. The product formation time course can be fit to a single-exponential equation for each substrate (solid line), yielding k_{obs}. In each case, a single new HPLC peak consistent with an authentic standard of the cis-diol product is observed (insets). For replicated points, n $\geq$ 3 and the errors bars represent 1 standard deviation of the mean.

The Rate-Limited Step Prior to Rieske Cluster Oxidation Occurs after Initial Substrate and O_2 Binding One possible explanation for the large difference in rate of single turnover between benzoate and the fluorobenzoates is that the fluorine substituent(s)

interferes with substrate and/or O_2 binding despite the comparable van der Waals radii of hydrogen and fluorine. This possibility was examined by studying the substrate and O_2 binding kinetics of each reaction through monitoring the Rieske cluster oxidation time course under pseudo-first-order conditions in substrate and O_2. The rate constant for each substrate reaction exhibits a hyperbolic concentration dependence, as shown in Figures 3.6A and S2A. This result shows that the oxidation of the Rieske cluster is not rate-limited by substrate binding and that the binding reaction is reversibly connected to the true rate-limiting step. For this type of kinetic behavior (see Experimental Procedures in Supporting Information), the apparent K_d for the relatively fast (unobserved) binding reaction is given by the K_d for the titration curve. In the present case, the apparent K_d values for benzoate and 4-FB are approximately the same (Table 3.2).

Fig. 3.6 Substrate and O_2 Concentration Dependence of RRT-1

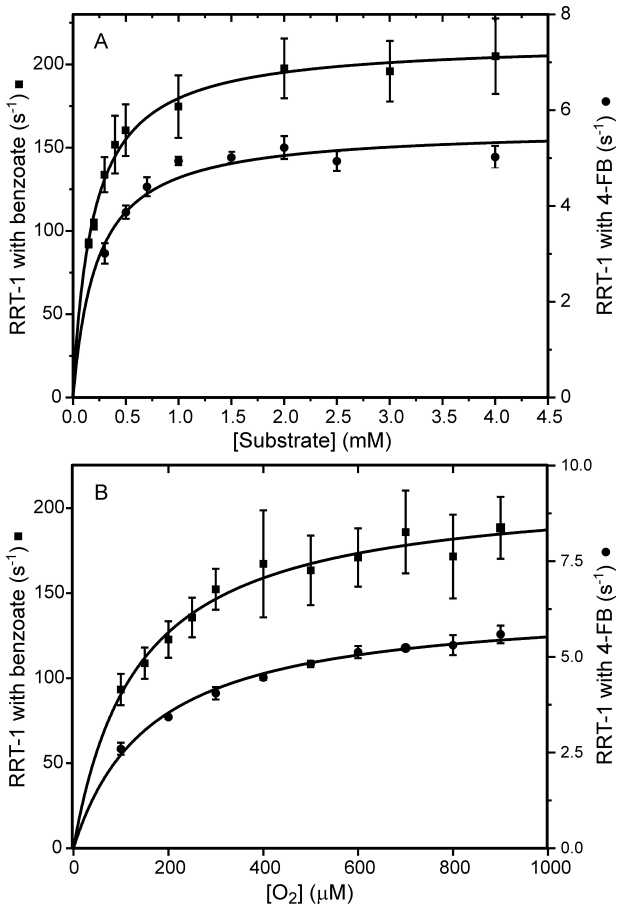

Substrate and O_2 concentration dependence of RRT-1 reveals a common subsequent slow step. Reduced BZDO (60 µM) was mixed 1:1 in a stopped-flow spectrophotometer with reaction buffer containing either (A) O_2 (saturated solution at 4 °C ∼1.8 mM) and varied concentrations of benzoate or 4-FB or (B) varied concentrations of O_2 and benzoate (5 mM) or 4-FB (5 mM). RRT-1 from multiexponential fitting of stopped-flow traces (n ≥ 6 and 4 for the reaction of benzoate and 4FB, respectively) was plotted vs (A) substrate or (B) O_2 concentration. Reported error of each point is 1 standard deviation of the mean. K_d and $k_{forward}$ values were determined by fitting the data to a hyperbolic function (solid curve) and are reported in Table 3.2.

This result shows that replacing hydrogen with a fluorine substituent at carbon 4 does not affect binding affinity. The extrapolated y-intercept and the asymptotic maximum of the curve give information about the true rate-limiting step. In this case, the y-intercept for the titration plots is approximately zero, suggesting that the rate-limiting reaction is effectively

irreversible, supporting the assumptions of irreversibility proposed above. The extrapolated maxima of the titration plots at high substrate concentration are quite different (Table 3.2), reflective of the substrate type dependence of the true rate-limiting step.

The 3,5-fluorobenzoate and 3,4,5-fluorobenzoate substrates also exhibit hyperbolic concentration dependence extrapolating to zero (Figure S2A). Once again, the maximum value for RRT-1 depends on the type of substrate present (Table 3.2). However, the apparent K_{d} values for the unobserved substrate binding step are an order of magnitude higher than those observed for benzoate and 4-fluorobenzoate. Apparently, the presence of fluorine at the 3 and/or 5 positions weakens the binding slightly without causing a change in the product formed. This pair of substrates shows similar values for the apparent K_{d}, as observed for the benzoate, 4-fluorobenzoate pair (Table 3.2).

Table 3.2 Kinetic Parameters from Substrate and O_2 Concentration Dependence of Product Coupled Phase RRT-1[a]

Substrate	$K_{\mathrm{d,substrate}}$ (µM)	k_{forward} (s^{-1})	$K_{\mathrm{d,O_2}}$ (µM)	k_{forward} (s^{-1})
benzoate	191 ± 10	213 ± 4	135 ± 13	212 ± 6
4-FB	226 ± 40	5.6 ± 0.2	163 ± 12	6.4 ± 0.1
3,5-FB	950 ± 140	17 ± 1	150 ± 14	15 ± 0.4
3,4,5-FB	1800 ± 200	1.1 ± 0.1	152 ± 7	0.89 ± 0.02

[a]Apparent K_{d} values determined from hyperbolic fits to the data shown in Figures 3.6 and S2. The value for k_{reverse} is approximately zero in all cases.

Earlier studies have shown that O_2 binding requires both reduction of the Rieske cluster and prior substrate binding (Figure 3.2).[7,52] As shown in Figure 3.6B, the rate constant for the catalytically relevant step preceding Rieske cluster oxidation reaction displays a hyperbolic dependence under pseudo-first-order conditions in O_2 and a large excess of benzoate or 4-FB over the apparent K_{d} values determined from Figure 3.6A. As described above for substrate binding, the hyperbolic plot shows that the O_2 binding reaction is not

rate-limiting. The hyperbolic fits with zero y-intercepts and the similar apparent K_d values for the two substrates confirm that the true rate-limiting reaction is effectively irreversible and that the presence of a fluorine substituent(s) does not significantly affect O_2 binding affinity. The maxima ($k_{forward}$) of the fitted O_2 titration plots are different from each other, but they are similar to the respective values found for the substrate titration plots (Table 3.2). This suggests that the true rate-limiting step is substrate-type-dependent and that the rate constant for substrate and O_2 binding reactions are limited by the same downstream reaction. The same conclusions are reached for the O_2 binding reactions in the presence of 3,5-FB and 3,4,5-FB, as shown in Figure S2B. In the case of O_2 binding, the substrate type causes little change in the apparent K_d.

Binding of the O_2 Surrogate Nitric Oxide to the Mononuclear Fe(II) Is Fast Relative to the Rate of Product Formation Studies of other oxygenases have indicated that O_2 binding might proceed in several steps beginning with the formation of a complex in the active site but not yet with the metal.[56–58] Indeed, a small molecule binding site has been identified in the active site of NDO.[59] As such, binding of O_2 to the mononuclear iron from an active site binding location might be rate-limiting. One means to directly observe small molecule binding to the metal utilizes NO as an O_2 surrogate.[16,60] The chemical and spatial environments of the resulting spin-coupled Fe(III)–NO^- complex can be probed via its characteristic $S = 3/2$ EPR spectrum and broad optical spectrum.[61,62] The optical spectra of reduced BZDO exposed to NO (˜0.5 equiv relative to active sites) with and without added benzoate or 4-FB are shown in Figure 3.7A. In the absence of substrate, there is a large change in the intensity and shape of the optical absorption spectrum across the visible region, but a much smaller change in intensity and little change in spectral line shape occur in the presence of either substrate. The cause of this difference is revealed in EPR spectra (Figure 3.7A, inset) of identical samples. When NO was added to the reduced enzyme in

the absence of substrate, the rhombic S = 1/2 EPR spectrum of the reduced Rieske cluster (g-values 2.01, 1.91, and 1.76)[7] was attenuated and a new species formed with spectral characteristics (g = 2.04) consistent with dinitrosyl iron complexes previously reported from reactions of biological Rieske clusters with NO.[63] When 4-FB was present, the predicted S = 3/2 spectrum of a mononuclear Fe(III)–NO^- adduct appears without alteration of intensity or line shape of Figure 3.7, inset). This demonstrates that when substrate is present NO binds preferentially to the mononuclear iron site, causing a broad increase in absorbance without significant change in the spectral line shape of the intense chromophore of the Rieske cluster.

Fig. 3.7 Optical Spectra Comparison with NO Binding to BZDO With and Without Benzoate

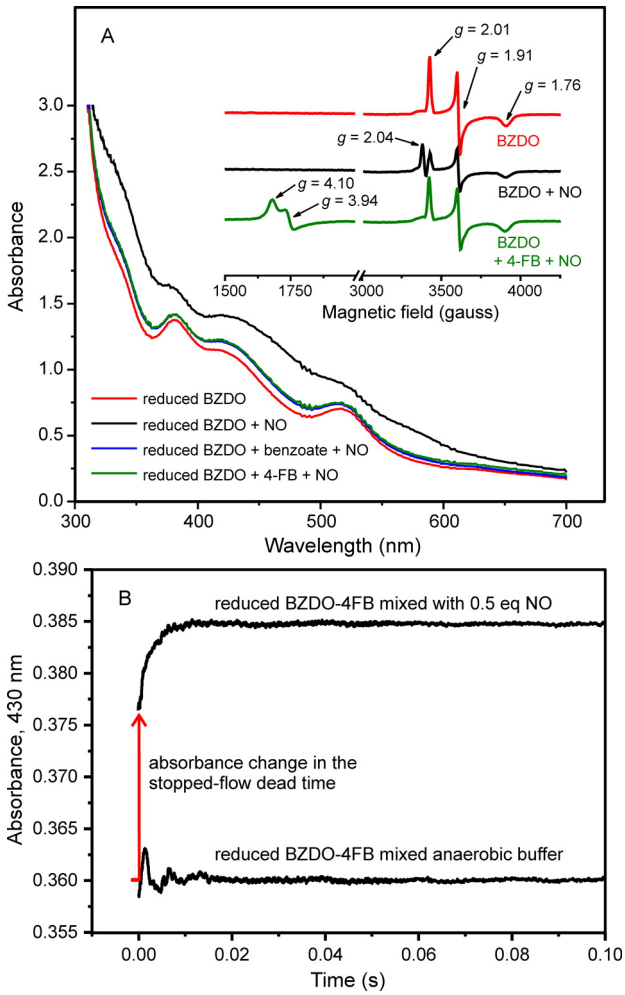

NO binds rapidly to the mononuclear Fe(II) in the substrate complex. (A) The optical spectra of reduced BZDO (250 µM) with or without benzoate (50 mM) or 4-FB (50 mM) are shown 15 min after the addition of NO (˜0.5 equiv relative to BZDO sites). In the absence of substrate, the large change in electronic absorption is caused by NO binding to the Rieske cluster, as can be observed by the attenuation of the S = ½ (g = 2.01, 1.91, and 1.76) EPR signal (inset) from the reduced Rieske cluster and formation of a new signal at g = 2.04. In the presence of benzoate or 4-FB, the NO adduct of the mononuclear iron is formed, as shown by the appearance of the characteristic S = ³/₂ (g = 4.10 and 3.94) EPR signal. Conditions: microwave power, 0.2 mW; temperature, 20 K; microwave frequency, 9.64 GHz. (B) A solution of reduced BZDO (200 µM) and 4-FB (1 mM) was mixed 1:1 in a stopped-flow instrument with anaerobic reaction buffer or anaerobic buffer containing NO (˜0.5 equiv relative to BZDO). Formation of the Fe(III)–NO^- adduct was monitored by the increase in absorption at 430 nm. The same experiment using benzoate in place of 4-FB gave indistinguishable results.

The optical changes observed upon binding of substoichiometric NO exclusively to the mononuclear Fe site in the presence of benzoate or 4-FB provides, in principle, a method to measure the rate constants for the binding reaction of NO, and by analogy O_2, to the metal. When substoichiometric NO was rapidly mixed with solutions of reduced BZDO and benzoate or 4-FB (Figure 3.7B), the change in absorbance occurred primarily in the dead time of the stopped-flow instrument (pseudo-first-order rate constant $\geq 600 s^{-1}$). These results show that NO, and presumably O_2, in the presence of substrates binds with a much larger pseudo-first-order rate constant than the rate constant for the true rate-limiting step prior to the Rieske oxidation reaction.

The Rate Constant for the Rate-Limiting Step Correlates with the Computed Atomic Charge at the Site of Attack on Substrate An alternative explanation for the difference in single-turnover rates of benzoate and the fluorobenzoates is that the electronegative fluorine aromatic substituents deactivate the substrates with respect to electrophilic attack on the aromatic ring. If this hypothesis is true, then a relationship should exist that correlates the electronic changes within the fluorobenzoates listed in Table 3.1 with the rate constants for Rieske cluster oxidation. As shown in Figure S3, this system is not described well by a Hammett σ plot. However, Hammett analysis is more typically successful for reactions occurring at benzylic positions than at aromatic ring centers themselves. A more direct approach to this analysis was adopted by calculating the partial atomic charge specifically at carbons 1 (the ipso carbon) and 2 for benzoate and the fluorobenzoates and then comparing this value to RRT-1 under saturating conditions for each substrate. While there is no trend associated with the CM5 partial charge for carbon 1 (neither is any trend apparent when correlating rates against computed frontier orbital energies), a linear relationship was observed between the observed rates and the CM5 partial group charge at carbon 2 (Figure 3.8), indicating that as electron density is removed from

carbon 2 the rate of electron transfer from the Rieske cluster decreases proportionally.[ii] The suggestion that the C(2)–H group is the site of initial reaction is supported by structural studies of NBDO, which is similar to BZDO in structure, substrate, and chemistry.[14] In NBDO, substrate carbon 2 is positioned closer to the mononuclear Fe than carbon 1 and is thus the likely site of initial attack of the activated oxygen species. This result is consistent with the hypothesis that the decreased rate of turnover with the fluorobenzoates is caused by a change in electron density at the site of initial substrate oxidation.

Fig. 3.8 Relationship Between ln k_{forward} and Calculated Partial Atomic Charge on C(2)–H

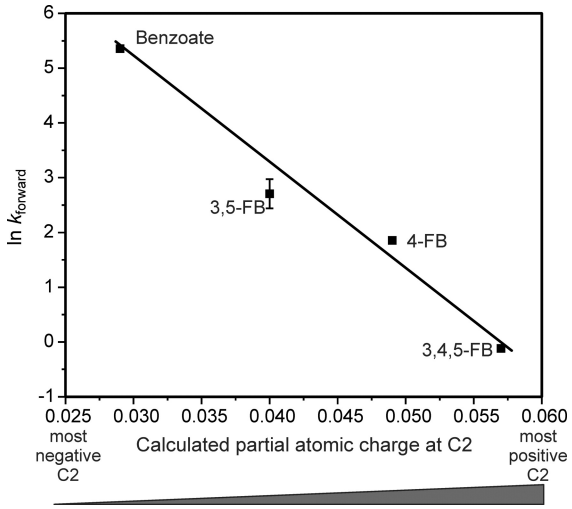

Logarithm of the rate of Rieske cluster oxidation is proportional to the calculated partial group charge at C(2)–H of the substrates tested. A linear trend is observed, showing RRT-1 decreases as the electron density at the C(2)–H group decreases.

[ii] The good correlation illustrated in Figure 3.8 is independent of whether the C(2)–H charges are computed for the conjugate acid (proximally or distally oriented) or base forms of the benzoates (R^2 values of 0.992 or higher), but the correlation is sensitive to whether the charges are computed in the gas phase or including solvation effects. The correlation is significantly improved when using solvated values, as might be expected given the condensed phase nature of the reaction.

3.1.4 Discussion

The results presented here show that the rate-determining step of product formation in the active site of BZDO occurs after substrate and O_2 binding but before transfer of an electron from the Rieske cluster to the mononuclear iron site. This finding contradicts all previous mechanistic theory for RDDs.[7,52,55,64,65] In these earlier studies, it was proposed that the reactive species is an Fe(III)–(H)peroxo adduct (or the derivative HO–Fe(V)═O), which requires transfer of a Rieske electron prior to its formation. Our finding implies a new reactive species for RDDs and differentiates the potential mechanism from those proposed for other NAD(P)H-linked oxygenases such as cytochrome P450 and MMO.[28,30,66–68] These aspects of RDD catalysis are discussed here.

Significance of Product Forming in Only One Step of the Rieske Cluster Oxidation Process A long-standing mystery in the study of BZDO is the cause of the multiphase Rieske cluster oxidation observed during single turnover.[16] This phenomenon has also been reported for other RDDs such as phthalate and anthranilate dioxygenases.[18,69] Several hypotheses were proposed in these studies to account for the multiphase oxidation, including (anti)cooperativity between the subunits of the enzymes, asymmetry caused by partially occupied metal sites, and multistep sequential reactions. The finding here that only the RRT and amplitude of the fastest phase correlate with the rate constant and overall yield of product formation during a single turnover argues against multistep sequential reactions and subunit cooperativity. Rather, the data strongly imply that the Rieske cluster can oxidize in multiple, independent, one-step processes, only one of which is relevant to product formation. It is this insight that allows the evaluation of the steps in substrate binding, oxygen activation, and product formation described here.

Despite the observation that product is formed in only one of two or more independent

Rieske oxidation reactions, it is true that the rate constants for some of the nonproduct forming reactions depend on both the type and concentration of substrate present. This implies substrate participation in each process and, consequently, a role for the mononuclear iron center where the substrate binds. The most straightforward explanation for this observation is that in each reaction an Fe–oxy species of some sort interacts with substrate to trigger the intersubunit electron transfer. For the slower, non-product-forming processes, the reaction apparently does not carry through to cis-diol formation. Indeed, after a single turnover of BZDO, all of the Rieske cluster and mononuclear iron is oxidized despite the less than stoichiometric product yield.[16] This finding may be associated with release of H_2O_2 or another reduced oxygen species, as has been previously reported for some RDD systems.[16,70,71] We have previously shown that BZDO can act as an effective catalase.[34,64] Consequently, direct observation of H_2O_2 release during the non-product-forming oxidation reactions of BZDO has not been verified.

Nature of the Reactive Species The most plausible initial activated oxygen species after formation of an Fe(II)–O_2 complex is an Fe(III)–superoxo (Fe(III)–$O_2^{\bullet--}$) complex. Regulation in BZDO and the RDD family prevents such a complex from forming in the absence of substrate and a reduced Rieske cluster.[7,52] This regulation appears to have at least two aspects. First, spectroscopic studies suggest that substrate binding may facilitate release of solvent, blocking the potential O_2 binding site.[9] Second, spectroscopic and crystallographic studies suggest that reduction of the Rieske cluster may shift the mononuclear iron slightly relative to substrate to create space for O_2 to bind.[9,15,21–23] We propose that the shifts in active site structure may have an additional function, as described below.

The reactivity of the Fe(III)–superoxo species with an aromatic ring has not been fully explored, but there are indications that some types of reactions are possible. For example, we and others have proposed that a metal superoxo species can add to a catechol ring to

form an alkyl peroxo intermediate in the mechanism of extradiol ring cleaving dioxygenases (Figure 3.9A).[72] In this case, we also proposed that the reaction is promoted by electron transfer from the catechol to the iron so that the iron and catechol have ferrous and radical character, respectively.[73] This, in turn, promotes recombination of the oxygen and substrate radicals to form the alkylperoxo intermediate. In the case of isopenicillin N-synthase, we and others have proposed that an Fe(III)–superoxo is capable of hydrogen atom abstraction from the β-carbon of the cysteinyl moiety of the δ-(L-α-aminoadipoyl)-L-cysteinyl-D-valine (ACV) substrate.[43–45,74] The energy for such a reaction would be similar to that required for electron abstraction from an aromatic ring. Here again, the Fe(III)–superoxo species can be considered to be somewhat activated by a shift in electron density from the cysteinyl sulfur of ACV bound directly to the iron. One particularly relevant example is found in the tryptophan 2,3-dioxygenase (TDO) and indolamine 2,3-dioxygenase (IDO) systems, where electron abstraction from aromatic systems by Fe(II)–O_2or Fe(III)–superoxo has been computationally and experimentally explored (Figure 3.9B).[75–77] For this enzyme class, the iron–oxy system is not significantly activated, but initial attack involving one- or two-electron withdrawal from the heterocyclic indole ring followed by recombination to form an alkylperoxo intermediate is predicted as a first step. Downstream reactions result in dioxygen insertion and indole ring cleavage. Radical reactions with aromatics have also been explored both experimentally and computationally using a diradical form of phthaloyl peroxide in which one radical moiety is proposed to attack an unactivated aryl moiety to form an ester-linked aryl radical with only a moderate activation barrier (Figure 3.9C).[78]

Fig. 3.9 Key Steps in Reactions Mechanisms Invoking Reaction Iron–Superoxide Intermediates[a]

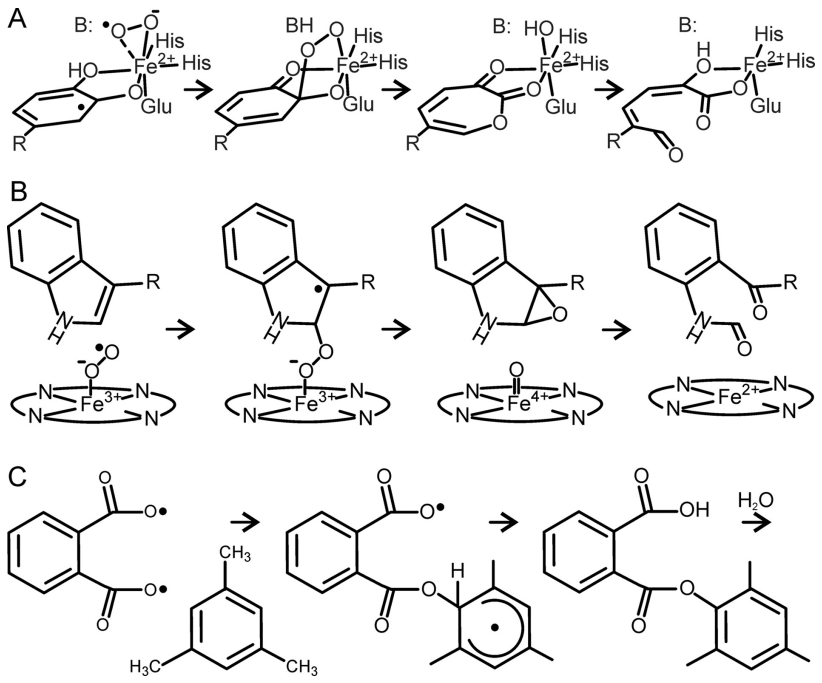

[a](A) Extradiol dioxygenase,[72] (B) tryptophan 2,3-dioxygenase,[75–77] (C) phthaloyl peroxide reaction with unactivated aromatic compound.[78]

One route to substrate hydroxylation by BZDO is illustrated in Figure 3.10. The current results show that substrate and O_2 binding occur rapidly to BZDO when both the mononuclear iron and Rieske cluster are reduced. Direct radical attack of a potential resulting Fe(III)–superoxo intermediate on the aromatic substrate would yield an Fe(III)–peroxo-aryl radical analogous to the Fe(III)–peroxo-imidazole radical proposed as a feasible route for the TDO/IDO systems (Figure 3.9B).[75–77] In the latter system, the subsequent steps may result in the formation of a substrate epoxide with coincident formation of an Fe(IV)=O at the level of Compound II. Reaction of the high-valent oxo species with the epoxide or the carbocation formed upon epoxide ring opening would result in the dioxygenation reaction and ring opening. In contrast, the BZDO system is able to avoid ring cleavage. This can

be achieved by controlling the source of the two electrons required for this phase of the reaction. Rather than utilizing two electrons from the sessile bond (as in the TDO/IDO case), our past results have shown that BZDO uses one from the iron and one from the Rieske cluster.[7,52] We propose that the high potential Fe(III) formed concurrent with the formation of the putative Fe(III)–peroxo-aryl radical intermediate allows the transfer of an electron from the Rieske cluster. The additional electron would promote homolytic O–O bond cleavage with formation of an intermediate ring epoxide and an Fe(III)–O^{-}. Opening of the epoxide would yield a carbocation that could abstract the hydroxide anion from the iron to yield the cis-diol product without ring opening. In this scenario, the Fe(III)–superoxo species would have to have sufficient Fe(II) character to prevent electron transfer from the Rieske prior to rate-limiting attack on the substrate. Other mechanistic scenarios, such as heterolytic cleavage of the O–O bond with formation of a high-valent iron–oxo intermediate subsequent to formation of the Fe(III)–peroxo-aryl radical species, are also possible.

Fig. 3.10 Reaction Cycle for Benzoate 1,2-Dioxygenase Emerging from the Current Study[a]

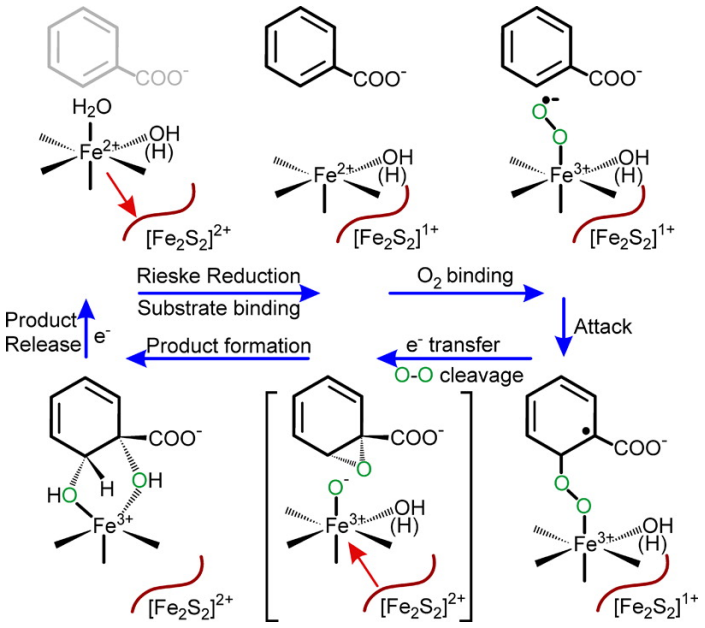

[a]Red arrows represent the direction of a conformational shift of the mononuclear iron observed spectroscopically and in crystal structures. There are several possibilities for the cis-diol forming reactions following electron transfer from the Rieske cluster, only one of which is shown. An electron from an external source is required to allow product release.

The initial reaction of Fe(III)–superoxo with the aromatic substrate shown in Figure 3.10 would depend strongly on susceptibility of the aromatic ring to oxidation, specifically at the position of attack. The current results show that the presence of electron-withdrawing fluorine substituents on the ring deactivate the C(2) position for such an attack. Moreover, the computational evaluation of the effect of the numbers and positions of fluorine atoms on the charge density at the presumed position of attack, C(2), are consistent with this proposed mechanism.

The crystal structure of BZDO has not been reported, making it impossible to explore theoretically any actual reaction coordinate with a requisite level of confidence, but structures of several other RDDs and some intermediates are known. This includes structures of the

putative Fe(III)–(H)peroxo intermediate previously assumed by many to be the species that initially attacks the substrate.[13,15] In all such structures, the distance between the mononuclear iron and the substrate carbon closest to the iron is in the range of 4.2–4.6 Å. This is the expected distance for formation of an aryl-peroxo intermediate. After O–O bond cleavage and electron transfer from the Rieske cluster, the resulting Fe(III)–O^- would be approximately 2.5–3 Å from the nearest substrate carbon. This is not an unreasonable distance for a nucleophilic attack of a Fe(III)–O^- on aryl cation, but the reaction may be further promoted by the return of the Rieske cluster to the oxidized state. Structural studies of 2-oxoquinoline 8-monooxygenase and CarDO show that oxidation of the Rieske cluster forces the mononuclear iron to move approximately 0.5 Å toward the substrate.[15,21] Such a movement would bring the Fe(III)–O^- and aryl cation in closer proximity and may trigger rapid irreversible completion of the reaction once the electron from the Rieske cluster has been transferred. This reaction would make the rate-limiting formation of the Fe(III)–peroxo-aryl intermediate appear to be irreversible, as we observe, even if it was, in fact, a reversible process.

3.1.5 Conclusions

Our previous studies have shown that product formation during a single turnover in RDDs results in one-electron oxidation of each metal center.[7,52] This stoichiometry together with crystal structures of CarDO and NDO showing a side-on bound peroxo intermediate and our demonstration that the enzymes can use a peroxide shunt to slowly drive catalysis led to the hypothesis that an Fe(III)–(H)peroxo (or HO–Fe(V)═O) species is the reactive species in RDDs.[13,15,34,64] This hypothesis was supported by computations as well as model studies.[36,55,79–81] However, the observation here that the apparent rate of the electron transfer from the Rieske cluster required to form the peroxo intermediate depends on the

number and position of fluorines introduced into the substrate ring strongly suggests that there is a reaction with substrate prior to electron transfer. The dependence of the rate of this reaction on the electron density at the closest substrate carbon to the iron is consistent with the attacking species being an electrophilic Fe(III)–superoxo. The result of this attack would be an Fe(III)–peroxo-aryl-radical intermediate. While it is possible that the O–O bond cleavage occurs at this stage, we believe that it is unlikely because there is no detectable reaction of any type when only the mononuclear iron is reduced. However, it may also be that the conformation imposed by the oxidized Rieske cluster does not allow substrate and O_2 access to the active site to allow the reaction to initiate. Oxygen bond cleavage after electron transfer from the Rieske cluster would force the reaction onward irreversibly to product formation.

There is little doubt that RDD enzymes can stabilize a reactive Fe(III)–peroxo species, as demonstrated in both solution and crystallographic studies.[13,15,35] However, the current study suggests that this species is not accessed during normal turnover due to either kinetic or steric constraints. When the intermediate is formed during a single-turnover peroxide shunt reaction of fully oxidized BZDO, the product formation reaction occurs on a minute rather than a millisecond time scale.[34]

NDO and other RDDs can catalyze both dioxygenase and adventitious monooxygenase reactions.[82] Use of a radical trap/clock molecule as a monooxygenase substrate for NDO unequivocally demonstrated that a radical intermediate was formed.[83] A radical is unlikely to arise from the attack of an Fe(III)–peroxo intermediate, but it might derive from attack by either an Fe(III)–superoxo species proposed here or an electrophilic HO–Fe(V)═O species hypothesized previously.[83] Indeed, both types of chemistry might occur in the versatile RDD family, with the mechanism determined by the reaction type, the oxygen species supplied, the substrate, and the kinetics of individual steps along the reaction coordinate.

3.1.6 Associated Content

Additional experimental procedures and results. Figures S1: Product analysis of single-turnover reactions. Figure S2: Substrate and O_2 concentration dependence of RRT-1. Figure S3: Hammett plot for the reaction using the substrates. The Supporting Information is available free of charge on the ACS Publications website at DOI: 10.1021/acs.biochem.5b00573.

3.1.7 Notes

The authors declare no competing financial interest.

3.1.8 Acknowledgments

We thank Simon E. Lewis for the gift of the *Ralstonia eutrophus* strain B9 and Jung-Kul Lee for the gift of the pACYC-*isc* plasmid. We thank Johannes Klein for assistance in NMR analysis.

References

[1] Barry, S.; Challis, G. L. *ACS Catal.* **2013**, *3*, 2362–2370.

[2] Gibson, D. T.; Parales, R. E. *Curr. Opin. Biotechnol.* **2000**, *11*, 236–243.

[3] Aukema, K. G.; Kasinkas, L.; Asan, A.; Wackett, L. P. *Appl. Environ. Microbiol.* **2014**, *80*, 4968–4976.

[4] Lewis, S. E. *Chem. Commun.* **2014**, *50*, 2821–2830.

[5] Jenkins, G. N.; Ribbons, D. W.; Widdowson, D. A.; Slawin, A. M. Z.; Williams, D. J. *J. Chem. Soc., Perkin Trans. 1* **1995**, 2647–2655.

[6] Myers, A. G.; Siegel, D. R.; Buzard, D. J.; Charest, M. G. *Org. Lett.* **2001**, *3*, 2923–2926.

[7] Wolfe, M. D.; Altier, D. J.; Stubna, A.; Popescu, C. V. a. M. E.; D., L. J. *Biochemistry* **2002**, *41*, 9611–9626.

[8] Koehntop, K. D.; Emerson, J. P.; Que, L. *JBIC, J. Biol. Inorg. Chem.* **2005**, *10*, 87–93.

[9] Ohta, T.; Chakrabarty, S.; Lipscomb, J. D.; Solomon, E. I. *J. Am. Chem. Soc.* **2008**, *130*, 1601–1610.

[10] Ferraro, D. J.; Gakhar, L.; Ramaswamy, S. *Biochem. Biophys. Res. Commun.* **2005**, *338*, 175–190.

[11] Kauppi, B.; Lee, K.; Carredano, E.; Parales, R. E.; Gibson, D. T.; Eklund, H.; Ramaswamy, S. *Structure* **1998**, *6*, 571–586.

[12] Carredano, E.; Karlsson, A.; Kauppi, B.; Choudhury, D.; Parales, R. E.; Parales, J. V.; Lee, K.; Gibson, D. T.; Eklund, H.; Ramaswamy, S. *J. Mol. Biol.* **2000**, *296*, 701–712.

[13] Karlsson, A.; Parales, J. V.; Parales, R. E.; Gibson, D. T.; Eklund, H.; Ramaswamy, S. *Science* **2003**, *299*, 1039–1042.

[14] Friemann, R.; Ivkovic-Jensen, M. M.; Lessner, D. J.; Yu, D. T., C.-L. Gibson; Parales, R. E.; Eklund, H.; Ramaswamy, S. *J. Mol. Biol.* **2005**, *348*, 1139–1151.

[15] Ashikawa, Y.; Fujimoto, Z.; Usami, Y.; Inoue, K.; Noguchi, H.; Yamane, H.; Nojiri, H. *BMC Struct. Biol.* **2012**, *12*, 15.

[16] Lee, K. *J. Bacteriol.* **1999**, *181*, 2719–2725.

[17] Parales, R. E.; Parales, J. V.; Gibson, D. T. *J. Bacteriol.* **1999**, *181*, 1831–1837.

[18] Beharry, Z. M.; Eby, D. M.; Coulter, R., E. D. andViswanathan; Neidle, E. L.; Phillips, R. S.; Kurtz, D. M. *Biochemistry* **2003**, *42*, 13625–13636.

[19] Pinto, A.; Tarasev, M.; Ballou, D. P. *Biochemistry* **2006**, *45*, 9032–9041.

[20] Tarasev, M.; Pinto, A.; Kim, D.; Elliott, S. J.; Ballou, D. P. *Biochemistry* **2006**, *45*, 10208–10216.

[21] Martins, B. M.; Svetlitchnaia, T.; Dobbek, H. *Structure* **2005**, *13*, 817–824.

[22] Yang, T.-C.; Wolfe, M. D.; Neibergall, M. B.; Mekmouche, Y.; Lipscomb, J. D.; Hoffman, B. M. *J. Am. Chem. Soc.* **2003**, *125*, 7056–7066.

[23] Yang, T.-C.; Wolfe, M. D.; Neibergall, M. B.; Mekmouche, Y.; Lipscomb, J. D.; Hoffman, B. M. *J. Am. Chem. Soc.* **2003**, *125*, 2034–2035.

[24] Solomon, E. I.; Light, K. M.; Liu, L. V.; Srnec, M.; Wong, S. D. *Acc. Chem. Res.* **2013**, *46*, 2725–2739.

[25] Kovaleva, E. G.; Lipscomb, J. D. *Nat. Chem. Biol.* **2008**, *4*, 186–193.

[26] Dalton, H. *Adv. Appl. Microbiol.* **1980**, *26*, 71–87.

[27] Tyson, C. A.; Lipscomb, J. D.; Gunsalus, I. C. *J. Biol. Chem.* **1972**, *247*, 5777–5784.

[28] Ortiz de Montellano, P. R. *Cytochrome P450: Structure, Mechanism, and Biochemistry*; Plenum Press: New York, 1995.

[29] Zhou, N.-Y.; Al-Dulayymi, J.; Baird, M. S.; Williams, P. A. *J. Bacteriol.* **2002**, *184*, 1547–1555.

[30] Tinberg, C. E.; Lippard, S. J. *Acc. Chem. Res.* **2011**, *44*, 280–288.

[31] Liu, K. E.; Valentine, A. M.; Wang, D. L.; Huynh, B. H.; Edmondson, D. E.; Salifoglou, A.; Lippard, S. J. *J. Am. Chem. Soc.* **1995**, *117*, 10174–10185.

[32] Lee, S. K.; Lipscomb, J. D. *Biochemistry* **1999**, *38*, 4423–4423.

[33] Davydov, R.; Makris, T. M.; Kofman, V.; Werst, D. E.; Sligar, S. G.; Hoffman, B. M. *J. Am. Chem. Soc.* **2001**, *123*, 1403–1415.

[34] Neibergall, M. B.; Stubna, A.; Mekmouche, Y.; Münck, E.; Lipscomb, J. D. *Biochemistry* **2007**, *46*, 8004–8016.

[35] Bassan, A.; Blomberg, M. R. A.; Siegbahn, P. E. M. *JBIC, J. Biol. Inorg. Chem.* **2004**, *9*, 439–452.

[36] Pabis, A.; Geronimo, I.; Paneth, P. *J. Phys. Chem. B* **2014**, *118*, 3245–3256.

[37] Chen, K.; Costas, M.; Kim, J.; Tipton, A. K.; Que, L. *J. Am. Chem. Soc.* **2002**, *124*, 3026–3035.

[38] Prat, I.; Mathieson, J. S.; Guell, M.; Ribas, X.; Luis, J. M.; Cronin, L.; Costas, M. *Nat. Chem.* **2011**, *3*, 788–793.

[39] Oloo, W. N.; Fielding, A. J.; Que, L. *J. Am. Chem. Soc.* **2013**, *135*, 6438–6441.

[40] Liu, L. V.; Hong, S.; Cho, J.; Nam, W.; Solomon, E. I. *J. Am. Chem. Soc.* **2013**, *135*, 3286–3299.

[41] Mbughuni, M. M.; Chakrabarti, M.; Hayden, J. A.; Meier, K. K.; Dalluge, J. J.; Hendrich, M. P.; Münck, E.; Lipscomb, J. D. *Biochemistry* **2011**, *50*, 10262–10274.

[42] Mbughuni, M. M.; Chakrabarti, M.; Hayden, J. A.; Bominaar, E. L.; Hendrich, E., M. P. andMünck; Lipscomb, J. D. *Proc. Natl. Acad. Sci. U. S. A.* **2010**, *107*, 16788–16793.

[43] Brown, C. D.; Neidig, M. L.; Neibergall, M. B.; Lipscomb, J. D.; Solomon, E. I. *J. Am. Chem. Soc.* **2007**, *129*, 7427–7438.

[44] van der Donk, W. A.; Krebs, C.; Bollinger, J. M. *Curr. Opin. Struct. Biol.* **2010**, *20*, 673–683.

[45] Bollinger, J. M.; Krebs, C. *Curr. Opin. Chem. Biol.* **2007**, *11*, 151–158.

[46] Zhao, Y.; Truhlar, D. G. *Theor. Chem. Acc.* **2008**, *120*, 215–241.

[47] Hehre, W. J.; Random, L.; Schleyer, P. v. R.; Pople, J. A. *Ab Initio Molecular Orbital Theory*; Wiley: New York, 1986.

[48] Marenich, A. V.; Cramer, C. J.; Truhlar, D. G. *J. Phys. Chem. B* **2009**, *113*, 6378–6396.

[49] Marenich, A. V.; Jerome, S. V.; Cramer, C. J.; Truhlar, D. G. *J. Chem. Theory Comput.* **2012**, *8*, 527–541.

[50] Frisch, M. J. et al. Gaussian 09, Revision C.01. 2010.

[51] Marenich, A. V.; Cramer, C. J.; Truhlar, D. G. CM5PAC: University of Minnesota, Minneapolis, MN, 2011.

[52] Wolfe, M. D.; Parales, J. V.; Gibson, D. T.; Lipscomb, J. D. *J. Biol. Chem.* **2001**, *276*, 1945–1953.

[53] Bernhardt, F. H.; Ruf, H. H.; Ehrig, H. *FEBS Lett.* **1974**, *43*, 53–55.

[54] Twilfer, H.; Bernhardt, F. H.; Gersonde, K. *Eur. J. Biochem.* **1985**, *147*, 171–176.

[55] Bassan, A.; Blomberg, M. R. A.; Borowski, T.; Siegbahn, P. E. M. *J. Phys. Chem. B* **2004**, *108*, 13031–13041.

[56] Liu, Y.; Nesheim, J. C.; Lee, S.-K.; Lipscomb, J. D. *J. Biol. Chem.* **1995**, *270*, 24662–24665.

[57] DuBois, J. L.; Klinman, J. P. *Biochemistry* **2005**, *44*, 11381–11388.

[58] Orville, A. M.; Lipscomb, J. D.; Ohlendorf, D. H. *Biochemistry* **1997**, *36*, 10052–10066.

[59] Karlsson, A.; Parales, J. V.; Parales, R. E.; Gibson, D. T.; Eklund, H.; Ramaswamy, S. *JBIC, J. Biol. Inorg. Chem.* **2005**, *10*, 483–489.

[60] Orville, A. M.; Lipscomb, J. D. *J. Biol. Chem.* **1993**, *268*, 8596–8607.

[61] Arciero, D. M.; Lipscomb, J. D.; Huynh, B. H.; Kent, T. A.; Münck, E. *J. Biol. Chem.* **1983**, *258*, 14981–14991.

[62] Schenk, G.; Pau, M. Y. M.; Solomon, E. I. *J. Am. Chem. Soc.* **2004**, *126*, 505–515.

[63] Tinberg, C. E.; Tonzetich, Z. J.; Wang, H.; Do, L. H.; Yoda, Y.; Cramer, S. P.; Lippard, S. J. *J. Am. Chem. Soc.* **2010**, *132*, 18168.

[64] Wolfe, M. D.; Lipscomb, J. D. *J. Biol. Chem.* **2003**, *278*, 829–835.

[65] Bugg, T. D. H.; Ramaswamy, S. *Curr. Opin. Chem. Biol.* **2008**, *12*, 134–140.

[66] Shaik, S.; Cohen, S.; Wang, Y.; Chen, H.; Kumar, D.; Thiel, W. *Chem. Rev.* **2010**, *110*, 949–1017.

[67] Wallar, B. J.; Lipscomb, J. D. *Chem. Rev.* **1996**, *96*, 2625–2657.

[68] Kovaleva, E. G.; Neibergall, M. B.; Chakrabarty, S.; Lipscomb, J. D. *Acc. Chem. Res.* **2007**, *40*, 475–483.

[69] Tarasev, M.; Rhames, F.; Ballou, D. P. *Biochemistry* **2004**, *43*, 12799–12808.

[70] Twilfer, H.; Sandfort, G.; Bernhardt, F.-H. *Eur. J. Biochem.* **2000**, *267*, 5926–5934.

[71] Perez-Pantoja, D.; Nikel, P. I.; Chavarria, M.; de Lorenzo, V. *PLoS Genet.* **2013**, *9*, e1003764.

[72] Lipscomb, J. D. *Curr. Opin. Struct. Biol.* **2008**, *18*, 644–649.

[73] Kovaleva, E. G.; Lipscomb, J. D. *Science* **2007**, *316*, 453–457.

[74] Lundberg, M.; Siegbahn, P. E. M.; Morokuma, K. *Biochemistry* **2008**, *47*, 1031–1042.

[75] Capece, L.; Lewis-Ballester, A.; Yeh, S.-R.; Estrin, D. A.; Marti, M. A. *J. Phys. Chem. B* **2012**, *116*, 1401–1413.

[76] Chung, L. W.; Li, X.; Sugimoto, H.; Shiro, Y.; Morokuma, K. *J. Am. Chem. Soc.* **2010**, *132*, 11993–12005.

[77] Basran, J.; Efimov, I.; Chauhan, N.; Thackray, S. J.; Krupa, J. L.; Eaton, G.; Griffith, G. A.; Mowat, C. G.; Handa, S.; Raven, E. L. *J. Am. Chem. Soc.* **2011**, *133*, 16251.

[78] Yuan, C.; Liang, Y.; Hernandez, T.; Berriochoa, A.; Houk, K. N.; Siegel, D. *Nature* **2013**, *499*, 192–196.

[79] Das, P.; Que, L. *Inorg. Chem.* **2010**, *49*, 9479–9485.

[80] Lyakin, O. Y.; Prat, I.; Bryliakov, K. P.; Costas, M.; Talsi, E. P. *Catal. Commun.* **2012**, *29*, 105–108.

[81] Gomez, L.; Canta, M.; Font, D.; Prat, I.; Ribas, X.; Costas, M. *J. Org. Chem.* **2013**, *78*, 1421–1433.

[82] Gibson, D. T.; Resnick, S. M.; Lee, K.; Brand, J. M.; Torok, D. S.; Wackett, L. P.; Schocken, M. J.; Haigler, B. E. *J. Bacteriol.* **1995**, *177*, 2615–2621.

[83] Chakrabarty, S.; Austin, R. N.; Deng, D.; Groves, J. T.; Lipscomb, J. D. *J. Am. Chem. Soc.* **2007**, *129*, 3514–3515.

4. Interrogating Reaction Mechanisms for Complex Organic Reactions

4.1 Mechanism of the Intramolecular Hexadehydro-Diels–Alder Reaction

4.1.1 Introduction

The hexadehydro-Diels–Alder (HDDA) cascade (Figure 4.1a) involves an initial rate-limiting, thermal cycloisomerization of a triyne to a benzyne intermediate[1–3] followed by a trapping reaction. The overall process has been shown to be quite general and serves as a platform for the discovery of new reaction processes.[4,5] Coupled cluster calculations including single, double, and perturbatively estimated triple excitations (CCSD(T)) indicate that *o*-benzyne is approximately 50 kcal/mol more stable than 1,3-butadiyne and ethyne.[6] Similar exergonicities have been computed for the free energy changes that attend intramolecular HDDA processes.[7] Like the classic Diels-Alder reaction between a diene and dienophile, for which extensive mechanistic interrogation has been undertaken, the HDDA could potentially proceed through one of two pathways (Figure 4.1b). In a concerted process (magenta arrows) the a–b and c–d bonds form simultaneously, which is to say that no intermediate intervenes prior to product formation, irrespective of the degree of synchronicity in the formation of the two bonds. Alternatively, in a stepwise pathway, the proximal bond a–b is formed first (blue arrows) to create a diradical intermediate, which then ring-closes by formation of the distal bond c–d (green arrows); bond formation in the reverse order (c-to-d then a-to-b) is formally plausible, but clearly unlikely (*vide infra*). At the coupled cluster level of theory, the concerted and stepwise pathways for the parent HDDA reaction between ethyne and

butadiyne are predicted to have activation barriers within 0.5 kcal/mol of one another;[6] however, as discussed in this paper, there is reason to believe that this level of theory may underestimate the stability of diradical transition-state (TS) structures. Houk and co-workers have recently reported broken-symmetry density functional theory (DFT) studies for a hypothetical series of bimolecular HDDA reactions between 1,3-butadiyne and four different diynophiles.[8] In each case, including the parent reaction, they identified a preference for a stepwise, diradical pathway over the concerted event. They found in addition that the barriers for ring closure of the generated diradical intermediate, to complete the generation of the *o*-benzyne species, were quite low (in the range of 4–7 kcal/mol). Larini, Perrin, and coworkers have recently reported a DFT examination of an intramolecular HDDA reaction (of a tetrayne substrate) in which they also observed a preference for a stepwise, diradical pathway.[9]

Fig. 4.1 General Reaction and Proposed Mechanisms for the Intramolecular Hexadehydro-Diels–Alder

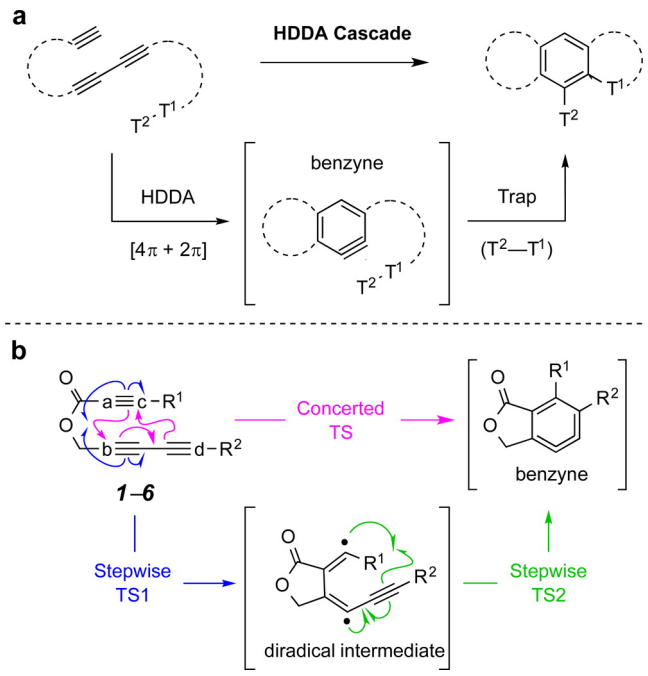

(a) Intramolecular hexadehydro-Diels–Alder (HDDA) reaction of a generic tethered triyne substrate, followed by intramolecular trapping. (b) Concerted vs stepwise mechanistic alternatives. See Table 4.1 for substituents defining for **1**–**6**.

To gain further mechanistic insight into the details of HDDA cycloisomerizations, which to date have only been observed in intramolecular settings, we have carried out additional experimental and computational studies reported here. In particular, the energies of activation of a new series of six triyne substrates have been determined experimentally and evaluated computationally using a variety of DFT and wave function theory methods. On this specific test set we address the questions of (i) is the HDDA reaction better described as a concerted or a stepwise diradical pathway? and (ii) to what degree does diradical character along the stepwise reaction pathway affect the applicability of theoretical methods based on single-determinantal references? We then extend our theoretical attention to additional HDDA substrates for which kinetic data are available and show that broken-symmetry

DFT calculations agree with multireference wave function theory calculations. This helps in distinguishing between a reaction pathway that is fully stepwise vs one that is concerted but so asynchronous as to be effectively stepwise, albeit with an intermediate on the potential energy surface that is not predicted to have a bound vibrational state.

4.1.2 Results and Discussion

Theory/Computational Models Gas-phase molecular structures were fully optimized at the M06-2X level[10] of density functional theory employing the 6-311+G(d,p) basis set.[11] This level of theory has been documented to give very good agreement with experiment for organic structures.[12] The natures of all stationary points, either minima or TS structures, were confirmed by analytic computation of vibrational frequencies, which were also employed for the calculation of molecular partition functions and thermal contributions to molecular enthalpies and free energies.

"Best" DFT electronic energies were computed using the B3LYP functional[13–16] combined with the 6-311+G(d,p) basis set and a D3 dispersion correction[17] damped according to the scheme of Becke and Johnson.[18] In addition, *o*-dichlorobenzene solvation effects were included in these single-point calculations using the SMD solvation model.[19] This level of theory, denoted in full as SMD(*o*-dichlorobenzene)/B3LYP-D3BJ/6-311+G-(d,p)//M06-2X/6-311+G(d,p), will be referred to simply as B3LYP-D3BJ hereafter. In select instances, geometries and energetics were also computed using other levels of density functional theory, including M06-L, M06, M06-D3, M06-2X, M11-L, M11, and B3LYP; full details are provided either below or in the Supporting Information.

Importantly, while restricted Kohn-Sham determinants for relevant singlet electronic (ground) states were found to be stable to symmetry breaking for all reactants, this was not

the case for any of the concerted TS structures that were located. Unrestricted (broken-symmetry) determinants were optimized for TS structures, and intermediates along stepwise cyclization pathways and singlet energies ^{1}E were determined from spin purification of the mixed-spin-state energies according to refs 20 and 21 where the "BS" and "3" superscripts in Eq. 4.1 refer to broken-symmetry and triplet Kohn-Sham determinants, respectively, and $\langle S^2 \rangle$ is the expectation value of the total spin operator.

$$^1\mathrm{E} = \frac{2 \cdot {}^{\mathrm{BS}}\mathrm{E} - {}^{\mathrm{BS}}\langle S^2 \rangle \cdot {}^3\mathrm{E}}{2 - {}^{\mathrm{BS}}\langle S^2 \rangle} \tag{4.1}$$

To address the instability of the restricted Kohn-Sham determinants, we also applied, in select cases, second-order perturbation theory based on complete active space self-consistent field (CASPT2) calculations,[22,23] taking for the active space the 12 electrons in 12 orbitals associated with the π and π* orbitals for the three triple bonds and using the triple-ζ ANO-RCC basis set of Roos et al.[24] An IPEA shift of 0.25 au (the default value) was applied in the CASPT2 calculations to define the zeroth-order Hamiltonian.[25] We also examined the CBS-QB3 level of theory[26] in certain instances. This composite electronic structure method assembles molecular energies from a variety of levels with the most complete being coupled cluster theory including single, double, and perturbatively estimated triple excitations (CCSD(T)); for singlets, however, the default CBS-QB3 procedure is based on a single-determinant reference RHF wave function, and we computed the T1 diagnostic[27] of Lee and Taylor to assess the degree to which this might render the CBS-QB3 level unreliable. In order to apply CBS-QB3 to diradical species, we calculated each of the contributing molecular energies based on a broken-symmetry Hartree-Fock reference.

Density functional enthalpies and free energies were computed from Boltzmann averages over all relevant structures[21] (note that solvation free energies from continuum solvent calculations are *not* readily separable into enthalpies and entropies, but because we are

interested only in *relative* enthalpies, the assumption that any variation in the solvation enthalpies is similar to that in the solvation free energies seems reasonable, given the overall structurally similar nature of the substrates). Averaging was required only for reactant minima having free rotation about single bonds in the tether joining the reactive 4π and 2π fragments. For these substrates, rotamers placing the triple bonds into proximity with one another (i.e., in a "pre-reactive" conformation) were invariably higher than alternatives with the reactive fragments oriented away from one another. Other averages (e.g., rotameric populations associated with a TBS group) were assumed to cancel in reactant and TS structures.

Mechanistic Analysis At the outset, our thinking was influenced by extensive qualitative observations some of us have made about many HDDA reaction cascades. For example, they are essentially insensitive to the presence or absence of triplet oxygen, light, or good hydrogen-atom donor solvents such as chloroform, observations more compatible with the hypothesis of a concerted reaction mechanism. We therefore designed and prepared a series of substrates to test this possibility. Esters **1**–**6** (Figure 4.1 and Table 4.1) differ substantially in the steric bulk of the trisubstituted silyl substituents on one or both of their terminal alkynes.

Table 4.1 Half-Lives (h) and Relative Rates for HDDA Cyclization of Ester Triynes **1**–**6**

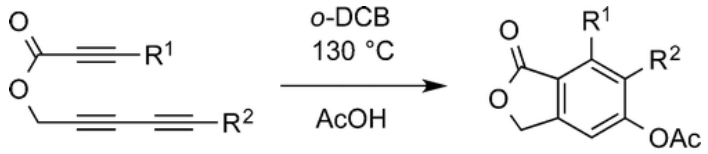

1-6 ***7-12***

triyne substrate	R^1	R^2	$t_{1/2}$, h	k_{rel}	phthalide product
1	H	H	4.5	1.1	**7**
2	H	TMS	2.8	1.8	**8**
3	H	TBS	2.8	1.8	**9**
4	H	$SiPh_3$	2.8	1.8	**10**
5	TMS	H	1.1	4.5	**11**
6	TMS	TMS	5.0	1.0	**12**

We presumed that enhanced bulk would slow the rate of HDDA cyclization, if concerted. The preparation of esters **1**–**6** was straightforward. Each ester was heated in 1,2-dichlorobenzene (*o*-DCB) in the presence of 20–40 equiv of acetic acid, a known and efficient trap of HDDA-generated benzynes. Half-lives were measured by following the conversion to product at various time points via ^{1}H nuclear magnetic resonance (NMR) spectroscopy. Surprisingly, all six substrates exhibited reaction rates within a factor of 4.5 of one another, and the least and most highly substituted variants (i.e., **1** and **6** respectively) cyclized at essentially the same rate (k_{rel} of 1.1). This observation is more consistent with the reaction proceeding through a rate-limiting transition state in which the distal alkyne termini are quite far from one another. Such a situation can be envisioned for either a highly asynchronous concerted process or a stepwise diradical pathway (Figure 4.1b).

We then turned to computational modeling. For each of the educts **1**–**6**, we located multiple conformational minima related as rotamers. In general, "unreactive" conformers (e.g., the *anti* conformer shown at left in Figure 4.2) predominated; specifically, the percentages of *syn*-like "reactive" conformers at the B3LYP-D3BJ//M06-2X level were predicted to be

3, 3, 14, 3, 11 and 28 for **1**–**6**, respectively. Proper enthalpies of reaction must take into account Boltzmann averages over all contributors to the educt population, and this was indeed done as noted in the Theory/Computational Models Section (see page 119).

Fig. 4.2 Fischer Projections and Ball-and-Stick Models of Two Rotameric Minima for **1**

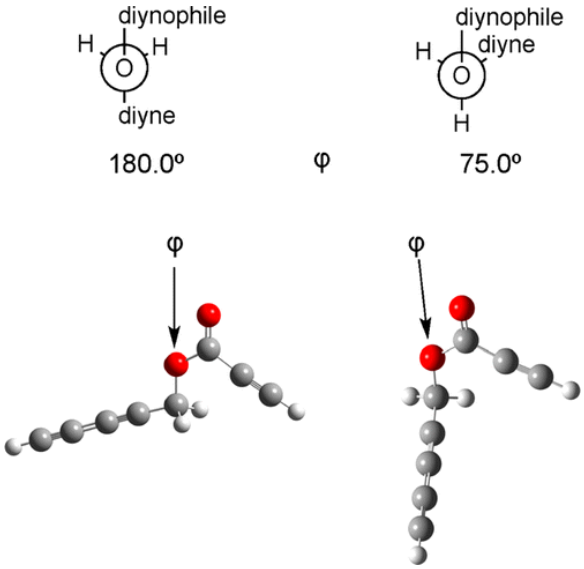

With respect to transition states for a concerted reaction, for substrates **1**–**5** it proved possible to locate TS structures on the singlet surface using a restricted Kohn–Sham formalism (in the case of **6**, such a TS structure could not be located, presumably owing to instability of the restricted determinant, as discussed in more detail below). Perturbing these structures in either direction along the reaction coordinate led either back to educts or forward to *o*-benzyne products; i.e., they are TS structures for concerted HDDA cycloaddition. Consistent with concerted reactivity, the lengths of the two newly forming bonds connecting the termini of the former yne and diyne fragments were reasonably similar, e.g., in the case of **1**, 2.018 Å for the forming bond nearer the ester tether and 2.463 Å for the other (cf. the length difference of ca. 3 Å for the stepwise pathway, below). Comparison (Table 4.2 of the computed activation enthalpies to those derived from experiment, however, does not give a

particularly close match for **1**–**5**. The computed values are all substantially higher than the experimental ones, and the computed values range over 2.7 kcal/mol while the experimental values range over only 1.3 kcal/mol.

Table 4.2 Experimentally Derived and Predicted Concerted and Stepwise Activation Enthalpies (kcal/mol) for **1**–**6**

		$\Delta H^{\ddagger}$			
			Theoretical[a]		
	Triyne	Experiment[b]	Concerted TS	Stepwise TS1	Stepwise TS2[c]
1	H/H	23.7	31.5	25.5	18.1 (–0.8)
2	H/TMS	23.3	30.4	24.8	16.5 (–1.2)
3	H/TBS	23.3	30.3	24.8	16.4 (–1.3)
4	H/$SiPh_3$	23.3	28.8	24.6	*d*
5	TMS/H	22.5	28.9	23.1	17.1 (0.2)
6	TMS/TMS	23.8	*d*	20.9	18.8 (4.8)

[a]Relative to the Boltzmann-averaged enthalpy of the educt. [b]Determined from relative rates and assuming a common Arrhenius *A* value; see Experimental Section (Page 140) for details. [c]Enthalpy in parentheses is relative to the diradical intermediate; a negative value implies an enthalpy *below* that of the intermediate, in spite of a higher potential energy. [d]Not located.

Further assessment of the Kohn-Sham determinants for the concerted TS structures revealed them to be unstable to spin-symmetry breaking (i.e., they exhibited a restricted → unrestricted determinantal instability). Reoptimization using a broken-symmetry unrestricted Kohn-Sham formalism led in every case to a *new* TS structure in which bond formation between the alkyne termini connected proximally to the tether was evident, but the remaining distal alkyne termini remained far apart. In the case of **1**, for instance, the forming C–C bond length in this broken-symmetry TS structure is 1.779 Å, while the distance between the remaining alkyne termini is 4.740 Å. These TS structures, then, are consistent with *stepwise* reactivity. In the case of **6**, it was possible to locate this stepwise TS structure even though it had not proven possible to find a concerted TS structure. In every

instance where a comparison could be made, these stepwise TS structures were predicted to be 4–6 kcal/mol lower in energy than the corresponding concerted TS structures. The broken-symmetry TS structures were all characterized by $\langle S^2 \rangle$ values of 0.45, consistent with significant diradical character.

As expected for a stepwise pathway, in each case except for **4** it was also possible using broken-symmetry Unrestricted Density Functional Theory (UDFT) to locate diradical intermediates (having $\langle S^2 \rangle$ values very near 1.00) and in addition subsequent TS structures for the formation of the second C–C bond leading to *o*-benzyne products. We will distinguish these two TS structures along any stepwise path as TS1 and TS2 for purposes of discussion. Enthalpies computed for TS2 structures were in every case below those computed for TS1; i.e., it is TS1 that is predicted to be rate determining. Interestingly, while intermediate diradicals between these two TS structures could be identified on the potential energy surface in every case other than **4**, including zero-point vibrational energies and 298 K enthalpic contributions caused the enthalpy of TS2 to fall below that of the intermediate in several instances. The reaction in such cases is stepwise on the potential energy surface, but from an enthalpic standpoint may be viewed as concerted, albeit extremely asynchronous— consistent with the term "stepwise-like," if we indulge in such coinage of a term. For **4**, on the other hand, it was not possible to find an intermediate diradical, so the reaction truly is predicted to be concerted, even with broken-symmetry DFT, but it is extremely asynchronous.

If we now consider the predicted energetics associated with the rate-determining TS1 structures (Table 4.2), we see that, for **1**–**5**, theory overestimates the enthalpy of activation in every case, but by an average of only 1.3 kcal/mol. The variation across all five substrates is 2.4 kcal/mol, which is still larger than that observed in the experimental data, although by a slightly smaller margin than predicted for the concerted reaction paths. These results taken as a whole argue for assignment of the mechanism of the intramolecular HDDA reaction as stepwise(-like). For the case of **1**, the various reaction paths are compared to one another in

Figure 4.3.

Fig. 4.3 Concerted and Stepwise-like Reaction Paths for **1**

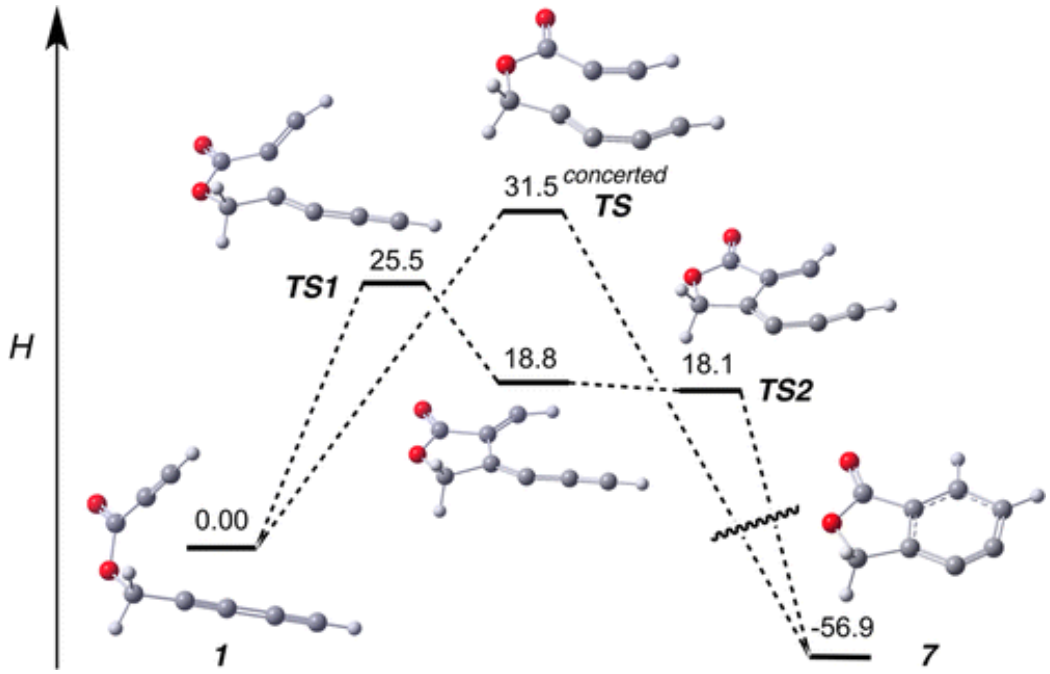

Concerted and stepwise-like reaction paths for **1** at the B3LYP-D3BJ level of theory; relative enthalpies are reported in kcal/mol from the B3LYP-D3BJ level (individual structures are shown, but relative enthalpies are computed from a Boltzmann average over all relevant contributors).

Given the reasonably good correlation of computed and experimental values for the others, it is somewhat surprising that B3LYP-D3BJ predicts a substantially smaller activation enthalpy for the bis-trimethylsilylated substrate **6** than is observed experimentally. Such a prediction is consistent with an enhanced stability of the diradical intermediate that is produced, as might be expected given silyl substitution at both radical centers (such stability is also manifest in the higher barrier remaining for completion of this cycloaddition compared to substrates **1**–**5**).[i] Nevertheless, repeat experiments confirmed that **1** and **6** cyclize with very similar rates. We considered whether the assumption of common Arrhenius *A* values

[i]The stabilizing effects of α-silyl substitution has been discussed in the literature, with both electronic and rehybridization effects being suggested to be important [28,29]

might be invalid in this instance, but inspection of computed entropies of activation (a simple relationship exists between the entropy of activation and the Arrhenius A value[21]) suggested that any difference would be unlikely to account for more than a few tenths of a kcal/mol variation in the activation enthalpy. Another possibility is some specific interaction with the surrounding solvent that is unique to the doubly silyl-substituted **6**, but we did not explore this further.

Instead, we chose to expand our consideration to an additional six substrates for the intramolecular HDDA reaction (top of Table 4.3) for which experimental kinetic data are also available.[30] A comparison of activation enthalpies continuing to employ the B3LYP-D3BJ level of theory is presented in Table 4.3, focusing exclusively on the stepwise(-like) reaction coordinate. It is apparent that there is very good agreement between theory and experiment, with the error being less than 1.1 kcal/mol in every case except for **14**, where the error is 3.0 kcal/mol. However, the "experimental" value of the Arrhenius activation energy (which is used to determine the activation enthalpy: $E_a = \Delta H^{\ddagger} + RT$[21]) is likely underestimated in the case of **14** because it was determined from the observed rate by assuming the same A value that is used for compounds having free rotation about all single bonds in the tether. The use of the alternative and larger A value that is determined/employed for compounds having far less rotational freedom (i.e., **13**, **16**, and **18**; see Experimental Section) would increase the experimental enthalpy of activation reported in Table 4.3 by nearly 2 kcal/mol and bring it into much closer agreement with theory. The actual A value for **14**, which has moderately restricted rotation, is likely somewhere in between the two extreme values, but temperature-dependent measurements have not been made to assess this point more quantitatively. In any case, the mean signed and unsigned errors comparing theory and experiment for **13**–**18** provide additional strong support for the assignment of a stepwise(-like) mechanism to the intramolecular HDDA reaction.

Table 4.3 Experimentally Derived and Computed Activation Enthalpies (kcal/mol) for **13**–**18**

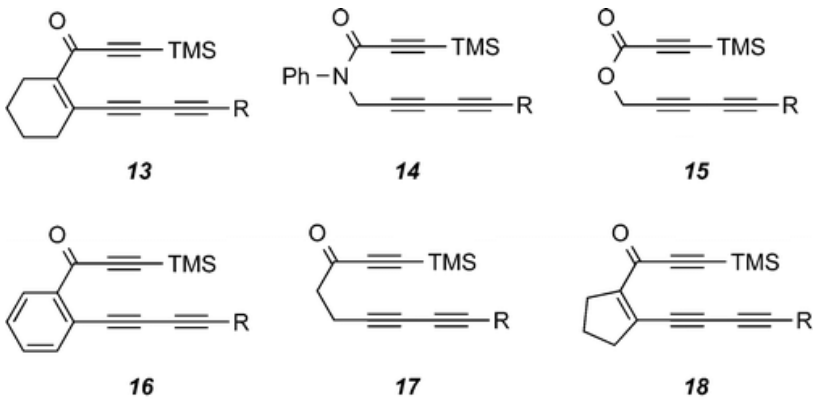

$R_{experimental}$ = $(CH_2)_2OTBS$ $R_{computed}$ = Et

	$\Delta H^{\ddagger}$	
Compound	Experimental	B3LYP-D3BJ TS1
13	19.1	19.1
14	21.4	24.4
15	22.6	23.5
16	22.7	21.6
17	27.0	27.4
18	27.2	26.7
MSE[a]		0.45
MUE[b]		0.98

[a]Mean signed error. [b]Mean unsigned error.

We close this subsection by noting the degree to which theory provides an important rationalization for two seemingly inconsistent experimental observations, namely (i) rates that appear largely insensitive to steric bulk at the distal termini of the reacting alkyne linkages, and thus seem more in support of a stepwise mechanism, and (ii) the failure of external additives (solvent, oxygen, or phenolic radical inhibitors) to alter the course of reaction, expected for pathways involving intermediates having (di)radical character, which supports a concerted mechanism. In this instance, the reaction appears to be balanced on

the knife edge between these two formal pathways. Thus, there is a rate-determining TS structure that has essentially no bond formation occurring at the distal termini, but the resulting intermediate diradical either fails to be a minimum or, if it is a minimum, fails to have a sufficient lifetime to be trapped prior to crossing a second transition state to complete the cycloaromatization. Indeed, insofar as the potential energy surfaces for the reactions studied here represent 0 K Born–Oppenheimer topologies that are relatively flat, at more typical reaction temperatures one would expect reactive trajectories to sample a broad range of structures, with some trending toward more concerted, albeit still quite asynchronous, overall reaction paths.

One may regard the intramolecular HDDA in some respects as a variation on the known dimerization reaction of alkynes to generate 1,3-butadiene-diyl intermediates,[31–33] a process that Haberhauer and Gleiter have recently predicted to be competitive with Bergman cyclization when sufficiently high concentrations of substrate outweigh the otherwise entropically favored intramolecular process.[34] A key difference in the two processes, however, is that the diradical intermediate that is formed in the alkyne dimerization process is preferentially *s*-trans in geometry, and immediate closure to a formal [2 + 2] cycloadduct is expected to be kinetically disfavored, compared to other radical reactions, given the very high strain energy associated with the product cyclobutadiene ring. In the HDDA example, by contrast, the developing radical character of one of the vinyl centers is progressively delocalized in an "in-plane" allylic sense to the remaining alkyne terminus, which creates an opportunity for ring closure to the six-membered benzyne, a more energetically favorable option. Indeed, in the intramolecular case with a reasonably short tether, the geometry lending itself to such an outcome is essentially so constrained. As noted in the introduction, Houk and co-workers[8] have found diradical pathways to be operative in their theoretical studies of intermolecular HDDA reactions, and it would not be surprising if experiment were to reveal such reactions to generate longer-lived diradical intermediates (the promiscuity of

which might compromise the reactions synthetic utility)— to date, however, no experimental results are available against which to assess this point. It is also relevant that small, unsubstituted conjugated poly-ynes such as 1,3-butadiyne[35] and 1,3,5-hexatriyne[36] (a natural product!) are known to detonate when handled as neat substances.

The intramolecular HDDA reaction is in some sense unique among hydrocarbon cycloaromatization reactions, insofar as the diradical character generated along the reaction coordinate is predisposed to continue reaction so as readily to join what would otherwise be two radical centers into a new bond (noting that the so-produced *o*-benzyne cycloadduct *does* have some biradical character,,[37–39] but *o*-benzynes are nevertheless generally regarded as highly reactive closed-shell species in organic synthesis[40]). This is in contrast, then, to the Bergman cycloaromatization of an enediyne,[41,42] which generates a diradical *p*-benzyne intermediate that is incapable of further closure owing to the instability of what would be a "Dewar benzyne" product.[43–47] The intramolecular HDDA is also in contrast with the MyersSaito[48,49] and Schmittel[50] cycloaromatizations of enyne-allenes, which lead to α,3-didehydrotoluene and extracyclic fulvenoid diradical intermediates, respectively,[47,51–54] and with the cycloaromatization of the enyne-cumulene neocarzinostatin chromophore, which leads to a 1,5-didehydroindene.[55] In none of these other cases are the radical centers able to react (intramolecularly) with one another to form a new bond (and ring): geometric constraints prevent such a closure.

While the particular circumstances of the intramolecular HDDA make it possible for an intermediate with diradical character to close productively, one may certainly ask the question, why is there diradical character at all? Why does the reaction not occur in a fully concerted fashion? It is not obvious that there is an intuitively simple answer to this question, and indeed our calculations predict that the degree of diradical character is quite sensitive to substitution (cf. Table 4.2, page 124), suggesting that a continuum of reactivity may be accessed based on steric and electronic factors that differentially affect alternative

transition-state structures. At one time, a lively debate centered on the propensity of electrocyclic reactions to undergo concerted vs stepwise reaction mechanisms.[56–58] The intramolecular HDDA reaction is an interesting new contributor to this discussion, to the extent that in its case the answer seems to be, "It depends."

While experiments examining kinetic isotope effects (KIEs for intramolecular HDDA reactions have yet to be performed, we have carried out calculations for **1** that indicate that they may be expected to be potentially useful for further distinguishing between stepwise-like and fully concerted reactivity (Table 4.4). In particular, compared to the concerted TS structure, in the stepwise-like TS structure the more significant rehybridizations of the distal termini associated with developing radical character lead to noteworthy predicted differences in secondary H/D KIEs.

Table 4.4 Secondary Kinetic Isotope Effects (Dimensionless) Predicted at the B3LYP-D3BJ Level for the Parent Triyne **1**

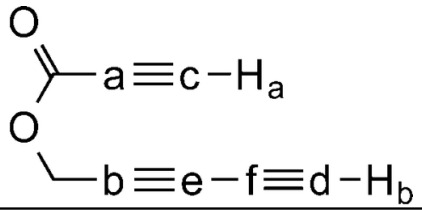

Position	Concerted TS	Stepwise TS1
C_a	1.0220	1.0398
C_b	1.0211	1.0360
C_c	1.0202	1.0158
C_d	1.0138	1.0040
C_e	1.0098	1.0160
C_f	1.0072	1.0080
H_a	1.0569	1.0863
H_b	1.0028	1.0237

In addition, the *difference* in the secondary $^{12}C/^{13}C$ KIEs for the proximal vs the distal alkyne termini is predicted to be considerably larger for the stepwise-like TS structure than

for the concerted structure (KIEs for the interior carbon atoms in the diyne fragment do not show much sensitivity to TS structure and are unlikely to be useful for distinguishing between the two mechanisms).

Additional Computational Analysis This section provides additional support for the mechanistic analysis provided above, but is likely to be of interest primarily to specialists, as it addresses technical details associated with further validation of the computations beyond simple comparison to experimental quantities. Such a comparison is especially important because the structures and energies computed from DFT prove to be extraordinarily sensitive to the choice of functional, which can certainly lead to decreased confidence in interpretation, even when good quantitative agreement with measured quantities appears to be achieved by a particular functional choice. In such situations, it is helpful to employ alternative levels of electronic structure theory, the design of which may render them less sensitive than DFT to particular challenges.

To begin, we note that activation enthalpies predicted for the concerted or stepwise TS structures, from restricted and unrestricted single-point calculations with other functionals, respectively, span a very wide range. Of the functionals tested, the smallest and largest enthalpies of activation associated with the concerted TS structure were 28.9 and 36.1 kcal/mol, as predicted by the M11-L and B3LYP functionals, respectively (see SI for full details). Similarly, the smallest and largest enthalpies of activation associated with the stepwise TS structure TS1 were 22.5 and 32.4 kcal/mol, as predicted by the M11-L and M06-2X functionals, respectively. In general, functionals including higher proportions of exact (Hartree–Fock) exchange predict higher relative energies for TS structures and exhibit larger values of $\langle S^2 \rangle$ in their broken-symmetry wave functions. Above and beyond this variation associated with single-determinantal instability, there may also be some effect from the documented failure of several functionals to predict accurately the energetics of reactions

in which one or more bonds are transformed from π type to σ type.[59]

Perhaps not surprisingly, given this substantial variation in relative enthalpies for fixed structures as a function of the functional, there is also substantial variation in the location of stationary points on overall cycloaddition potential energy surfaces as a function of the functional. This is illustrated in Figure 4.4, for instance, where the M06-2X and B3LYP levels of theory are compared using the somewhat smaller 6-31+G(d,p) basis set to map the two-dimensional surface defined by the distances between the two sets of alkyne termini. In both panels of Figure 4.4, two trajectories are shown. Both begin at the upper right on the reduced potential energy surface (PES), with long distances between the two sets of alkyne termini characteristic of the reactant structure. Closing the proximal C–C bond without substantially reducing the distance between the distal termini is equivalent to moving horizontally left on the PES, and that stepwise pathway proceeds through a saddle point (i.e., TS1) with a forming proximal C–C bond distance of about 1.8 Å while the distal C–C separation remains about 4.8 Å. A diradical intermediate occupies "the high plateau" at upper left in the PES, and that intermediate can continue to react by shortening the distal C–C distance, corresponding to movement vertically downward in the diagram. The trajectory passes through the saddle point TS2 (which is at lower energy than TS1) at a terminal C–C distance of about 2.9 Å and continues steeply downhill thereafter to the *o*-benzyne product at the lower left in the PES.

Fig. 4.4 Potential Surface Maps for the HDDA Reaction of the Parent Triyne **1**

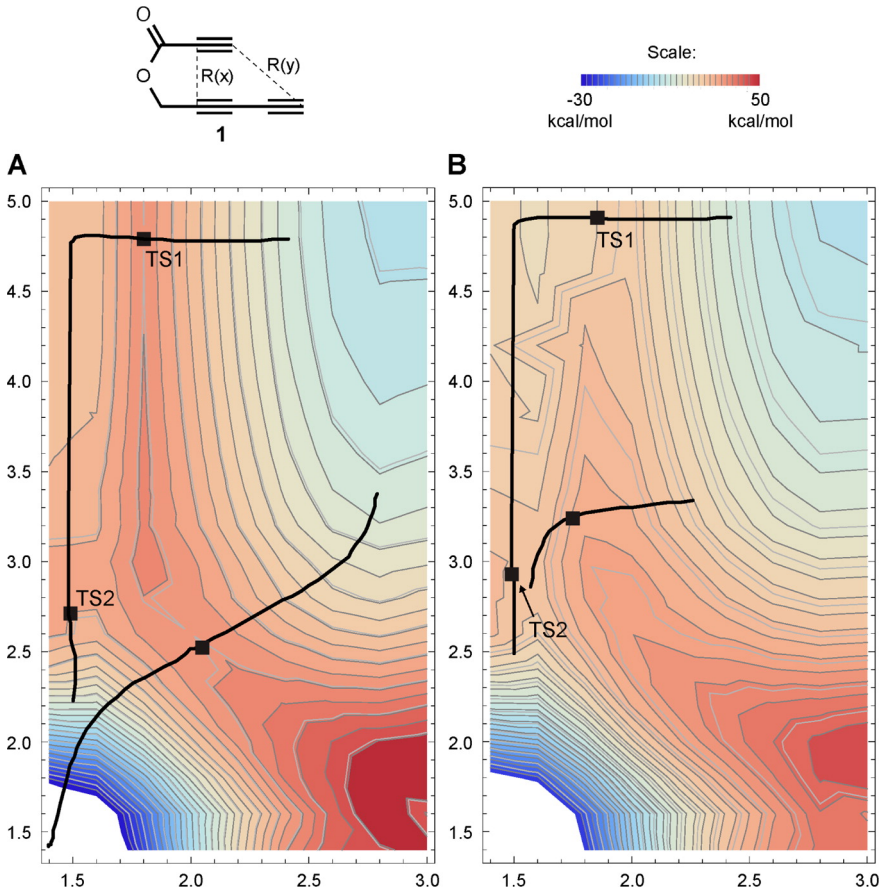

(A) UM06-2X/6-31+G(d,p) potential surface and (B) UB3LYP/6-31+G(d,p) potential surface for the HDDA reaction of the parent triyne **1**. Distances R(x) and R(y) are plotted on the respective x and y axes in Å. Energies in kcal/mol are relative to the optimized reactive conformer energy in each respective model chemistry. In panel A, a stepwise reaction path is illustrated proceeding from reactant, at upper right, through TS1 to an intermediate diradical, at upper left, through TS2 to products at lower left. Also shown is the path proceeding through a concerted TS. The formal concerted and stepwise reaction pathways are plotted for A and B using the default IRC algorithm in Gaussian 09. Black squares mark the location of optimized transition state geometries for each case.

A second trajectory in each panel begins by reducing the terminal distance first (downward movement), followed by a coupled closure of both distances (diagonally downward left movement) until a concerted-like TS structure is reached (Figure 4.4), after which continued movement along the trajectory goes directly to the product. At the M06-2X/6-31+G(d,p)

level of theory, the energies of TS1 and the concerted TS structure are quite close to one another. However, the generation of these surfaces is complicated by the tendency for the Kohn–Sham wave functions to exhibit restricted → unrestricted instabilities over large regions of the surface on either side of a diagonal running from upper left to lower right. Coaxing convergence to a lower energy unrestricted solution rather than a higher energy restricted solution is not always a simple task and can lead to some jaggedness in the contour plots (this is particularly evident in panel B for B3LYP).

Considering the B3LYP PES in more detail, it is apparent that on this surface there is a stepwise trajectory analogous to that on the M06-2X surface, but the concerted-like TS structure does not occur at a visible saddle point—contours to the lower right of TS1 rise monotonically in energy toward the energy peak found at the lower right in both PESs. Note that this energy peak corresponds to structures having distal bond closure preceding proximal bond closure. As was noted in the introduction, such a reaction mechanism seems intuitively unlikely, but these PESs offer more quantitative support for that contention.

If we assume, for the moment, that the M06-2X TS structures are reasonably representative of saddle points for stepwise and concerted reactions on some "true" Born–Oppenheimer surface, it is worth noting that while there is substantial deviation in the absolute activation enthalpies predicted by various functionals, there is uniformity in the prediction that activation enthalpies predicted for stepwise TS1 (from broken-symmetry DFT) are always lower than those predicted for the concerted TS structure (using either a restricted or unrestricted formalism). This offers additional support for the overall mechanistic interpretation of a mechanism in which bond formation is either fully stepwise or stepwise-like. However, more convincing support requires that we consider a level of electronic structure theory that includes nondynamical electron correlation in a rigorous fashion (it is a nondynamical correlation, which is associated with near degeneracies in frontier orbital energies associated with diradicals, that causes spin symmetry breaking in the various Kohn–Sham determinants

described above[21]).

Such a level of theory is second-order perturbation theory based on a complete-active space self-consistent field (CASSCF) wave function; this level is denoted CASPT2.[22,23] For substrate **1**, we carried out CASPT2 calculations based on a CASSCF(12,12) wave function for the same reactant, TS1, and concerted TS structures employed in our DFT calculations. We employed a triple-ζ atomic natural orbital basis set and took for the 12-electron/12-orbital active space those electrons and π and π* orbitals associated with the three triple bonds. Results from the CASPT2 level are compared to those from the density functional models in Table 4.5.

Table 4.5 Single-Point Relative Electronic Energies (kcal/mol) for Reactant and Concerted and Stepwise TS Structures of Parent Triyne **1** at Various Levels of Theory

Structure[a]	M06-2X	B3LYP-D3BJ	CASPT2	dom. CSF wt.[b]	CAS wt.[c]
Reactant[d]	0.0	0.0	0.0	0.831	0.697
Stepwise TS1	29.2	22.9	21.9	0.727	0.695
Concerted TS	33.7	29.8	25.6	0.787	0.695

[a]From M06-2X/6-311+G(d,p) level of theory; see Theory/Computational Models Section (Page 119). [b]Weight of the dominant configuration-state function (CSF) in the CASSCF wave function. [c]Weight of the CASSCF wave function in the PT2 expansion. [d]Structure in prereactive conformation.

CASPT2 shows good quantitative agreement with broken- symmetry B3LYP-D3BJ for the energy of stepwise TS1 relative to the reactant, while broken-symmetry M06-2X predicts a substantially higher value (consistent with its increased percentage of exact exchange compared to B3LYP, *vide supra*). CASPT2 predicts the concerted TS structure to be 3.7 kcal/mol higher in energy than TS1, which interestingly is in reasonable agreement with the separation between the two TS structures predicted by M06-2X, but is smaller than the separation predicted by B3LYP-D3BJ. Importantly, the weight of the CASSCF wave function in the PT2 expansion is essentially identical for all three molecular structures;

this suggests that the application of perturbation theory to their relative energies is not unbalanced. Also of interest, the weight of the dominant configuration-state function (in this case the restricted HartreeFock-like determinant) drops from 0.831, for the reactant, to 0.787, for the concerted TS structure, to 0.727, for stepwise TS1. This significant drop in the weight of the dominant configuration is entirely consistent with the tendency for the Kohn–Sham single determinants to exhibit restricted $\rightarrow$ unrestricted symmetry breaking as proximal bond formation advances along the cyclization reaction coordinate.[60]

Taken as a whole, the comparison of DFT and CASPT2 results provides additional support for a stepwise(-like) mechanism above and beyond that inferred from direct comparison of the B3LYP-D3BJ results to experiment as presented above. A single remaining vulnerability might be the theoretical reliance on geometries obtained from the M06-2X functional, in spite of that functionals generally very good performance[61] for organic geometries (for both minima and TS structures). It is not obvious, however, that any other model might be expected to offer a guaranteed improvement. Other functionals are similarly prone to symmetry breaking in the face of diradical character, and CASSCF geometries are known to be rather poor as they fail to include dynamical electron correlation during the optimization process (we have not attempted the more tedious task of CASPT2 geometry optimizations). And, while the M06-2X and B3LYP PESs in Figure 4.4 certainly have some qualitative differences, they are in general agreement that one would not expect a sharp drop in the energy of the concerted TS structure on the basis of small variations in otherwise roughly similar C–C bond lengths.

One remaining possibility is to consider a highly correlated post-Hartree–Fock method to provide one additional window into the computational characterization of the reaction mechanism. To that end, we investigated the CBS-QB3 composite level of theory,[26] which includes steps up to the coupled cluster level of theory including all single, double, and perturbatively estimated triple excitations. At the CBS-QB3 level (which by construction

employs B3LYP optimized geometries), the concerted and stepwise TS structures are predicted to have gas-phase enthalpies of 27.4 and 29.8 kcal/mol, respectively, relative to the reactant. Thus, the CBS-QB3 level predicts the *concerted* TS structure to be lower in energy, an apparent inversion compared to all other levels. However, inspection of the T1 diagnostic[27] for the coupled cluster portion of the calculation suggests that this particular prediction is likely to be unreliable. A T1 value in excess of 0.02 for a singlet electronic state is generally taken to mean that the underlying wave function has sufficient diradical character to make the CCSD(T) model unstable.[27] The T1 values for the concerted and stepwise TS structures from our CBS-QB3 calculations, however, are 0.021 and 0.050, respectively. While the first value may be on the edge of reliability, the second considerably exceeds it (and, indeed, exceeds as well a more generous threshold of 0.044 that has been proposed as more appropriate for diradicals[62]). On that basis, we elected not to consider additional results from the CBS-QB3 model chemistry.

4.1.3 Conclusions

Through a comparison of theoretical models to an expanded set of experimental data and with one another, we have determined that the mechanism of the intramolecular hexadehydro-Diels–Alder proceeds in a fashion that (i) involves much more substantial bond formation between the proximal alkyne termini that are attached to the joining tether compared to bond formation between the distal alkyne termini, but that (ii) is nevertheless balanced on the knife edge of concertedness, with diradical intermediates being found to be stable on some thermodynamic surfaces but not others, depending on substitution at the distal alkyne termini. We refer to such highly asynchronous concerted pathways as "stepwise-like" insofar as diradical minima *are* in general predicted on the potential energy surface, even if they fail to remain lower in enthalpy (or free energy) than subsequent transition-state

structures for completion of the cyclization once zero-point vibrational energies and thermal contributions are added to electronic energies. The modeling of these reactions is made particularly challenging because of the instability of single-determinantal models—such as Kohn–Sham density functional and Hartree–Fock theories—along key regions of the cycloaromatization reaction coordinates. Careful calibration against both experimental results and multireference wave function theories, however, permits a clear picture to emerge that supports the stepwise(-like) mechanistic assignment. Secondary kinetic isotope effects are predicted to offer another means to further distinguish between alternative mechanistic pathways, and such experiments will hopefully prove forthcoming.

4.1.4 Experimental Section

General Information NMR spectra were recorded in the indicated solvent on a 500 MHz spectrometer. "The following format is used to report the proton NMR data: chemical shift in ppm [multiplicity, coupling constant(s) in Hz, integral, and assignment]. Coupling constant analysis was informed by methods we have previously reported.[63,64] Chemical shifts for proton spectra are referenced to TMS ($\delta = 0.00$ ppm) for spectra recorded in $CDCl_3$. Nonfirst-order multiplets are identified as 'nfom'."[ii] Chemical shifts for ^{13}C NMR spectra are referenced to $CDCl_3$ ($\delta = 77.16$ ppm). "Infrared spectral data were collected on an FT-IR spectrometer. Spectra were collected as thin films in attenuated total reflectance (ATR) mode on a germanium window."[ii] HRMS data were obtained using an electrospray ionization (ESI) mass spectrometer. Samples were doped with either PPG or PEG as an internal calibrant and then were introduced as a methanolic solution. "MPLC (medium pressure liquid chromatography) was performed at 25–200 psi. Columns were hand-packed with silica gel (18–32 µm, 60 Å pore size)."[ii] An HPLC pump outfitted with a differential refractive index detector was used. Flash chromatography was performed on silica gel. "Thin layer

[ii] From supporting information of reference 65.

chromatography was carried out on glass or plastic backed plates of silica gel. Spots were visualized by UV irradiation and/or dipping in a solution of anisaldehyde, phosphomolybdic acid, potassium permanganate, or ceric ammonium molybdate followed by heat treatment. Reactions requiring anhydrous conditions were performed in flame- or oven-dried glassware under an inert atmosphere (nitrogen or argon). Anhydrous diethyl ether, toluene, THF, and methylene chloride were passed through a column of activated alumina and tapped immediately prior to use. $CHCl_3$ used as a medium for the HDDA reaction was ethanol-free. Reported (external) reaction temperatures are the temperature of the heating bath. HDDA initiated reactions, including those that were carried out at temperatures above the boiling point of the solvent, were typically carried out in a screw-capped vial or culture tube fitted with an inert, Teflon-lined cap."[ii]

Procedure for Determination of HDDA Half-Lives A 0.1 M solution of the HDDA polyyne substrate in *o*-DCB was prepared and AcOH (10–50 equiv) was added. The vial was sealed with a Teflon-lined cap, and the solution was placed in a silicone oil bath that had been pre-equilibrated to a desired temperature. At various time points, an aliquot (ca. 15 µL) was diluted in $CDCl_3$ (600 µL) and analyzed directly via ^{1}H NMR spectroscopy (500 MHz, nt = 32). Peak integration of a resonance in the starting material vs the ^{13}C satellite resonance for the *o*-DCB was used to judge the extent of starting material consumption. Rate constants (k) were determined from the experimentally measured half-lives of HDDA substrates assuming unimolecular first-order kinetics. An Arrhenius pre-exponential factor (A) of $8.78 \times 10^8 s^{-1}$ was previously determined from the temperature-dependence of the rate via an Arrhenius plot for the analog of ester **1** having R^1 = TMS and R^2 = $(CH_2)_2OTBS$.[65] Activation energies E_a were calculated from the Arrhenius equation ($k = Ae^{E_a/RT}$) based on single-temperature measurements using this same value of A for all substrates reported here having free rotation about all single bonds in the tethering fragment. By contrast, an

Arrhenius pre-exponential factor (A) of 1.42×10^{10}s^1 was previously determined from the temperature-dependence of the rate via an Arrhenius plot for the analog of ester **1** having R^1 = TMS and $R^2 = (CH_2)_2$OTBS but with the O–CH_2 ester linkage fragment replaced by a benzene ring (compound **16**).[65] Activation energies for substrates having similarly restricted rotation about this tether linkage (compounds **13**, **16**, and **18**) were calculated from single-temperature measurements via the Arrhenius equation using this A value. For comparison to theory, enthalpies of activation were determined according to the relationship $E_a = \Delta H^{\ddagger} + RT$.[21]

Preparation Procedures and Characterization Data for 2–6 and 8–12 All of the compounds newly described in this report.

*5-(Trimethylsilyl)penta-2,4-diyn-1-yl propiolate (**2**)* A solution of 5-(trimethylsilyl)penta-2,4-diyn-1-ol[66] (230 mg, 1.5 mmol) and propiolic acid (110 µL, 1.8 mmol) in dichloromethane (10 mL) was cooled to 0 °C. *N,N*-Dicyclohexylcarbodiimide (370 mg, 1.8 mmol) and DMAP (15 mg, 0.12 mmol) were added, and the mixture was allowed to come to room temperature. After 4 h the solution was filtered through a plug of Celite, rinsing with EtOAc. After solvent removal the crude material was purified by MPLC (15:1 Hex/EtOAc) to give triyne **2** (155 mg, 0.76 mmol, 51%) as an amber oil. ^{1}H NMR (500 MHz, $CDCl_3$): δ 4.84 (s, 2H), 2.96 (s, 1H), 0.20 (s, 9H). ^{13}C NMR (125 MHz, $CDCl_3$): δ 151.7, 89.1, 86.7, 76.3, 73.8, 72.5, 69.9, 53.9, and –0.5. IR: 3291, 2963, 2123, 1724, 1252, 1207, 966, 848, and 753 cm^{-1}. HR ESI-MS calcd for $C_{11}H_{12}NaO_2Si$ $[M + Na]^+$ 227.0499, found 227.0482.

*5-(tert-Butyldimethylsilyl)penta-2,4-diyn-1-yl Propiolate (**3**)* A solution of 5-(tert-butyldimethylsilyl)penta-2,4-diyn-1-ol[67] (194 mg, 1.0 mmol) and propiolic acid (75 µL, 1.2 mmol) in dichloromethane (8 mL) was cooled to 0 °C. *N,N*-Dicyclohexylcarbodiimide (247 mg,

1.2 mmol) and DMAP (15 mg, 0.12 mmol) were added and the mixture was allowed to come to room temperature. After 2 h the solution was filtered through a plug of Celite, rinsing with EtOAc. After solvent removal the crude material was purified by MPLC (10:1 Hex:EtOAc) to give triyne **3** (168 mg, 0.68 mmol, 68%) as an amber oil. ^{1}H NMR (500 MHz, $CDCl_3$): δ 4.85 (s, 2H), 2.96 (s, 1H), nmeh0.94s9, nmeh0.14s6. ^{13}C NMR (125 MHz, $CDCl_3$): δ 151.8, 87.9, 87.4, 76.3, 73.9, 72.7, 69.4, 54.0, 26.1, 16.8, and –4.8. IR: 3290, 2954, 2931, 2858, 2123, 1725, 1208, 830, and 778 cm^{-1}. HR ESI-MS calcd for $C_{14}H_{18}NaO_2Si$ $[M + Na]^+$ 269.0972, found 269.0957.

5-(Triphenylsilyl)penta-2,4-diyn-1-yl Propiolate (4) 5-(Triphenylsilyl)penta-2,4-diyn-1-ol was prepared as follows: Under an inert atmosphere, triphenylsilyl acetylene (284 mg, 1.0 mmol) and 3-bromopropargyl alcohol (335 mg, 2.5 mmol) were dissolved in 4 mL of freshly deaerated piperidine, and the solution was cooled to 0 °C. CuCl (40 mg, 0.4 mmol) was added, and the reaction mixture was stirred for 1.5 h at 0 °C. The mixture was diluted with satd aq. NH_4Cl and extracted with EtOAc. The combined organic extracts were washed with brine, dried ($MgSO_4$), and concentrated. Purification by MPLC (3:1 Hex/EtOAc) gave 5-(triphenylsilyl)penta-2,4-diyn-1-ol (125 mg, 0.40 mmol, 40%) as a clear oil ^{1}H NMR (500 MHz, $CDCl_3$): δ 7.63 (dt, J = 6.6, 1.4 Hz, 6H), 7.45 (tt, J = 7.4, 1.4 Hz, 3H), 7.39 (ddd, J = 7.5, 6.7, and 1.4 Hz, 6H), 4.37 (s, 2H), and 1.64 (br s, 1H). A solution of this 5-(triphenylsilyl)penta-2,4-diyn-1-ol (110 mg, 0.32 mmol) and propiolic acid (30 µL, 0.48 mmol) in dichloromethane (3 mL) was cooled to 0 °C. *N,N*-Dicyclohexylcarbodiimide (100 mg, 0.48 mmol) and DMAP (5 mg, 0.04 mmol) were added, and the mixture was allowed to come to room temperature. After 4 h the solution was filtered through a plug of Celite, rinsing with EtOAc. After solvent removal the crude material was purified by MPLC (12:1 Hex/EtOAc) to give triyne **4** (65 mg, 0.17 mmol, 51%) as a clear oil. ^{1}H NMR (500 MHz, $CDCl_3$): δ 7.62 (dd, J = 8.0, 1.4 Hz, 6H), 7.45 (ddd, J = 7.3, 7.3, and 1.4 Hz, 3H), 7.39

(ddd, J = 7.5, 6.8, and 1.4 Hz, 6H), 4.86 (s, 2H) and 2.95 (s, 1H). ^{13}C NMR (125 MHz, $CDCl_3$): δ 151.7, 135.7, 132.2, 130.4, 128.3, 90.7, 84.0, 76.5, 73.8, 72.6, 71.3, and 53.9. IR: 3272, 3069, 3050, 3023, 2119, 1724, 1429, 1208, 1113, 967, 806, and 749 cm^{-1}. HR ESI-MS calcd for $C_{26}H_{18}NaO_2Si$ $[M + Na]^+$ 413.0968, found 413.0979.

*Penta-2,4-diyn-1-yl 3-(trimethylsilyl)propiolate (**5**)* A solution of penta-2,4-diyn-1-ol[68] (60 mg, 0.75 mmol) and 3-trimethylsilylpropynoic acid (140 mg, 1.0 mmol) in dichloromethane (7 mL) was cooled to 0 °C. *N,N*-Dicyclohexylcarbodiimide (206 mg, 1.0 mmol) and DMAP (10 mg, 0.08 mmol) were added, and the mixture was allowed to come to room temperature. After 4 h the solution was filtered through a plug of Celite, rinsing with EtOAc. After solvent removal the crude material was purified by MPLC (20:1 Hex/EtOAc) to give triyne **5** (65 mg, 0.32 mmol, 42%) as an amber oil. ^{1}H NMR (500 MHz, $CDCl_3$): δ 4.81 (s, 2H), 2.23 (s, 1H), and 0.26 (s, 9H). ^{13}C NMR (125 MHz, $CDCl_3$): δ 151.9, 96.3, 93.4, 71.6, 69.3, 69.1, 67.1, 53.4, and –0.8. IR: 3294, 2965, 2363, 2344, 2175, 2118 1719, 1253, 1205, 848, and 760 cm^{-1}. HR ESI-MS calcd for $C_{11}H_{12}NaO_2Si$ $[M + Na]^+$ 227.0499, found 227.0489.

*5-(Trimethylsilyl)penta-2,4-diyn-1-yl 3-(trimethylsilyl)-propiolate (**6**)* The following reagents were added in sequence to CH_2Cl_2 (5 mL) at 0 °C: 5-(trimethylsilyl)penta-2,4-diyn-1-ol (137 mg, 0.9 mmol), 3-trimethylsilylpropynoic acid (142 mg, 1.0 mmol), EDCI (170 mg, 1.1 mmol), and DMAP (12 mg, 0.1 mmol). The resulting homogeneous solution quickly became cloudy. After 3 h the suspension was diluted with H_2O and extracted with CH_2Cl_2. The combined organic extracts were washed with brine, dried ($MgSO_4$), and concentrated. Purification by MPLC (10:1 hexanes/EtOAc) gave the ester **6** (140 mg, 0.51 mmol, 51%) as a clear oil. ^{1}H NMR (500 MHz, $CDCl_3$): δ 4.81 (s, 2H), 0.25 (s, 9H), and 0.20 (s, 9H). ^{13}C NMR (125 MHz, $CDCl_3$): δ 152.0, 96.2, 93.5, 88.9, 86.8, 72.3, 70.3, 53.6, –0.4, and –0.8. IR: 2965, 2903, 2114, 1721, 1253, 1205, 851, and 760 cm^1. HR ESI-MS calcd for $C_{14}H_{20}NaO_2Si_2$

$[M + Na]^+$ 299.0894, found 299.0898.

*1-Oxo-6-(trimethylsilyl)-1,3-dihydroisobenzofuran-5-yl acetate (**8**)* A solution of triyne **2** (24 mg, 0.12 mmol) and acetic acid (70 µL, 10 equiv) in DCB (1.0 mL) was heated at 120 °C. After 24 h the solution was loaded onto a column of silica and DCB was removed by initial elution with hexanes. Subsequent elution with hexanes/EtOAc (2:1) gave the benzenoid **8** (28 mg, 0.11 mmol, 90%) as a yellow oil. ^{1}H NMR (500 MHz, $CDCl_3$): δ 8.05 (d, J = 0.6 Hz, 1H), 7.27 (t, J = 0.8 Hz, 1H), 5.30 (d, J = 1.2 Hz, 2H), 2.37 (s, 3H), and 0.33 (s, 9H). ^{13}C NMR (125 MHz, $CDCl_3$): δ 170.5, 168.8, 159.7, 149.2, 134.2, 133.2, 122.8, 115.8, 69.2, 21.6, and –1.0. IR (neat): 2954, 2900, 1762, 1618, 1248, 1190, 1136, 1068, 1010, and 843 cm^{-1}. HRMS (ESI-TOF): Calcd for $C_{13}H_{16}NaO_4Si^+$ $[M + H^+]$ requires 287.0710; found 287.0721.

*6-(tert-Butyldimethylsilyl)-1-oxo-1,3-dihydroisobenzofuran-5-yl acetate (**9**)* A solution of triyne **3** (35 mg, 0.14 mmol) and acetic acid (80 µL, 10 equiv) in DCB (1.4 mL) was heated at 135 °C. After 18 h the solution was loaded onto a column of silica and DCB was removed by initial elution with hexanes. Subsequent elution with hexanes/EtOAc (2:1) gave benzenoid **9** (33 mg, 0.11 mmol, 76%) as a yellow oil. ^{1}H NMR (500 MHz, $CDCl_3$): δ 8.05 (s, 1H), 7.28 (t, J = 0.8 Hz, 1H), 5.31 (d, J = 0.9 Hz, 2H), 2.36 (s, 3H), 0.90 (s, 9H), and 0.35 (s, 6H). ^{13}C NMR (125 MHz, $CDCl_3$): δ 170.6, 168.9, 159.7, 149.0, 134.5, 131.7, 122.6, 116.1, 69.2, 60.6, 53.6, 26.7, 21.8, 17.6, and –4.7. IR (neat): 2953, 2930, 2883, 2857, 1764, 1618, 1250, 1189, 1065, 1010, 837, and 768 cm^{-1}. HRMS (ESI-TOF): Calcd for $C_{16}H_{22}NaO_4Si^+$ $[M + Na^+]$ requires 329.1180; found 329.1182.

*6-(Triphenylsilyl)-1-oxo-1,3-dihydroisobenzofuran-5-yl acetate (**10**)* A solution of triyne **4** (20 mg, 0.05 mmol) and acetic acid (30 µL, 10 equiv) in DCB (0.5 mL) was heated at 135 °C. After 24 h the solution was loaded onto a column of silica and DCB was removed by initial

elution with hexanes. Subsequent elution with hexanes/EtOAc (2:1) gave benzenoid **10** (22 mg, 0.05 mmol, 95%) as a yellow oil containing minor impurities. ^{1}H NMR (500 MHz, $CDCl_3$): δ 7.91 (d, J = 0.5 Hz, 1H), 7.54 (dd, J = 8.0, 1.4 Hz, 6H), 7.46 (tt, J = 7.4, 1.5 Hz, 3H), 7.40 (m, 6H), 7.37 (t, J = 1.4 Hz, 1H), 5.34 (d, J = 1.3 Hz, 2H), and 1.38 (s, 3H). ^{13}C NMR (125 MHz, $CDCl_3$): δ 170.2, 168.3, 159.8, 150.3, 136.5, 136.1, 132.8, 130.2, 129.4, 128.3, 122.9, 116.6, 69.2, and 20.2. IR (neat): 2955, 2922, 1767, 1618, 1457, 1429, 1371, 1293, 1247, 1185, 1136, 1109, 1067, and 1012 cm^{-1}. GC-MS t_r (5031022) = 15.37 min; m/z: 373, 331, 253, 207. HRMS: (ESI-TOF): Calcd for $C_{28}H_{22}NaO_4Si^+$ [M + Na^+] requires 473.1180; found 473.1187.

*1-Oxo-7-(trimethylsilyl)-1,3-dihydroisobenzofuran-5-yl acetate (**11**)* A solution of triyne **5** (20 mg, 0.10 mmol) and acetic acid (110 µL, 20 equiv) in DCB (9.0 mL) was heated at 125 °C. After 24 h the solution was loaded onto a column of silica and DCB was removed by initial elution with hexanes. Subsequent elution with hexanes/EtOAc (2:1) gave the crude product. Purification via MPLC (5:1 Hex/ EtOAc) gave benzenoid **11** (24 mg, 0.09 mmol, 93%) as a yellow oil. ^{1}H NMR (500 MHz, $CDCl_3$): δ 7.31 (d, J = 2.0 Hz, 1H), 7.23 (dt, J = 1.9, 0.9 Hz, 1H), 5.29 (d, J = 0.7 Hz, 2H), 2.36 (s, 3H), and 0.40 (s, 9H). ^{13}C NMR (125 MHz, $CDCl_3$): δ 170.9, 169.1, 154.2, 148.6, 144.4, 128.8, 127.5, 115.9, 69.0, 21.3, and –1.2. IR (neat): 2934, 2855, 1759, 1588, 1194, 1128, 1048, 1010, 843, and 757 cm^{-1}. HRMS (ESI-TOF): Calcd for $C_{13}H_{16}NaO_4Si^+$ [M + H^+] requires 287.0710; found 287.0705.

*1-Oxo-6-(trimethylsilyl)-1,3-dihydroisobenzofuran-5-yl acetate (**12**)* A solution of triyne **6** (27 mg, 0.10 mmol) and acetic acid (60 µL, 10 equiv) in DCB (1.0 mL) was heated at 120 °C. After 24 h the solution was loaded onto a column of silica and DCB was removed by initial elution with hexanes. Subsequent elution with hexanes/EtOAc (5:1) gave the benzenoid **12** (28 mg, 0.08 mmol, 85%) as a yellow oil. ^{1}H NMR (500 MHz, $CDCl_3$): δ 7.16 (t, J = 0.7

Hz, 1H), 5.24 (d, J = 0.8 Hz, 2H), 2.36 (s, 3H), 0.44 (s, 9H), and 0.39 (s, 9H). ^{13}C NMR (125 MHz, $CDCl_3$): δ 171.1, 169.0, 159.2, 155.3, 148.1, 143.0, 129.3, 115.0, 68.6, 21.9, and 2.7. IR (neat): 2952, 2902, 1760, 1249, 1190, 1141, 1058, 1017, 844, and 757 cm^{-1}. HRMS (ESI-TOF): Calcd for $C_{16}H_{24}NaO_4Si_2^+$ $[M + H^+]$ requires 359.1105; found 359.1113.

4.1.5 Associated Content

The Supporting Information is available free of charge on the ACS Publications website at DOI: 10.1021/acs.joc.5b01356.

Cartesian coordinates and electronic energies for all stationary points, as well as energetics comparisons using different density functionals. Listing of ^{1}H NMR data with authors' assignments of resonances with their associated protons. Copies of ^{1}H and ^{13}C NMR spectra of all newly reported compounds (PDF)

4.1.6 Notes

The authors declare no competing financial interest.

4.1.7 Acknowledgments

This investigation was supported by grants awarded by the U.S. Department of Health and Human Services (National Institute of General Medical Sciences, GM-65597) and the U.S. National Science Foundation (CHE-1361595 and CHE-1039925, the latter a Major Research Instrumentation grant to the Midwest Undergraduate Computational Chemistry Consortium). Some of the computational aspects of this work were performed with software and hardware software made available through the University of Minnesota Supercomputing

Institute (MSI). NMR spectra were recorded on an instrument purchased with support from the NIH Shared Instrumentation Grant program (S10OD011952). We thank Vedamayee Pogula and Moriana Haj for performing several repeat experiments and Professor Laura Gagliardi for having carried out the CASPT2(12,12) calculations.

References

[1] Bradley, A. Z.; Johnson, R. P. *J. Am. Chem. Soc.* **1997**, *119*, 9917–9918.

[2] Miyawaki, K.; Suzuki, R.; Kawano, T.; Ueda, I. *Tetrahedron Lett.* **1997**, *38*, 3943–3946.

[3] Holden, C.; Greaney, M. F. *Angew. Chem., Int. Ed.* **2014**, *53*, 5746–5749.

[4] Yun, S. Y.; Wang, K.-P.; Lee, N.-K.; Mamidipalli, P.; Lee, D. *J. Am. Chem. Soc.* **2013**, *135*, 4668–4671.

[5] Niu, D.; Willoughby, P. H.; Woods, B. P.; Baire, B.; Hoye, T. R. *Nature* **2013**, *501*, 531–534.

[6] Ajaz, A.; Bradley, A. Z.; Burrell, R. C.; Li, W. H. H.; Daoust, K. J.; Bovee, L. B.; DiRico, K. J.; Johnson, R. P. *J. Org. Chem.* **2011**, *76*, 9320–9328.

[7] Hoye, T. R.; Baire, B.; Niu, D. W.; Willoughby, P. H.; Woods, B. P. *Nature* **2012**, *490*, 208–212.

[8] Liang, Y.; Hong, X.; Yu, P.; Houk, K. N. *Org. Lett.* **2014**, *16*, 5702–5705.

[9] Kerisit, N.; Toupet, L.; Larini, P.; Perrin, L.; Guillemin, J.-C.; Trolez, Y. *Chem. - Eur. J.* **2015**, *21*, 6042–6047.

[10] Zhao, Y.; Truhlar, D. G. *Theor. Chem. Acc.* **2008**, *120*, 215–241.

[11] Hehre, W. J.; Radom, L.; Schleyer, P. v. R.; Pople, J. A. *Ab Initio Molecular Orbital Theory*; Wiley: New York, 1986.

[12] Zhao, Y.; Truhlar, D. G. *Chem. Phys. Lett.* **2011**, *502*, 1–13.

[13] Becke, A. D. *Phys. Rev. A: At., Mol., Opt. Phys.* **1988**, *38*, 3098–3100.

[14] Lee, C.; Yang, W.; Parr, R. G. *Phys. Rev. B: Condens. Matter Mater. Phys.* **1988**, *37*, 785–789.

[15] Becke, A. D. *J. Chem. Phys.* **1993**, *98*, 5648–5652.

[16] Stephens, P. J.; Devlin, F. J.; Chabalowski, C. F.; Frisch, M. J. *J. Phys. Chem.* **1994**, *98*, 11623–11627.

[17] Grimme, S.; Antony, J.; Ehrlich, S.; Krieg, H. *J. Chem. Phys.* **2010**, *132*, 154104/1–154104/19.

[18] Johnson, E. R.; Becke, A. D. *J. Chem. Phys.* **2006**, *124*, 174104/1–174104/9.

[19] Marenich, A. V.; Cramer, C. J.; Truhlar, D. G. *J. Phys. Chem. B* **2009**, *113*, 6378–6396.

[20] Yamaguchi, K.; Jensen, F.; Dorigo, A.; Houk, K. N. *Chem. Phys. Lett.* **1988**, *149*, 537–542.

[21] Cramer, C. J. *Essentials of Computational Chemistry: Theories and Models*, 2nd ed.; John Wiley & Sons: Chichester, U.K., 2004.

[22] Andersson, K.; Malmqvist, P.-r.; Roos, B. O.; Sadlej, A. J.; Wolinski, K. *J. Phys. Chem.* **1990**, *94*, 5483–5488.

[23] Andersson, K.; Malmqvist, P.-r.; Roos, B. O. *J. Chem. Phys.* **1992**, *96*, 1218–1226.

[24] Roos, B. O.; Lindh, R.; Malmqvist, P.-r.; Veryazov, V.; Widmark, P.-O. *J. Phys. Chem. A* **2004**, *108*, 2851–2858.

[25] Ghigo, G.; Roos, B. O.; Malmqvist, P.-R. *Chem. Phys. Lett.* **2004**, *396*, 142–149.

[26] Montgomery, J. A.; Frisch, M. J.; Ochterski, J. W.; Petersson, G. A. *J. Chem. Phys.* **1999**, *110*, 2822–2827.

[27] Lee, T. J.; Taylor, P. R. *Int. J. Quantum Chem.* **1989**, *36*, 199–207.

[28] Laub, H. A.; Mayr, H. *Chem. - Eur. J.* **2014**, *20*, 1103–1110.

[29] Alabugin, I. V.; Bresch, S.; Manoharan, M. *J. Phys. Chem. A* **2014**, *118*, 3663–3677.

[30] Woods, B. P.; Baire, B.; Hoye, T. R. *Org. Lett.* **2014**, *16*, 4578–4581.

[31] Mayer, J.; Sondheimer, F. *J. Am. Chem. Soc.* **1966**, *88*, 602–603.

[32] Gleiter, R.; Ritter, J. *Angew. Chem., Int. Ed. Engl.* **1995**, *33*, 2470–2472.

[33] Haberhauer, G.; Gleiter, R. *J. Am. Chem. Soc.* **1999**, *121*, 4664–4668.

[34] Haberhauer, G.; Gleiter, R.; Fabig, S. *Org. Lett.* **2015**, *17*, 1425–1428.

[35] Maretina, I. A.; Trofimov, B. A. *Russ. Chem. Rev.* **2000**, *69*, 591–608.

[36] Glen, A. T.; Hutchinson, S. A.; McCorkindale, N. J. *Tetrahedron Lett.* **1966**, *7*, 4223–4225.

[37] Cramer, C. J.; Nash, J. J.; Squires, R. R. *Chem. Phys. Lett.* **1997**, *277*, 311–320.

[38] Debbert, S. L.; Cramer, C. J. *Int. J. Mass Spectrom.* **2000**, *201*, 1–15.

[39] de Visser, S. P.; Filatov, M.; Shaik, S. *Phys. Chem. Chem. Phys.* **2000**, *2*, 5046–5048.

[40] Pellissier, H.; Santelli, M. *Tetrahedron* **2003**, *59*, 701–730.

[41] Jones, R. R.; Bergman, R. G. *J. Am. Chem. Soc.* **1972**, *94*, 660–661.

[42] Bergman, R. G. *Acc. Chem. Res.* **1973**, *6*, 25–31.

[43] Kraka, E.; Cremer, D. *J. Am. Chem. Soc.* **1994**, *116*, 4929–4936.

[44] Cramer, C. J. *J. Am. Chem. Soc.* **1998**, *120*, 6261–6269.

[45] Schreiner, P. R. *Chem. Commun.* **1998**, 483–484.

[46] Mohamed, R. K.; Peterson, P. W.; Alabugin, I. V. *Chem. Rev.* **2013**, *113*, 7089–7129.

[47] Kraka, E.; Cremer, D. *Wiley Interdisciplinary Reviews-Computational Molecular Science* **2014**, *4*, 285–324.

[48] Myers, A. G. *Tetrahedron Lett.* **1987**, *28*, 4493–4496.

[49] Nagata, R.; Yamanaka, H.; Okazaki, E.; Saito, I. *Tetrahedron Lett.* **1989**, *30*, 4995–4998.

[50] Schmittel, M.; Strittmatter, M.; Kiau, S. *Tetrahedron Lett.* **1995**, *36*, 4975–4978.

[51] Schreiner, P. R.; Prall, M. *J. Am. Chem. Soc.* **1999**, *121*, 8615–8627.

[52] Cramer, C. J.; Kormos, B. L.; Seierstad, M.; Sherer, E. C.; Winget, P. *Org. Lett.* **2001**, *3*, 1881–1884.

[53] de Visser, S. P.; Filatov, M.; Shaik, S. *Phys. Chem. Chem. Phys.* **2001**, *3*, 1242–1245.

[54] Schmittel, M.; Steffen, J. P.; Maywald, M.; Engels, B.; Helten, H.; Musch, P. *J. Chem. Soc., Perkin Trans. 2* **2001**, 1331–1339.

[55] Cramer, C. J.; Squires, R. R. *Org. Lett.* **1999**, *1*, 215–218.

[56] S., D. M. J. *J. Am. Chem. Soc.* **1984**, *106*, 209–219.

[57] Borden, W. T.; Loncharich, R. J.; Houk, K. N. *Annu. Rev. Phys. Chem.* **1988**, *39*, 213–236.

[58] Houk, K. N.; Gonzalez, J.; Li, Y. *Acc. Chem. Res.* **1995**, *28*, 81–90.

[59] Pieniazek, S. N.; Clemente, F. R.; Houk, K. N. *Angew. Chem., Int. Ed.* **2008**, *47*, 7746–7749.

[60] Schmidt, M. W.; Gordon, M. S. *Annu. Rev. Phys. Chem.* **1998**, *49*, 233–266.

[61] Zhao, Y.; Truhlar, D. G. *Acc. Chem. Res.* **2008**, *41*, 157–167.

[62] Rienstra-Kiracofe, J. C.; Allen, W. D.; Schaefer, H. F. *J. Phys. Chem. A* **2000**, *104*, 9823–9840.

[63] Hoye, T. R.; Hanson, P. R.; Vyvyan, J. R. *J. Org. Chem.* **1994**, *59*, 4096–4103.

[64] Hoye, T. R.; Zhao, H. *J. Org. Chem.* **2002**, *67*, 4014–4016.

[65] Niu, D.; Wang, T.; Woods, B. P.; Hoye, T. R. *Org. Lett.* **2014**, *16*, 254–257.

[66] Bowling, N. P.; Burrmann, N. J.; Halter, R. J.; Hodges, J. A.; McMahon, R. J. *J. Org. Chem.* **2010**, *75*, 6382–6390.

[67] Marino, J. P.; Nguyen, H. N. *J. Org. Chem.* **2002**, *67*, 6841–6844.

[68] Turlington, M.; Du, Y.; Ostrum, S. G.; Santosh, V.; Wren, K.; Lin, T.; Sabat, M.; Pu, L. *J. Am. Chem. Soc.* **2011**, *133*, 11780–11794.